2018

INTERMITTENCY EFFECTS ON THE UNIVERSALITY OF LOCAL DISSIPATION SCALES IN TURBULENT BOUNDARY LAYER FLOWS WITH AND WITHOUT FREE-STREAM TURBULENCE

Sabah Falih Habeeb Alhamdi
University of Kentucky, sfal222@g.uky.edu
Author ORCID Identifier:
https://orcid.org/0000-0002-3698-8351
Digital Object Identifier: https://doi.org/10.13023/ETD.2018.214

STUDENT AGREEMENT:

I represent that my thesis or dissertation and abstract are my original work. Proper attribution has been given to all outside sources. I understand that I am solely responsible for obtaining any needed copyright permissions. I have obtained needed written permission statement(s) from the owner(s) of each third-party copyrighted matter to be included in my work, allowing electronic distribution (if such use is not permitted by the fair use doctrine) which will be submitted to UKnowledge as Additional File.

I hereby grant to The University of Kentucky and its agents the irrevocable, non-exclusive, and royalty-free license to archive and make accessible my work in whole or in part in all forms of media, now or hereafter known. I agree that the document mentioned above may be made available immediately for worldwide access unless an embargo applies.

I retain all other ownership rights to the copyright of my work. I also retain the right to use in future works (such as articles or books) all or part of my work. I understand that I am free to register the copyright to my work.

REVIEW, APPROVAL AND ACCEPTANCE

The document mentioned above has been reviewed and accepted by the student's advisor, on behalf of the advisory committee, and by the Director of Graduate Studies (DGS), on behalf of the program; we verify that this is the final, approved version of the student's thesis including all changes required by the advisory committee. The undersigned agree to abide by the statements above.

<div align="right">

Sabah Falih Habeeb Alhamdi, Student

Dr. Sean C. C. Bailey, Major Professor

Dr. Haluk E. Karaca, Director of Graduate Studies

</div>

INTERMITTENCY EFFECTS ON THE UNIVERSALITY OF LOCAL
DISSIPATION SCALES IN TURBULENT BOUNDARY LAYER FLOWS WITH
AND WITHOUT FREE-STREAM TURBULENCE

DISSERTATION

A dissertation submitted in partial
fulfillment of the requirements for
the degree of Doctor of Philosophy
in the College of Engineering at the
University of Kentucky

By
Sabah Falih Habeeb Alhamdi
Lexington, Kentucky

Director: Dr. Sean C. C. Bailey
Associate Professor of Mechanical Engineering
Lexington, Kentucky 2018

ABSTRACT OF DISSERTATION

INTERMITTENCY EFFECTS ON THE UNIVERSALITY OF LOCAL
DISSIPATION SCALES IN TURBULENT BOUNDARY LAYER FLOWS WITH
AND WITHOUT FREE-STREAM TURBULENCE

Measurements of the small-scale dissipation statistics of turbulent boundary layer flows with and without free-stream turbulence are reported for $Re_\tau \approx 1000$ ($Re_\theta \approx 2000$). The scaling of the dissipation scale distribution is examined in these two boundary conditions of external wall-bounded flow.

Results demonstrated that the local large-scale Reynolds number based on the measured longitudinal integral length-scale fails to properly normalize the dissipation scale distribution near the wall in these two free-stream conditions, due to the imperfect characterization of the upper bound of the inertial cascade by the integral length-scale. When a length-scale based on Townsend's attached-eddy hypothesis is utilized to describe the local large-scale Reynolds number near the wall, the description of the Reynolds number scaling was determined to be significantly improved and agreed with that found in homogeneous, isotropic turbulence. However, the scaling based on Townsend's attached-eddy hypothesis agreed best for the lowest 40% of the boundary layer thickness and then it degraded due to the loss of the validity of the attached eddy-hypothesis and the onset of external intermittency.

A surrogate large-scale found from turbulent kinetic energy and mean dissipation rate improved the scaling of the dissipation scales, relative to the measured integral length-scale. The probability density functions of the local dissipation scales were calculated. When the three local large-scale Reynolds numbers are used for normalization, the one based on the longitudinal integral length-scale and the one based on the length-scale of attached-eddy hypothesis provide support for the existence of a universal distribution of the local dissipation scales up to the edge of the outer region of the turbulent boundary layer, which scales differently for inner and outer regions. However, the probability density functions of the local dissipation scales normalized by these two large-scale Reynolds numbers are deviated in interface locations for the flow without free-stream turbulence due to external intermittency.

The surrogate large-scale provided the best agreement throughout the entire depth of the boundary layer. However, in the outer part of the boundary layer, a significantly reduced collapse in the scaled probability density functions was shown due to bias in the calculation introduced by the intermittent presence of laminar flow in the time series. To support that intermittency argument, injection of the free-stream turbulence was determined to improve the distribution of these normalized probability density functions in the intermittency locations for the flow regime without free-stream turbulence.

In addition, unlike in channel flow, in the outer part of the turbulent boundary layer, the normalized distributions of the local dissipation scales were observed to be dependent on wall-normal position. This was found to be attributable to the presence of external intermittency in this outer part as the presence of free-stream turbulence was found to restore the scaling behavior by replacing the intermittent laminar flow with turbulent flow.

Thus, the influence of external intermittency on the scaling of the dissipation scale distribution was examined in greater detail for the laminar free-stream condition. Probability density functions of the dissipative scales were compared with, and without, accounting for the external intermittency using an intermittency detection function. Results showed that accounting for the external intermittency produces restores universality in the shapes of the probability density functions at the same wall-normal location at different instances in time. In addition, properly scaling the dissipation-scale-distribution collapses the probability density functions calculated at different wall-normal locations. This improvement in the scaling of the dissipation-scale-distribution supports prior observations of universality of the small-scale description of the turbulence for wall-bounded flow.

KEYWORDS: Turbulence, Turbulent Boundary Layer, Dissipation Scales, External Intermittency, Free-Stream Turbulence, Turbulent/Non-Turbulent Interfaces

Author's signature: Sabah Falih Habeeb Alhamdi

Date: May 31, 2018

INTERMITTENCY EFFECTS ON THE UNIVERSALITY OF LOCAL
DISSIPATION SCALES IN TURBULENT BOUNDARY LAYER FLOWS WITH
AND WITHOUT FREE-STREAM TURBULENCE

By
Sabah Falih Habeeb Alhamdi

Director of Dissertation: Dr. Sean C. C. Bailey

                          Director of Graduate Studies: Dr. Haluk E. Karaca

                                                        Date: May 31, 2018

Dedicated to my dear father, Falih Alhamdi; dear mother, Hashmiya Alhamdi. Dedicated to my dear wife, Zeina; dear son, Ali; dear daughter, Marwah; and dear son, Mustafa.

ACKNOWLEDGMENTS

TABLE OF CONTENTS

LIST OF TABLES

LIST OF FIGURES

Nomenclature

A_n	universal constants
B	constant in log-law equation
c_f	skin friction coefficient
D	dissipation spectrum
E	acquired voltage of the hot-wire probe at the mean streamwise velocity
E_{ii}	wavenumber spectra of velocity components in rectangular co-ordinate, U_i
E_{11}	wavenumber spectra of the streamwise velocity
F_{ii}	frequency spectrum of velocity components in rectangular co-ordinate, U_i
F_{11}	frequency spectrum of the streamwise velocity
f	frequency
f_s	sample frequency
H	shape factor
h	fractal dimension
h_1	channel half-width
I	binary indicator to identify instances where the transition from turbulence to non-turbulence occurs
i	direction index
j	direction index
K	turbulent kinetic energy
k_1	wavenumber in the streamwise direction
k_c	cutoff wavenumber
L	integral length-scale
L^*	mixing length-scale, length-scale based on Townsend's attached eddy hypothesis
M	grid mesh size
n	nth-order of the structure function
P	pressure
p	fluctuating component of the pressure
P_w	wall pressure
Q	probability density function
q	intermittency exponent
R	pipe radius
Re_L	local large-scale Reynolds number
Re_λ	Taylor-scale Reynolds number
Re_λ^*	revised Taylor micro-scale Reynolds number based on the mixing length-scale, L^*
$Re_\lambda^{\mathcal{L}}$	revised Taylor micro-scale Reynolds number based on the alternative large scale, $\mathcal{L}$

Re_θ	Reynolds number based on momentum loss thickness
Re_τ	friction Reynolds number
Re_L^*	Reynolds number based on length-scale of Townsend's attached eddy hypothesis, L^*
r	spacial separation between two points in space
r_i	spacial vector
r_j	spacial vector
r_1	spacial vector in streamwise direction
S_n	longitudinal structure function of the streamwise velocity
S_{2n}	longitudinal structure function of the streamwise velocity proposed by Yakhot and Sreenivasan [1, 2]
T_s	sampling time
t	time
$U_{composite}$	composite streamwise to describe the defect layer
U_i	velocity component in rectangular co-ordinate
U_j	velocity component in rectangular co-ordinate
U_∞	free-stream velocity
U_1	velocity in streamwise direction
U_2	velocity in wall-normal direction
U_3	velocity in spanwise direction
u'	root-mean-square of the turbulence velocity fluctuation in the streamwise direction
u_1	fluctuation velocity in streamwise direction
u_2	fluctuation velocity in wall-normal direction
u_i	fluctuating components of the velocity vector in rectangular co-ordinate
u_j	fluctuating components of the velocity vector in rectangular co-ordinate
u_K	Kolmogorov velocity-scale
u_τ	friction velocity
$u_1 rms$	streamwise turbulence intensity
x	distance in streamwise direction
x_i	direction vector
x_j	direction vector
x_1	distance in streamwise direction
x_2	distance in wall-normal direction
x_3	distance in spanwise direction
Y	mean interface position
y	distance in wall-normal direction

Greek Symbols

γ	average intermittency function
Δt	time increment
δ	boundary layer thickness
δ^*	displacement thickness
δ^+	Kaŕmań number
$\delta_L u$	velocity increment across the local large-scale
$\delta_L u^*$	longitudinal velocity increment across the mixing length-scale, L^*
$\delta_r u$	longitudinal velocity increment in the streamwise direction
$\delta_\eta u$	velocity increment across the local dissipation scale
$\delta_{\mathcal{L}} u$	longitudinal velocity increment across an alternative large scale, $\mathcal{L}$
ε	turbulence kinetic energy dissipation rate
ζ_n	nth-order structure function exponent
η	local dissipative scale
η^*	scaling parameter derived from the mixing length-scale, L^* and its corresponding Reynolds number, Re_L^*
η_{max}	maximum value of local dissipative scale
η_K	Kolmogorov dissipation length-scale
$\eta_{\mathcal{L}}$	scaling parameter derived from the alternative length-scale, $\mathcal{L}$, proposed in this work
η_0	scaling parameter derived from the integral length-scale, L, and its corresponding Reynolds number, Re_L
η_{2n}	local dissipative scale proposed by Yakhot and Sreenivasan [1, 2]
θ	momentum loss thickness
κ	von Kaŕmań constant
λ	Taylor micro-scale
λ^*	revised Taylor micro-scale based on the mixing length-scale, L^*
$\lambda_{\mathcal{L}}$	revised Taylor micro-scale based on the alternative large scale, $\mathcal{L}$
μ	dynamic viscosity
ν	kinematic viscosity
Π	wake parameter
ρ	density of the fluid
σ_Y	standard deviation of the instantaneous interface position, y, relative to the mean interface location, Y
σ	standard deviation of the streamwise velocity
τ	mean total shear stress
τ_K	Kolmogorov time-scale
τ_{ij}	components of the mean total shear stress in rectangular co-ordinate

τ_w	wall shear stress

Other Symbols

$\mathcal{D}$	detection function to identify instances where the transition from turbulence to non-turbulence occurs
$\mathcal{D}_t$	threshold value of the detection function, $\mathcal{D}$
$\mathcal{L}$	alternative large scale
ℓ	sensing length of hot-wire probe
ℓ_t	length of a turbulent interval
ℓ_{nt}	length of a non-turbulent interval
ℓ_ν	viscous length-scale
$\mathcal{T}$	time increment in Equation (6.7)
$\mathcal{T}_c$	cut-off time in Equation (6.7)
$\mathcal{W}$	wake function

Other Notation

$\lvert \; \rvert$	absolute value
$\langle \; \rangle$	denotes an ensemble average
$(\;)^+$	denotes normalization using inner parameter, friction velocity and viscous length-scale
$f()$	function of
$g()$	function of
$\mathcal{O}()$	order of magnitude

Acronym

const	constant
DNS	direct numerical simulation
KTH	Royal Institute of Technology
PDF	probability density function
RANS	Reynolds average Navier-Stokes
RTD	resistance temperature detection
ZPG	zero pressure gradient

Latin Acronym

et al.	Et alii means "and others"
e.g.	exempli gratia means "for example"
i.e.	id est means "in other words"

Chapter 1 Introduction

1.1 Turbulence

In physics and fluid dynamics, flowing fluids can be classified as being laminar, turbulent, or transitional flows. These three classifications of flow can typically be observed in cigarette smoke, as shown in Figure (1.1). In laminar flow, the flow streamlines follow smooth, regular, paths that are approximately parallel with one another. However, these streamlines form complex patterns and interweave with each other in turbulence, which is characterized by the formation of eddying motion. Transitional flow is a mixture of these two states, containing features of both laminar and turbulent flow.

One result of laminar flow is that for steady boundary conditions the velocity of the fluid is also steady, constant in both time and space; conversely, turbulent flow for the same boundary conditions is highly unsteady. The unsteady nature of turbulent flow lends itself to a statistical approach to analysis and evaluation, and prediction of these flows often relies on being able to model the impact of the small-scale turbulent motions on the large-scale dynamics.

Most flowing fluids are turbulent, and thus turbulence represents the dominant physics in many types of engineering applications. Therefore, the understanding of turbulent behavior in flowing fluids is one of the most intriguing and significant problems in all classical physics. Although strict definition eludes us, turbulence is commonly defined as being a highly chaotic fluid motion that is described by random velocity fluctuation in both time and space. In both internal (e.g. pipe and channel flow) and external (e.g. boundary layer) wall-bounded flows, turbulence is characterized by an increase in the frictional forces applied by the fluid on sold
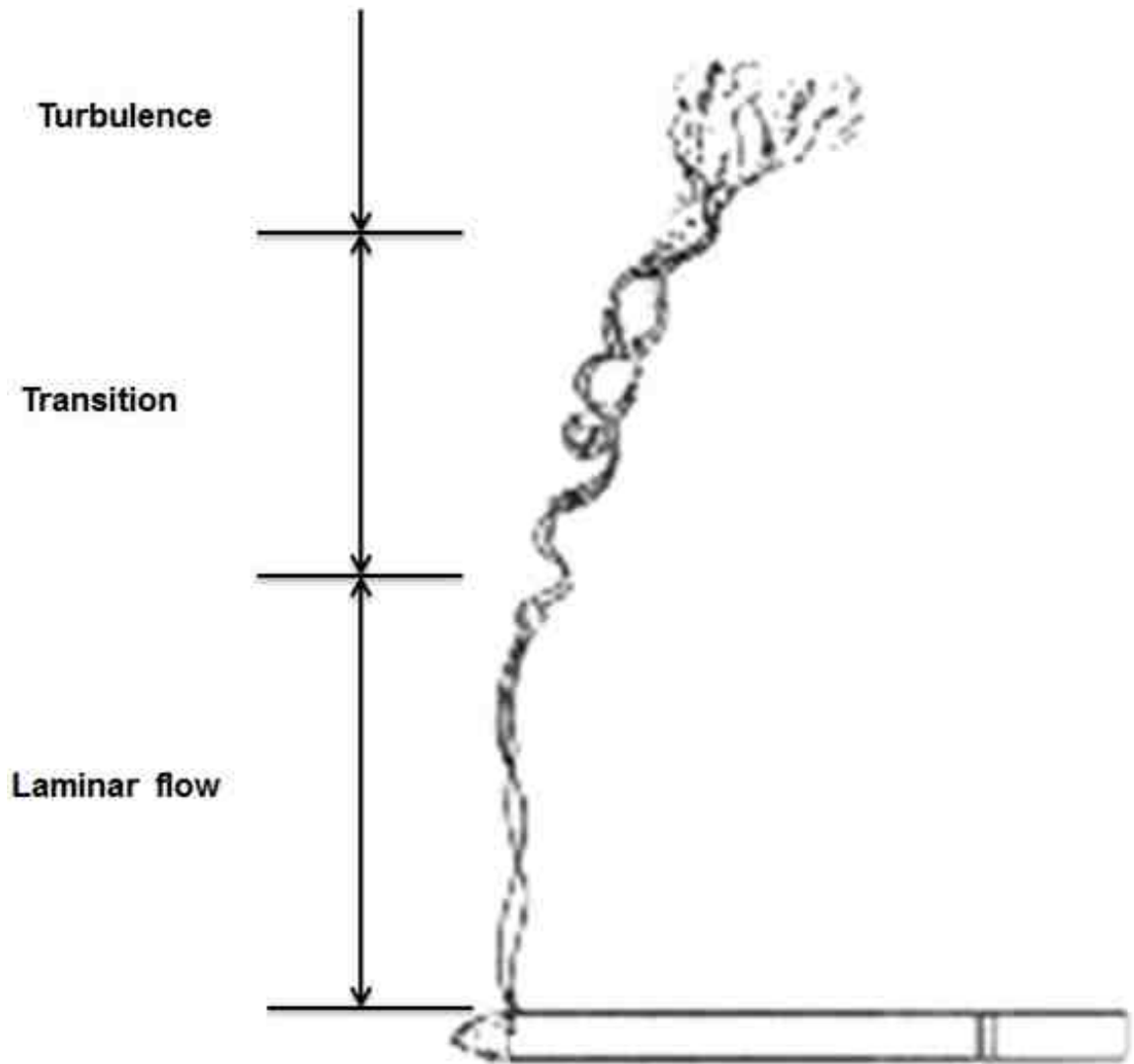
Figure 1.1: Illustration of the laminar, transition and turbulence from cigarette smoke.

surfaces.

A critical parameter for predicting turbulent behavior is the ratio of the inertial forces to viscous forces within the fluid. This ratio is called Reynolds number and is an important dimensionless quantity in fluid mechanics that describes, for example, the stability conditions of the flow. If the Reynolds number increases sufficiently then cascading instabilities cause laminar flow to transition to turbulent flow. The disorganized motion of turbulence leads to a significant increase in the rate of mixing

and diffusion of mass, momentum and energy through a cascade of turbulent interactions. These interactions occur over a range of temporal and spatial scales, with the separation between the largest scales of turbulence, to the smallest ones, described by the Reynolds number.

Once turbulent, a turbulent flow can be classified as statistically homogeneous or inhomogeneous, with further classification provided by its degree of isotropy. Homogeneous turbulence is such that its statistically averaged properties are independent of location. However, it is also possible for flows to be partially homogeneous if it is statistically homogeneous in one or two Cartesian directions. Turbulence is classified as been isotropic if its statistics are independent of rotation and reflections. If this is not the case, it is classified as being anisotropic.

Finally, a turbulent flow of sufficiently high Reynolds number can be homogeneous in the statistics of the small-scale turbulence, even though it is inhomogeneous in the statistics of the larger scales. This homogoeneity is achieved through a cascade process, by which kinetic energy is transferred from larger scales to smaller scales, through breakup of larger scale eddies into smaller scale ones. Through this cascade of interactions, the inhomogeneity of the larger scale eddies is lost, resulting in small scale homogeneity and isotropy.

1.2 Turbulence Features

Although a formal definition of turbulence is elusive, turbulence exhibits some common features that can be used to distinguish turbulence from other phenomena in fluids mechanics. In particular, a turbulent flow can be characterized to exhibit all of the following features:

- Turbulent flows are highly disorganized, chaotic and seemingly random behavior.

- Non-repeatability (i.e., sensitivity to initial conditions [1]) is one of the physical features that can be observed in turbulent flows. This sensitivity in chaos theory refers to the behavior of the dynamical system that can change drastically due to small changes in the initial conditions [3].

- Turbulent flows exhibits extremely large range of length and time-scales, although the smallest scales are still large enough to satisfy the continuum hypothesis.

- Turbulence enhances mixing (diffusion) and dissipation of mass, momentum and energy. Both diffusion and dissipation are mediated by viscosity at molecular scales. Through viscous shear stresses, turbulent flows convert kinetic energy of the velocity fluctuation into internal energy without a form of production. Thus, turbulence would eventually decay back to laminar state, unless provided with a source of kinetic energy.

- Turbulent flows are three-dimensional, time-dependent and rotational. The irrationality of a potential flow is due to its definition (the curl of the gradient of a property equal to zero); therefore, potential flow cannot be turbulent. Turbulent flows are described by high levels of vorticity and the mechanism of vortex stretching.

- Turbulent flows are intermittent in both space and time [2].

---

[1] Turbulence exhibits this sensitivity to initial conditions because of successive instabilities, which are experienced during the transition process. The sensitivity generally increases with the order of statistical moment. Thus, replicating the experiment in turbulence, data may not match. Therefore, replications must match statistically.

[2] It should be distinguished between intermittency from the transition to turbulence and reversion of turbulent to laminar flow (relaminarization). The transition to turbulence is the process of instability of a laminar flow that leads to turbulent flow, while the transition from turbulent flow to laminar one is called relaminarization [4].

1.3 Turbulence in Engineering

Turbulence has many characteristics that make its prediction and control an important and challenging task in engineering. Turbulent flows are generally characterized by an increase in shear forces (skin friction) exerted by the fluid on sold surfaces in both internal and external flows (e.g. flow through pipes, flow between two axial compressor blades [5], and flow around an airplane). Turbulence can effect the vibration and noise experienced by objects, where pressure fluctuations in turbulence lead to an increase in noise level. Turbulence also results in undesirable effects, such as a decrease of efficiency and the need for high power and thrust in a turbomachine due to the loss of energy to the turbulence.

However, turbulence can also be beneficial to thermal systems. Heat exchangers, combustion chambers, nuclear reactors and chemical reactors are more efficient due to turbulence, as it induces mixing of mass, momentum and heat in these systems. An aerodynamic application of turbulence is the tripping of a laminar boundary layer on a wing to force transition to turbulence in order to delay or prevent flow separation at large angles of attack.

1.4 External Intermittency in Turbulent Wall-Bounded Flows

External intermittency in turbulent flows describes the process by which a fixed location in space might experience intermittent switching between turbulent and non-turbulent states as a function of time. Alternately, it can also describe a condition whereby at a fixed time, both laminar and turbulent conditions can be intermittently distributed in space. Of particular interest in this work, is the external intermittency that can be observed in the outer region of wall-bounded flows. In this region, the turbulent boundary layer forms bulges of turbulent fluid that has been transported away from the surface. The result is that, at a fixed point a fixed distance from the

wall, as these bulges advect with the mean flow the fixed point will experience periods of laminar flow, interspaced with periods of turbulent flow when a bulge advects past the point of interest. External intermittency can be observed in Figure (6.2), which shows smoke-wire flow visualization of a turbulent boundary layer. It can be observed that there are instances where the free-stream flow extends very close to the wall.

This external intermittency can be quantified by the ratio of the length of the turbulent segments to the length of the total segment at any point. Thus, it measures the probability of having turbulent flow at any instant at the considered point. This intermittency increases with the wall-normal location in wall-bounded flows until the free-stream is reached, whereby the flow is typically laminar.

1.5 Motivation and Objective

In most of the fluid systems of engineering interest, the flow is turbulent and bounded by one or more solid surfaces [6]. Within these systems, turbulence greatly enhances mixing (diffusion) and dissipation of mass, momentum and energy. As a result, it is of great fundamental and practical importance.

Modeling the smallest eddies in wall-bounded flows is important to improve simulations, which can, for example, predict and improve the performance of devices in industrial applications, or controlling the turbulence in others. Thus, to aid in the modeling of these smallest scales of turbulence, the objective of this dissertation is to measure the distribution of the smallest, dissipative scales of turbulence within turbulent boundary layer and to provide some predictive capability of their behavior by understanding their scaling behavior. Specifically, the objective is to investigate the scaling of the probability density functions (PDFs) of the spatial scales at which dissipation occurs within wall-bounded flows. To achieve this goal, experiments were conducted in a turbulent boundary layer developing within both laminar and turbulent free-streams. These results are used to calculate the PDFs of local

dissipative scale, η, at various distances from the wall and investigate the validity of a wall-distance dependent length-scale, and also to evaluate a proposed alternative description for the large-scale L. Furthermore, a procedure was developed to account for the external intermittency in the outer layer in order to improve the overall scaling of the local dissipation scales in the turbulent boundary layer flow.

Chapter 2 Background

2.1 Reynolds-Averaged Equations

The following section will introduce Reynolds decomposition to derive of the Reynolds-Average Navier Stokes (RANS) equation from the governing equations of flow motion. The equations of the flow motion are the continuity and the Navier-Stokes equations. The incompressible form of the continuity equation is

$$\frac{\partial U_i}{\partial x_i} = 0, \tag{2.1}$$

and the simplified form of the Navier-Stokes equations, by assuming incompressible fluid flow, negligible body forces and constant viscosity, are

$$\frac{\partial U_i}{\partial t} + U_j \frac{\partial U_i}{\partial x_j} = -\frac{1}{\rho} \frac{\partial P}{\partial x_i} + \nu \frac{\partial^2 U_i}{\partial x_j \partial x_j} \quad , \quad i = 1, 2, 3. \tag{2.2}$$

In these equations, U_i denotes the components of the instantaneous local velocity vector, t denotes time, x_j indicates spatial location, P is pressure, ν is the kinematic viscosity, and ρ is the density of the fluid. This system of four equations consists of the four unknowns U_1, U_2, U_3 and P. The convective term, $U_j \frac{\partial U_i}{\partial x_j}$, is non-linear; therefore, it is very difficult to practically find analytical solution for this system of equations.

Using Reynolds decomposition, we can say that

$$U_i = \langle U_i \rangle + u_i \quad and \quad P = \langle P \rangle + p, \tag{2.3}$$

in which u_i and p refer to the fluctuating components of the velocity vector and the pressure, respectively. Here, $\langle \, \rangle$ denotes an ensemble-averaged quantity. The expressions in Equation (2.3) can be substituted into Equations (2.1) and (2.2), and averaging over all terms of these equations to get the Reynolds-Averaged equations.

The continuity equation for incompressible fluid becomes

$$\frac{\partial(\langle U_i \rangle + u_i)}{\partial x_i} = 0. \tag{2.4}$$

Averaging this equation leads to

$$\frac{\partial \langle U_i \rangle}{\partial x_i} + \frac{\partial u_i}{\partial x_i} = 0. \tag{2.5}$$

Eliminating the vanishing term, $\frac{\partial \langle u_i \rangle}{\partial x_i} = 0$, we deduce the continuity equation for the mean

$$\frac{\partial \langle U_i \rangle}{\partial x_i} = 0. \tag{2.6}$$

Subtracting this equation from Equation (2.5), the continuity equation for the fluctuation can be obtained

$$\frac{\partial u_i}{\partial x_i} = 0. \tag{2.7}$$

The previous two equations are decoupled from each other because of the linearity of the continuity equation.

Introducing the Reynolds decomposition into the Navier-Stokes equations, Equation (2.2) can be expressed as

$$\frac{\partial(\langle U_i \rangle + u_i)}{\partial t} + (\langle U_j \rangle + u_j)\frac{\partial(\langle U_i \rangle + u_i)}{\partial x_j} = -\frac{1}{\rho}\frac{\partial(\langle P \rangle + p)}{\partial x_i} + \nu\frac{\partial^2(\langle U_i \rangle + u_i)}{\partial x_j \partial x_j}. \tag{2.8}$$

Averaging the entire equation with canceling the vanishing terms as what we did with the continuity equation, the Navier-Stokes equations for the mean can be written as

$$\frac{\partial \langle U_i \rangle}{\partial t} + \langle U_j \rangle\frac{\partial \langle U_i \rangle}{\partial x_j} + \frac{\partial \langle u_i u_j \rangle}{\partial x_j} = -\frac{1}{\rho}\frac{\partial \langle P \rangle}{\partial x_i} + \nu\frac{\partial^2 \langle U_i \rangle}{\partial x_j \partial x_j}. \tag{2.9}$$

The last term on the left-hand side can be expanded by applying the derivative of the product of two functions with using the continuity equation for the fluctuations, Equation (2.7). Then it easily follows

$$\frac{\partial \langle u_i u_j \rangle}{\partial x_j} = \langle u_j \frac{\partial u_i}{\partial x_j} \rangle. \tag{2.10}$$

These terms have no equivalent in the original form of the Navier-Stokes equations and it comes from the non-linear advective term. These terms describe the transport of momentum fluctuation by the fluctuation velocity. Therefore, additional unknowns are introduced to the Navier-Stokes equations for the mean velocity and pressure field. These terms are usually called the Reynolds stress tensor although a check of dimensions illustrates that they are not stresses; they must be multiplied by the density, ρ. To have more appropriate dimensions of stresses, the components of the tensor, $-\rho\langle u_i u_j \rangle$, are called Reynolds stresses with the Reynolds normal stresses if $i = j$ and the Reynolds shear Stresses if $i \neq j$ as well as this tensor is symmetric. These terms demonstrate that the velocity fluctuations have an impact on the mean flow by exchanging momentum with the mean flow through the Reynolds stress. Unlike the system of incompressible form of continuity equation and the Navier-Stokes equations that is closed, introduction of the six unknowns from the Reynolds stress tensor results in the requirement of additional equations to solve for the new unknowns. Manipulating the equations of motions to find additional transport equations for $\langle u_i u_j \rangle$ introduces even more unknowns. This leads to the so-called "turbulent closure problem"[7]. The RANS equation can be written as

$$\frac{\partial \langle U_i \rangle}{\partial t} + \langle U_j \rangle \frac{\partial \langle U_i \rangle}{\partial x_j} = -\frac{1}{\rho} \frac{\partial \langle P \rangle}{\partial x_i} + \nu \frac{\partial^2 \langle U_i \rangle}{\partial x_j \partial x_j} - \frac{\partial \langle u_i u_j \rangle}{\partial x_j}. \qquad (2.11)$$

2.2 Turbulent Wall-Bounded Flows

The following section will introduce some of the common terminology used in the study of turbulent wall-bounded flows, with focus on turbulent boundary layer flow, the type of flow used for this study. Turbulent boundary layer flow as an external wall-bounded flow shares common physical characteristics with internal wall-bounded flows (e.g. channel and pipe flows) within a region close to the boundary surface. Therefore, most of the concepts introduced here will also be valid in both internal and external wall-bounded flows. For more information and details, the interested reader

10
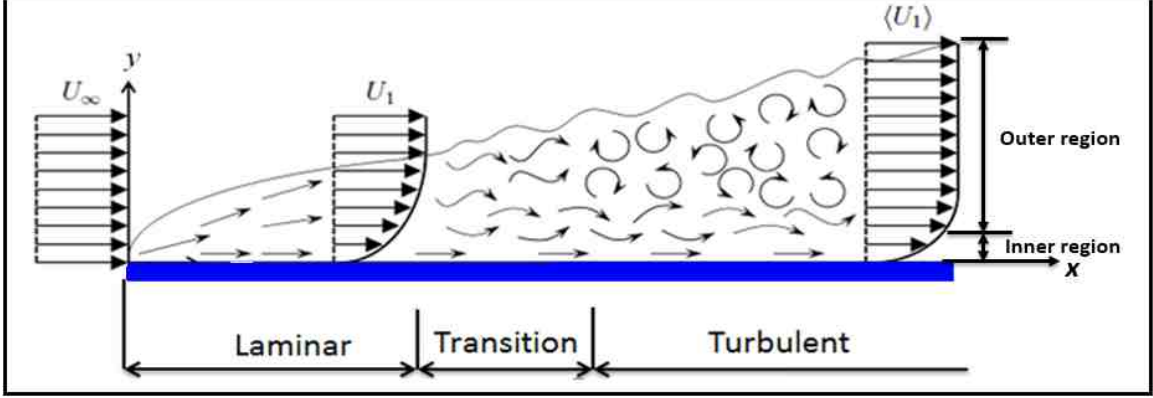
Figure 2.1: Illustration of the laminar, transition and turbulence with the inner and outer regions for turbulent boundary layer developing along flat plate.

may be referred to the classical and modern turbulence textbooks [8, 9, 10, 11, 12, 13, and others].

We assume turbulent flow on a flat plate with zero pressure gradient (ZPG) conditions, $\partial P/\partial x_1 = 0$, that coexists with a constant free-stream velocity, U_∞, in the downstream directions. Here, x_1, x_2 and x_3 are the streamwise, wall-normal and spanwise directions, respectively, with U_1, U_2, U_3 and P the corresponding velocity components and pressure. The distance across the boundary layer from the surface to the free-stream is the the boundary layer thickness, $\delta(x_1)$, which is function of the streamwise direction. The growth of the boundary layer on a flat plate illustrates in Figuree (2.1), which show the transition from laminar to turbulent boundary layer with the inner and outer regions of this external wall-bounded flow. In this figure, the wall-normal direction is $y = x_2$ and the streamwise direction is $x = x_1$.

The RANS under steady flow assumption can be written as

$$\langle U_j \rangle \frac{\partial \langle U_i \rangle}{\partial x_j} = -\frac{1}{\rho} \frac{\partial \langle P \rangle}{\partial x_i} + \frac{1}{\rho} \frac{\partial \tau_{ij}}{\partial x_j}, \tag{2.12}$$

where the components of the mean total shear stress in rectangular co-ordinate are

$$\tau_{ij} = \mu \left(\frac{\partial \langle U_i \rangle}{\partial x_j} + \frac{\partial \langle U_j \rangle}{\partial x_i} \right) - \rho \langle u_i u_j \rangle, \tag{2.13}$$

in which $\mu\left(\frac{\partial\langle U_i\rangle}{\partial x_j} + \frac{\partial\langle U_j\rangle}{\partial x_i}\right)$ is the laminar stress tensor with μ is the dynamic viscosity of the fluid, and $-\rho\langle u_i u_j\rangle$ is the turbulent stress tensor.

The two-dimensional, incompressible, steady flow, negligible gravity effects, streamwise mean momentum equations with the boundary layer approximation and employing Reynolds decomposition [7], and the incompressible continuity equation are

$$\frac{\partial\langle U_1\rangle}{\partial x_1} + \frac{\partial\langle U_2\rangle}{\partial x_2} = 0, \tag{2.14}$$

$$\langle U_1\rangle\frac{\partial\langle U_1\rangle}{\partial x_1} + \langle U_2\rangle\frac{\partial\langle U_1\rangle}{\partial x_2} = -\frac{1}{\rho}\frac{\partial\langle P\rangle}{\partial x_1} + \frac{1}{\rho}\frac{\partial\tau}{\partial x_2}. \tag{2.15}$$

The means of Bernoulli's equation can be used to substitute the pressure gradient terms. In that way, this term can be written in terms of the free-stream velocity and its gradient in streamwise direction, as follows

$$\langle P\rangle + \frac{1}{2}\rho U_\infty^2 = const \tag{2.16}$$

$$\frac{d\langle P\rangle}{dx_1} + \rho U_\infty\frac{dU_\infty}{dx_1} = 0 \tag{2.17}$$

$$\frac{d\langle P\rangle}{dx_1} = -\rho U_\infty\frac{dU_\infty}{dx_1}. \tag{2.18}$$

For turbulence, we have adopted the short notation for the mean total shear stress, τ,

$$\tau = \mu\frac{\partial\langle U_1\rangle}{\partial x_2} - \rho\langle u_1 u_2\rangle, \tag{2.19}$$

here, $-\rho\langle u_1 u_2\rangle$ refers to streamwise-wall-normal Reynolds stress. For ZPG condition (no pressure source), the pressure gradient term vanishes. For fully developed flows, such that channel, pipe and boundary layer flows, the streamwise derivatives of the Reynolds normal stresses and the convective terms can be canceled. Equation (2.15)

can be integrated from the wall to the free-stream to yield the so called von Kármań integral momentum equation.

$$\frac{\tau_w}{\rho} = \frac{d}{dx_1}\Big[U_\infty^2 \int_0^\infty \frac{\langle U_1(x_1, x_2)\rangle}{U_\infty}\big(1 - \frac{\langle U_1(x_1, x_2)\rangle}{U_\infty}\big)dx_2\Big] + U_\infty \frac{dU_\infty}{dx_1} \int_0^\infty \big(1 - \frac{\langle U_1(x_1, x_2)\rangle}{U_\infty}\big)dx_2,$$

(2.20)

here, since the order of magnitude of the Reynolds normal stresses contribution is less than the order of the leading term, this contribution can be neglected[1]. τ_w is the wall shear stress and depends on the distance from the wall in the streamwise direction, x_1. For a non ZPG flow, U_∞ depends also on x_1 distance. Thus, the two well known integral properties of the boundary layer, the displacement thickness, δ^* and the momentum thickness, θ, can be expressed as

$$\delta^*(x_1) = \int_0^\infty \left[1 - \frac{\langle U_1(x_1, x_2)\rangle}{U_\infty}\right] dx_2$$

(2.21)

and

$$\theta(x_1) = \int_0^\infty \frac{\langle U_1(x_1, x_2)\rangle}{U_\infty}\left[1 - \frac{\langle U_1(x_1, x_2)\rangle}{U_\infty}\right] dx_2.$$

(2.22)

These two integral properties depend on δ; however, this dependence can be eliminated by divided the first parameter on the second parameter to get the shape factor, H, which is often utilized as an indicator of the fullness of the velocity profile. Substituting these two thicknesses into Equation (2.15), This equation simplifies to

$$\frac{\tau_w}{\rho U_\infty^2} = \frac{d\theta}{dx_1} + \frac{1}{U_\infty}\frac{dU_\infty}{dx_1}\big[2\theta + \delta^*\big].$$

(2.23)

Introducing the definition of the skin friction coefficient, c_f, simplifies this equation to

$$c_f = \frac{\tau_w}{\frac{1}{2}\rho U_\infty^2} = 2\frac{d\theta}{dx_1} + \frac{2}{U_\infty}\frac{dU_\infty}{dx_1}(\delta^* + 2\theta).$$

(2.24)

Therefore, the measurements of the velocity profile at some different downstream positions can lead to determine the skin friction coefficient. Note that when using Equation (2.24), well resolved mean velocity profile is needed to be ensured.

---

[1]For example, Schlatter et al. [14] demonstrates that the contribution of this neglected term is about 50 times less than the leading order term for $Re_\theta = 2500$

13

Furthermore, for a flat plate, the previous two equation can be reduce to

$$\frac{\tau_w}{\rho U_\infty^2} = \frac{d\theta}{dx_1} \tag{2.25}$$

and

$$c_f = 2\frac{d\theta}{dx_1},, \tag{2.26}$$

These two equations show that the rate of change of momentum lost is controlled by the wall shear stress.

In internal flows, such that flows in pipes and channels, the streamwise momentum equation (Equation (2.15) or its equivalent in cylindrical coordinates) can be utilized to illustrate the dependence of the wall shear stress on the pressure drop such that

$$\tau_w = -\delta\frac{d\langle P_w\rangle}{dx_1} \tag{2.27}$$

and

$$\tau_w = -\frac{\delta}{2}\frac{d\langle P_w\rangle}{dx_1}, \tag{2.28}$$

in which $\langle P_w\rangle$ refers to the wall-mean pressure, and δ corresponds to the pipe radius, R, in pipe flows and the channel half-width, h_1, in channel flows. The static pressure can be estimated using the Pitot Static tube and pressure taps hence the wall shear stress can be found experimentally. Usually, the wall shear stress is calculated from indirect ways. However, one reason of using other methods than the pressure drop to find the wall shear stress is to avoid not satisfying the implicit assumptions. For example, in internal flows, the convective terms in momentum equation can be neglected only under fully developed conditions that need large channel heights or pipe diameters to meet the required hydrodynamic entrance length depending on Reynolds number. Another example, to meet the two-dimensional flow assumption in channels, a large aspect ratio (width-to-length ratio) is required.

The momentum equation in the wall-normal direction shows that the summation of the Reynolds stress in wall-normal direction, $\langle u_2^2\rangle$, and the pressure, $\langle P\rangle$, is

14

solely related to the streamwise coordinate. This relationship and Equation (2.27) substituted in the integration of Equation (2.15) to obtain

$$\tau = \tau_w \left(1 - \frac{x_2}{\delta}\right). \tag{2.29}$$

This equation shows that, in the near-wall region when $x_2/\delta \ll 1$, the total shear stress is approximately constant and equals to the wall shear stress. Thus, there exists a layer in the turbulent wall-bounded flows (i.e. turbulent channel, pipe and boundary layer flows) does not depend on the geometry and dimensions of the flow but depend on the wall shear stress. Therefore, in this near-wall region, a velocity and length-scale can be obtained from Equation (2.19) and Equation (2.29) as follows

$$u_\tau = \sqrt{\frac{\tau_w}{\rho}} \tag{2.30}$$

and

$$\ell_\nu = \frac{\nu}{u_\tau}, \tag{2.31}$$

which are the well-known friction velocity, u_τ and viscous length-scale, ℓ_ν, that used to scale the inner region in wall-bounded flow. These three parameters and the distance from the wall describe the condition of the near wall region.

Substituting Equation (2.19) into Equation (2.29) with $\tau_w = \rho u_\tau^2$ from from Equation (2.30), one gets

$$\nu \frac{d\langle U_1 \rangle}{dx_2} - \langle u_1 u_2 \rangle = u_\tau^2 \left(1 - \frac{x_2}{\delta}\right). \tag{2.32}$$

This equation can be rewritten as

$$\frac{d(\langle U_1 \rangle / u_\tau)}{d(x_2 u_\tau / \nu)} - \frac{\langle u_1 u_2 \rangle}{u_\tau^2} = \left(1 - \frac{x_2}{\delta}\right), \tag{2.33}$$

and rearranged by introducing to

$$\frac{dU_1^+}{dy^+} - \langle u_1 u_2 \rangle^+ + \frac{y^+}{\delta^+} = 1, \tag{2.34}$$

in which the $+$ indicates the scaling with viscous units, u_τ and ℓ_ν, and δ^+ is well-known Karmán number that is the ratio between the outer and inner length-scale,

$\delta u_\tau/\nu$, which is equivalent to the the friction Reynolds number, Re_τ. In the near-wall region when $y^+ << \delta^+$ the more the scales are separated, Equation (2.34) becomes

$$\frac{dU_1^+}{dy^+} - \langle u_1 u_2 \rangle^+ = 1, \tag{2.35}$$

which allowed self-similar solutions $f(y^+) = u^+$ and $g(y^+) = -\langle u_1 u_2 \rangle^+$. The first solution is the well-known as the law of the wall.

2.3   The Development of Turbulent Wall-Bounded Flows

Unlike the laminar boundary layer, there are two regimes governed by different sets of flow scales can be observed in turbulent boundary layer flow as a turbulent wall-bounded flow. These two sets of scales are the inner and outer scaling. The inner scaling is the normalization of the statistics of turbulence using the inner parameter, friction velocity and viscous length-scale, in the so-called inner region. However; the statistics of turbulence in the outer region are scaled using the outer scaling parameters that are the turbulent boundary layer thickness and the free-stream velocity in turbulent boundary layer flow. The inner and outer regions of turbulent wall-bounded flows with their specific layers as shown in Figure (2.2) will be discussed farther in the next two subsections. Figure (2.2) represents mean streamwise velocity profiles for a Reynolds number, $Re_\tau = 1000$, together with illustration of the inner and outer regions of typical turbulent boundary layer. The inner region consists the viscous sublayer, buffer and overlap layers, and the outer or wake region comprises of the overlap, defect (core) and potential layers.

2.3.1   The Inner Region

For sufficiently enough Reynolds number, there are three layers can be observed in the inner region of turbulent wall-bounded flows. These layers are the viscous sublayer, the buffer layer and the logarithmic layer that an overlap layer between the inner and

16
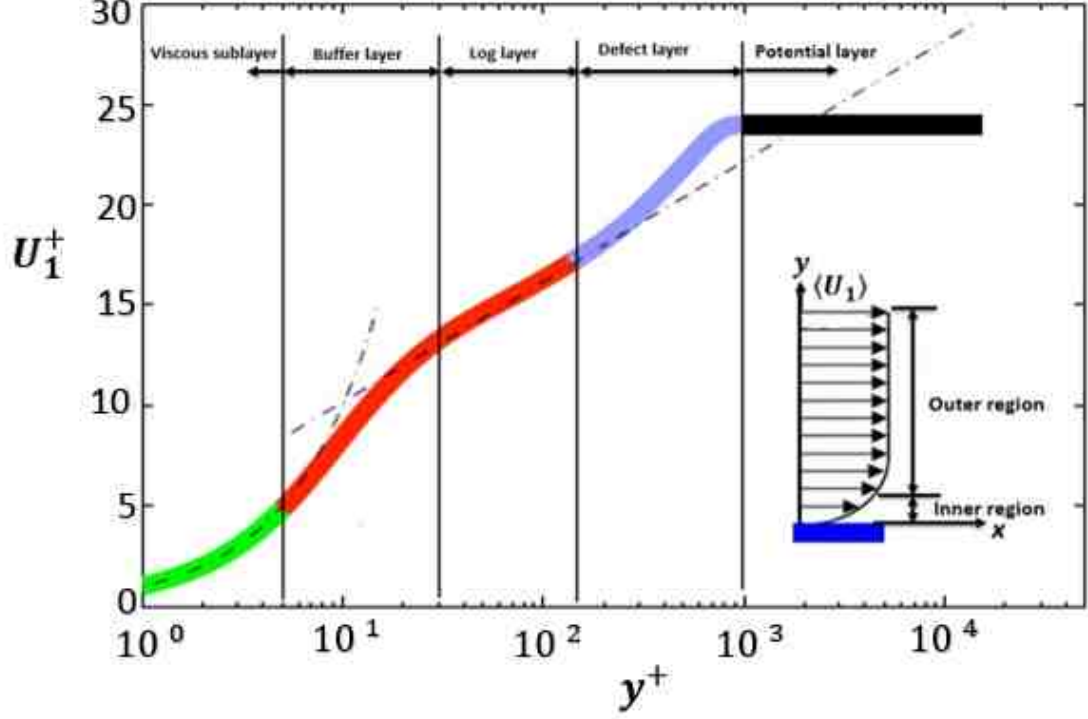
Figure 2.2: Streamwise mean velocity profile for ZPG turbulent boundary layer developing along flat plate calculated through the composite profile description of Chuahan et al. [15] for $Re_\tau = 1000$ with illustration of the inner and outer regions of typical turbulent boundary layer.

outer regions of the turbulent wall-bounded flows. These layers will be discussed in the following three subsections.

2.3.1.1 The Viscous Sublayer

The viscous sublayer is extremely close to the wall layer that is near a no-slip boundary. Turbulent motions are dampened severely by friction in this layer; therefore, the turbulent shear stress, $-\rho\langle u_1 u_2 \rangle$, is relatively small comparing to the viscous (laminar) shear stress, $\mu\frac{d\langle U_1 \rangle}{dy}$, in this sublayer. Hence, the simplified form of momentum equation, Equation (2.35), becomes:

$$\frac{dU_1^+}{dy^+} = 1, \tag{2.36}$$

17

in which $U_1{}^+$ is the inner-scaled streamwise mean velocity defined such that

$$U_1{}^+ = \frac{\langle U_1 \rangle}{u_\tau},$$ (2.37)

and y^+ refers to the inner-scaled position normal to the wall expressed as

$$y^+ = \frac{y u_\tau}{\nu}.$$ (2.38)

The simple linear solution of Equation (2.36) that describes this sublayer is

$$U_1^+ = y^+.$$ (2.39)

The range of this layer is found satisfactorily with experimental data for smooth surface to be roughly $0 \leq y^+ \leq 5$ as highlighted in green in Figure (2.2).

2.3.1.2   The Log(arithmic) Layer

The logarithmic sublayer is also known as the log layer. It is a logarithmic semi-empirical result that accurately describes the variation of velocity with the wall-normal distance in that region of turbulent wall-bounded flows. It corresponds to scaled distances relatively far from the wall depending on Reynolds number. This layer is also called the inertial subrange where it has some analogy with the inertial subrange of the spectrum of a locally isotropic turbulence. Since the viscous dissipation is negligible in the inertial subrange, the viscous shear stresses are negligible in this layer. This layer describes by the well-known law of the wall (log-law):

$$U_1{}^+ = \frac{1}{\kappa} \; ln \; y^+ \; + \; B.$$ (2.40)

The variation of the velocity across the wall-normal distance depends on the choice of von Kaŕmań constant, κ, and the constant B. The lower limit of the log layer is roughly when $y^+ = 30$, with the upper limit depending on the Reynolds number in wall-bounded flows.

18

2.3.1.3 The Buffer Layer

The layer between the viscous sublayer and the log layer in turbulent wall-bounded flows is called the buffer layer. It really comes from experiments where there is not analytical solution to determine the velocity variation in this layer. It is expected that this layer is matched the overlap region between the viscous sublayer and the log layer in order to obtain a well-defined global treatment for the velocity profile as demonstrated in Figure (2.2).

2.3.2 The Outer Region

Although the log-law is generally accepted to be universal in the outer region, boundary conditions (e.g., pressure gradient and Reynolds number) play a large rule in describing the variation of the mean velocity and statistics in the outer region of turbulent wall-bounded flows. The mean streamwise velocity distribution with the wall-normal distance in this region depends also on the flow type in turbulent wall-bounded flow. This region consists of part of the log layer as well as the defect layer and the potential layer that will be explained in the next two subsections.

2.3.2.1 The Defect Layer

The defect layer, sometimes called the "wake layer"or "outer layer", is the layer of a turbulent wall-bounded flow beyond the log layer as shown in Figure (2.2). It begins approximately one-tenth the boundary layer thickness from the wall in turbulent boundary layer flow.

In addition to the log-law function that describes the log layer, Equation (2.40), a number of composite functions for the mean streamwise velocity has been introduced in the literature as a valid description for the entire flow region. Sometimes, the composite velocity profile is given by the superposition of the description for the log-law plus a functional form to describe the wake function. Based on one of the first

formal descriptions for the defect layer that proposed by Coles [16]. A functional form for this layer can thus be given as

$$U^+_{composite} = \frac{1}{\kappa} \; ln \, y^+ \; + \; B \; + \frac{2\Pi}{\kappa} \; \mathcal{W} \; \frac{y^+}{\delta^+}, \qquad 0 \; \leq \; y^+ \; \leq \; \delta^+, \qquad (2.41)$$

in which Π is the wake parameter and $\mathcal{W}$ is the wake function. After that, a number of wake functions have been proposed. For a summary of more prominent complete functional forms of the defect layer, the reader can be referred to Appendix E of Örlü [17].

2.3.2.2 The Potential Layer

The potential layer is the layer beyond the defect layer that reaches the centerline in pipe flow and it is the free-stream in turbulent boundary layer. In this region the velocity remains at the initial entrance velocity in internal wall-bounded turbulence and the free-stream velocity in turbulent boundary layer.

Chapter 3 Literature Review

3.1 Kolmogorov Hypothesis

One of the most significant theories in the study of turbulence is the universal equi-
librium hypothesis of Kolmogorov [18], which postulates that the small scales of
turbulence are homogeneous and statistically isotropic, and that, due to a cascade
of kinetic energy from the largest scales of turbulence to the smallest scales, the
smallest scales become disconnected from the boundary conditions and thus become
uniquely and universally dependent only on the mean rate of dissipation of turbulent
kinetic energy, $\langle \varepsilon \rangle$, and the kinematic viscosity, ν. The rate of dissipation, ε, can be
estimated through

$$\varepsilon = \frac{\nu}{2} \left(\frac{\partial u_i}{\partial x_j} + \frac{\partial u_j}{\partial x_i} \right)^2, \tag{3.1}$$

Through dimensional analysis of $\langle \varepsilon \rangle$ and ν, length, velocity and time-scales corre-
sponding to the dissipation of kinetic energy can be formed. These scales are the
Kolmogorov dissipation length-scale (η_K), the Kolmogorov velocity-scale (u_K), and
the Kolmogorov time-scale (τ_K), which is expressed by Pope [8] as

$$\eta_K \sim (\nu^3/\langle \varepsilon \rangle)^{1/4}, \tag{3.2}$$

$$u_K = (\nu \langle \varepsilon \rangle)^{1/4}, \tag{3.3}$$

and

$$\tau_K = (\nu/\langle \varepsilon \rangle)^{1/2}. \tag{3.4}$$

The existence of a universal equilibrium region was heavily tested in the succeeding
decades and, as a result, there is a great amount of evidence to support Kolmogorov's

concept of small-scale universality, most notably through the collapse of the energy spectra scaled by ν, $\langle \varepsilon \rangle$ and η_K in the dissipation region [19, 20, and others].

Key to these theories is the energy cascade process by which energy is transferred from large energy-producing eddies, described by the integral length-scale L, down to the smallest eddies, characterized by η_K. Given sufficient separation of these scales, within the universal equilibrium range, there will be an inertial subrange where the turbulent dynamics depend only on $\langle \varepsilon \rangle$ and not ν.

3.2   The Structure Function

When the spatial separation between two points in space, represented by a vector with components r_j, lies in this inertial subrange such that $L >> |r| >> \eta_K$, the longitudinal structure function of the streamwise velocity, S_n, should follow power-law behavior such that

$$S_n \equiv \langle (\delta_r u)^n \rangle = A_n \left(\frac{|r|}{L} \right)^{\zeta_n}, \tag{3.5}$$

where A_n are universal constants and $\delta_r u$ represents the longitudinal velocity increment defined as

$$\delta_r u \equiv (u_i(x_j + r_j) - u_i(x_j)) \left(\frac{r_i}{|r|} \right). \tag{3.6}$$

Kolmogorov's theory indicated that $\zeta_n = n/3$. However, experimental investigations, e.g., the work of Anselmet et al. [21], have shown that ζ_n differs from this linear scaling and has nonlinear dependence on n. This deviation from the expected behavior has long been attributed to spatial intermittency in the fine structure of the turbulent flow, as reviewed by Frisch [22], for example. Note that the spatial intermittency describes the distribution of dissipation in localized regions of intense dissipation, separated by relatively large regions where little dissipation occurs. In other words, the dissipation does not occur homogeneously in space, but is instead occurs in compact regions in space, separated by regions of little-to-no dissipation.

In response, Kolmogorov produced the refined similarity hypothesis [23, 24], which predicted that

$$\zeta_n = \frac{n}{3}[1 - \frac{1}{6}q(n-3)], \tag{3.7}$$

with the intermittency exponent, $q = 0.25 \pm 0.05$ [25].

This intermittency persists throughout the universal equilibrium range and, as a result, the use of a singular mean dissipation length-scale to describe the turbulent dynamics does not appear to be sufficient [26]. In this context, an alternative description of the dissipation scale that incorporates the existence of an entire continuum of local dissipation scales becomes attractive.

The longitudinal velocity structure function exponent, ζ_n, as a function of n from Kolmogorov [18] prediction, the prediction of the refined similarity hypothesis, and experiment measurements from the literature presented in Figure (3.1). This figure illustrates that ζ_n is not evenly distributed in space as Kolmogorov [18] assume. However, it is distributed nonlinearly in the space as the compiled measurements by Anselmet et al. [21] show that, which motivate looking for the spacial intermittency.

3.3   Probability Density Functions (PDFs) of Dissipative Scales

As indicated in the earlier section, the use of a singular mean dissipation length scale is not enough to define the turbulent dynamics. Therefore, a surrogate description of the dissipation scale is needed to combine the existence of an entire continuum of local dissipation scales. Yakhot [27] proposed an approach that connects and defines a local scale η using the velocity increment across that scale, $\delta_\eta u$, whereby

$$\eta|\delta_\eta u| \sim \nu, \tag{3.8}$$

and $\delta_\eta u$ is calculated from Equation (3.6) with $|r| = \eta$. This is analogous to the definition of a local Reynolds number based on the local scale η and the velocity increment $\delta_\eta u$, defining a dissipative scale as the one for which this Reynolds number
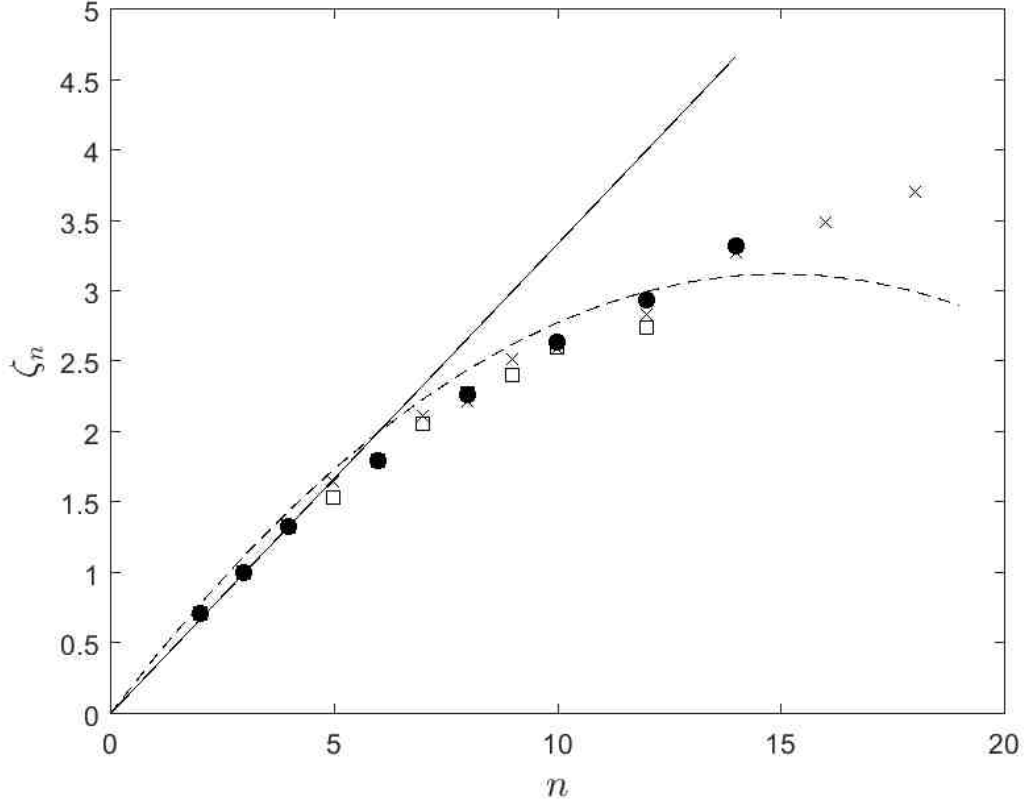
Figure 3.1: Variation of the longitudinal velocity structure function exponent, ζ_n, as a function of n. Solid line refers to the Kolmogorov [18] indication, $\zeta_n = n/3$. Dish line indicates the prediction of the refined similarity hypothesis, Equation (3.7) with $q = 0.25$. Symbols are measurements compiled by Anselmet et al. [21].

is $\mathcal{O}(1)$ [28]. Yakhot [27] suggested that this Reynolds number is connected to the crossover scales between the inertial subrange and the viscous dissipation range.

This is similar to what has been observed within the fashionable of multifractial formalism [28, 29, 30], where it has been shown that the crossover scale, a viscous dissipation scale, is related to Reynolds number through

$$\eta(h) \sim LRe_L^{-1/(1+h)}, \tag{3.9}$$

with h being the fractal dimension, having a spectrum of values. Re_L refers to the local large-scale Reynolds number that defines the large energy-producing eddies and

can be computed from

$$Re_L = \frac{\langle |\delta_L u| \rangle L}{\nu}, \tag{3.10}$$

in which $\delta_L u$ computed from Equation (3.6) at $|r| = L$. However, there are local scales smaller than η_K, which exist as an outcome of intermittency, leading to $h < 1/3$. Based on these foundations, an analytical expression for the probability density function of the dissipation scales was introduced by Biferale [31].

Yakhot and Sreenivasan [1, 2] introduced a surrogate approach to address the existence of a continuum of dissipation scales. They set η_{2n} to be an order dependent scale, which matches the separation distance between the inertial subrange and dissipative structure of $S_{2n}(|r|)$, this scale η_{2n} can be expressed as:

$$\eta_{2n} \sim (\langle [\partial_x u]^{2n} \rangle)^{1/(\zeta_{2n}-2n)} [(2n-1)!! \ \varepsilon^{2n/3} L^{(2n/3)-\zeta_n}]^{1/(2n-\zeta_{2n})}, \tag{3.11}$$

in which case the value of dissipating scale η depends on the order of the structure function being predicted. Utilizing the exact expressions for the nth-order longitudinal structure functions, Yakhot and Sreenivasan [1] showed that

$$\eta_{2n} \sim L Re_L^{-1/(\zeta_{2n}-\zeta_{2n+1}-1)}, \tag{3.12}$$

which leads to Kolmogorov's prediction when substituting $\zeta_n = n/3$.

To evaluate these concepts, as η is a random field, there is particular interest in characterizing this field through its PDF. To address this, Yakhot [27] presented an analytical description of the PDF of η. When normalized by η_0, this expression provided a good agreement with the PDFs estimated from the high-resolution direct numerical simulation (DNS) data of three-dimensional homogenous isotropic box turbulence of Schumacher [32]. The scale η_0 is analogous to η_K and is estimated from $\eta_0 \approx L Re_L^{-0.73}$. This can be compared to the results of scaling arguments, which suggest that $\eta_K \approx L Re_L^{-0.75}$, and thus the ratio η_0/η_K is close to unity, incrementing only gradually as $Re_L^{0.02}$, as detailed in the work of Hamlington et al. [33].

3.4 Scaling the Dissipative Scales

The analytical PDF of η/η_0, determined by Yakhot [27], was compared by Bailey et al. [34] to PDFs measured in low-Reynolds-number turbulent pipe flows at the pipe centerline and within the upper logarithmic layer and those calculated from homogeneous and isotropic DNS of Schumacher [32]. The comparison found good qualitative agreement between the experimental results and the analytical description and resulted in the collapse of the measured and simulated PDFs, fortifying the hypothesis that there is universality of the form of the PDFs and hence the distribution of η.

However, PDFs of η were also determined experimentally by Zhou and Xia [35], this time in buoyancy-driven turbulence. Instead of finding a good agreement between PDFs computed at different positions within the flow and at different Rayleigh numbers, the results exhibited a higher probability of there being scales smaller than η_0 than found by Schumacher [32] and Bailey et al. [34]. Zhou and Xia [35] attributed this discrepancy to a much higher level of small-scale intermittency caused by the presence of thermal plumes, which have a characteristic dimension in a thermal boundary layer that is smaller than η_K.

Hamlington et al. [33] also computed the PDFs of η/η_0 from very high-resolution DNS of turbulent channel flow and determined that universality of the PDF exists for much of the channel, except in the near-wall region. A similar position dependence of the PDF was identified experimentally in free-shear flow by Morshed et al. [36] who showed that this location dependency is related to large-scale shear through a mean shear-dissipation Reynolds number. In both studies, the comparison of PDFs calculated within regions of reduced shear to those observed in homogenous and nearly homogeneous turbulence by Schumacher [32] and Bailey et al. [34] showed a good agreement. Hence the presence of mean velocity shear appears to negatively influence the scaling of the PDFs.

Recently, Bailey and Witte [37] experimentally determined the PDFs of η in a

turbulent channel flow. They found that when η_0 is used as a normalization parameter, the distributions of PDFs are in a good agreement with those previously reported experimentally, numerically and analytically. However, using η_0 as a scaling parameter in the near-wall region lead to a non-universality of small scales in this region, coinciding with the presence of increased mean shear. Bailey and Witte found that the lack of universality could be attributed to the imperfect description of large scales, L, when using the measured integral length-scale. This influences the scaling parameter η_0 and results in the small scales being poorly described by η_0. Thus, they defined an alternate scaling parameter, η^*, which depends on a mixing length-scale and its corresponding Reynolds number, with the mixing length-scale related to the distance from the wall. Using η^* instead of η_0, Bailey and Witte found there to be an improved collapse of the PDFs near the wall. However, this collapse degraded for $y/\delta > 0.5$, which suggested there exists scaling behavior analogous to the inner- and outer-scaling that describes the mean flow.

In summary, these recent results imply that the mean shear impacts the description of the local dissipation scales. However, this impact appears to be through the scaling parameter chosen, rather than through the distribution of the PDF itself. In regions of small mean shear such as in homogenous isotropic turbulence, in the centerline of channel and pipe flows and the center of the Rayleigh-Beŕnard convection cells, the appropriate scaling parameter appears to be η_0, which is analogous to the Kolmogorov scale. In the high-shear regions of turbulent channel flow, this scale appears to be proportional to the distance from the wall. Thus, it is not yet clear whether the scaling of the PDFs within wall-bounded flows suggested by Bailey and Witte [37] can extend to external wall-bounded flows with both laminar and turbulent free-stream. it is also not yet clear whether introducing a scaling parameter depending on an alternative length-scale in external wall-bounded flows will support the universal distribution of the PDFs.

Table 3.1: Turbulence detection functions.

Reference	Detector function
Townsend [41]	$\|u_1\|, \;\; \|\partial u_1/\partial t\|$
Corrsin and Kistler [38]	$\|u_1\|, \;\; \|\partial u_1/\partial t\|$
Heskestad [42]	u_1^2
Gartshore [43]	$\|\partial u_1/\partial t\|$
Fiedler and Head [44]	$\|\partial u_1/\partial t\|$
Kaplan and Laufer [45]	$(\partial u_1/\partial t - \langle \partial u_1/\partial t \rangle)^2$
Wygnanski and Fiedler [46]	$(\partial u_1/\partial t)^2 - (\partial^2 u_1/\partial t^2)^2$
Kovasznay et al. [47]	$\|\partial^2 u_1/\partial y\,\partial t\|$
Antonia and Bradshaw [48]	$(\partial u_1/\partial t)^2$
Sunyach [49]	$(\partial u_1/\partial t)^2$ filtered
Antonia [50]	$(\partial u_1 u_2/\partial t)^2$
Thomas [51]	$\|\partial u_1/\partial t\|$ filtered
Chauhan et al. [40]	$(1 - \langle U_1 \rangle/U_\infty)^2$
Alhamdi and Bailey [52]	$100 \times (1 - \langle U_1 \rangle/U_\infty)^2$

3.5 Detection of External Intermittency

The existence of the leading and trailing edges of turbulent bulges in the outer part of the turbulent boundary layer was first identified and studied by Corrsin and Kistler [38] using hot-wire signals. They observed that sharp changes occur during the transition from turbulent to non-turbulent motions and referred to them as 'backs,' while their counterpart 'fronts' separate non-turbulent fluids from contiguous-turbulent fluids.

Detection of intermittency from a velocity time-series, as done by Corrsin and Kistler [38], requires the application of a kinematic criterion. To identify periods of interfaces in a velocity signal, the time derivative of the velocity component [39], the derivative of the instantaneous shear stress, and the magnitude of the velocity have all been utilized to construct different detection functions (see Table 3.1 for a list of different turbulence detector functions). In this study, we used a kinetic energy criterion suggested by Chauhan et al. [40] to detect turbulent/non-turbulent interfaces.

Chapter 4 Experiment Description
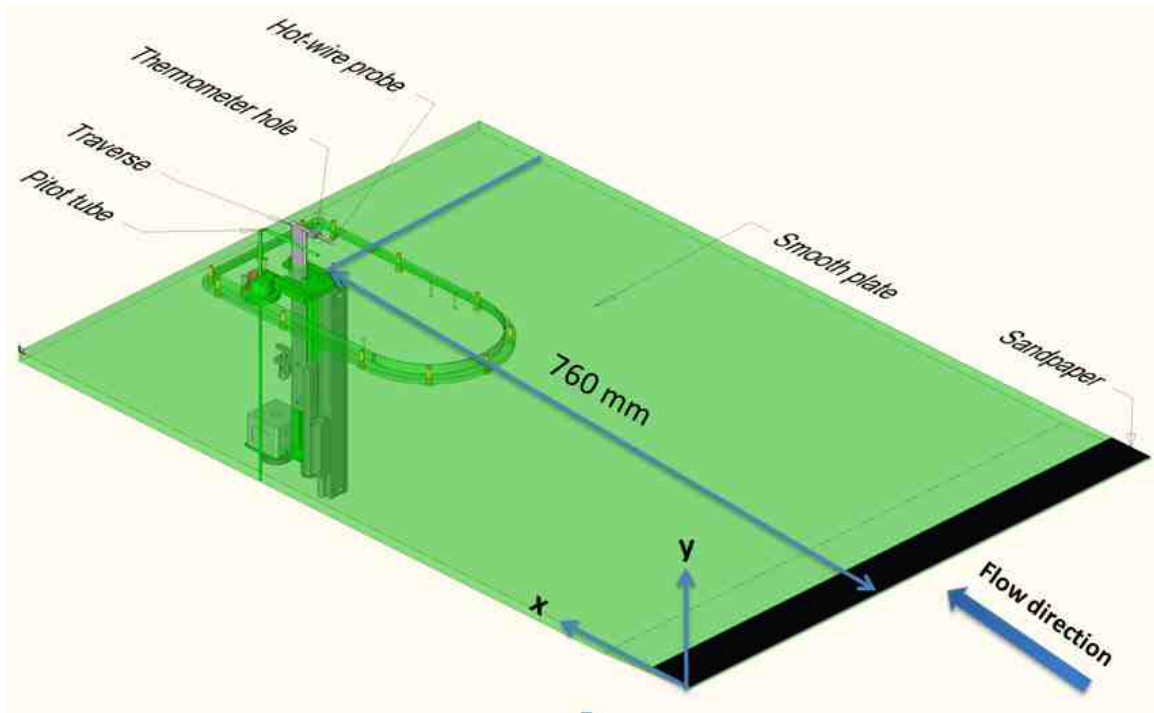
Figure 4.1: Experiment setup.

4.1 Overview

All measurements in this study were conducted in a wind tunnel flow facility located in the Experimental Fluid Dynamics Laboratory at the University of Kentucky. The experimental setup, consisting of a flat plate equipped at the leading edge by sandpaper trip, hot-wire probe, traverse, Pitot tube and resistance temperature detection (RTD) thermometer, is presented in Figure (4.1). The coordinate system used here is arranged with $x = x_1$ aligned in the flow direction, and $y = x_2$ aligned in the wall-normal direction. The hot-wire probe was used to measure the streamwise velocity, $U_1(t)$, over a range of wall-normal locations. A custom-built lead-screw system was

used to traverse the hot-wire probe normal to the plate surface. The Pitot tube and RTD were used to calibrate the hot-wire probe by measuring the reference velocity and temperature. During the measurement, the free-stream temperature was also monitored using a separate type K thermocouple operated in a handheld multimeter. The sandpaper trip was used to trigger transition to turbulence at the leading edge of the plate and ensure that turbulent conditions existed at the measurement location. More details of these elements of the experiment are presented in the following sections.

4.2   Flow Generation

4.2.1   Wind Tunnel

The wind tunnel used is an open circuit wind tunnel manufactured by Engineering Laboratory Design as the model 406(B). This facility has a test section with a $0.61\ m\ \times\ 0.61\ m$ cross-sectional area and length of $1.2\ m$, and is driven by a $40\ Hp$ ($29.83\ kW$) motor that can achieve free-stream velocity, U_∞, up to $45.7\ m/s$. For these experiments the free-stream velocity was approximately $4\ m/s$.

4.2.2   Flate Plate

To generate a turbulent boundary layer, a smooth-flat plate with dimensions of $886\ mm\ \times\ 608\ mm$ was placed in the test section. To trip the boundary layer forming on the plate, it was equipped at the leading edge by 50.8 mm of a 60 grit sandpaper trip. A trailing edge flap was also located on the plate to prevent leading edge flow separation. To produce the free-stream turbulence, a grid with a solidity of 0.32 and square perforations having mesh sizes of $M = 25.4$ mm could be inserted in the inlet of the test section. The resulting free-stream turbulence intensity at the measurement location was approximately 2.5%. To measure the properties of the boundary layer developing along the smooth plate when mounted in the wind tunnel,

measurements of streamwise velocity, U_1, were performed over a range of wall-normal distances, using a hot-wire probe. More details of the hot-wire probe are given in Section (4.3.1)

4.3   Measurement Instrumentation

4.3.1   Hot-wire Probe

The hot-wire probe was made from platinum-core Wollaston wire etched to a sensing length of $\ell = 0.50$ mm and diameter of 2.5 $\mu\, m$. This leads to $\ell^+ = \ell u_\tau / \nu \approx 6$. The maximum of the ratio ℓ/η_K was approximately 3 and occurred in the measurement locations closest to the wall. The probe was operated in a constant temperature anemometer (IFA 300) system at an overheat ratio of 1.6. Frequency response of the probe was measured via square wave test to be 75 kHz. The constant temperature anemometer signal was low-pass filtered at half the sample frequency, f_s, which was 100 kHz for the case without free-stream turbulence and 200 kHz for the case with free-stream turbulence.

The probe was located 760 mm from the leading edge of the smooth plate and traversed in the wall-normal direction, i.e. in the y-direction, from its initial position approximately 100 ± 5 μm from the wall to its final position 120 mm from the wall. Streamwise velocity was measured at 40 points logarithmically spaced between these two locations. At each measurement location for the baseline case the data were sampled for 60 s. For the case with free-stream turbulence, the sample time was increased to 120 s. The free-stream temperature was measured by a type K thermocouple and found to remain approximately constant for each measurement, changing by less than 0.4°C over the course of a profile measurement.

4.3.2 Traverse

To traverse the hot-wire probe normal to the plate surface in the wind tunnel a nano-stepping traverse equipped with a high-accuracy linear encoder and controlled by stepper motor was employed (0.5 μm resolution and ± 3 μm accuracy). An electrical contact switch was used to set the initial position of the hot-wire probe from the wall. At the initial measurement location, the distance from the wall to the probe was found using a distance measuring microscope (Titan Tool Supply 2DM-1 with ± 15 μm accuracy). Probe positioning and data acquisition was controlled by a custom LabVIEW program.

4.4 Calibration

Hot-wire probe calibrations were performed in the free-stream directly prior to, and following, each measurement run using a Pitot-static tube located in the free stream at the measurement location. The pre-measurement and post-measurement calibrations were used to verify that there was no voltage drift during a profile measurement. To maximize the sensitivity over the range of calibration velocities, two transducers with accuracy of 0.25%, having sensitivities of 125 and 1245 Pa, were used to measure the pressure difference between total and static pressure. The calibration data were fitted with a fourth-order polynomial to convert the measured time dependent voltage into time series of streamwise velocity, $U_1(t)$. Figures (4.2 & 4.3) show sample calibration data from two cases and compares the hot-wire reading to the velocity measured by the Pitot tube pre- and post- experiment, as well as the resulting curve fit, respectively. These figures show a good agreement between pre- and post-measurement calibrations. Calibrations measured for replicated cases are provided in Appendix (8.2).

4.5 Measurement Uncertainty

This section is a concise of explanations and estimation methods of measurement uncertainty that is raised from measurement errors. The measured value of a property is an estimate of the true value gave by the instrument. In general, this value is unsimilar to the true value as no measuring system is perfect. The difference between these two values is represented by the absolute measurement error. The relative measurement error defines as the percentage ratio of the absolute measurement error and the true value. Both the true value and the measurement error cannot be found exactly.

Accuracy and inaccuracy of a measurement is an indication of how perfect or imperfect the measurement is, respectively. This means they refer to how the measure value close to the true value, when they are compared. Inaccuracy in a measurement could be raised from errors in calibration, data reduction and data acquisition. Furthermore, these errors are caused by the imperfections of the instruments and procedures. In addition to these errors, human errors are other possible errors in measurements. These errors raise from the inconsistent and imprecise readings of analogue measuring systems or imprecise eye averaging of the fluctuating digital meters [53]. In the next two subsection, more details on the two kinds of the measurement errors, bias (fixed or systematic) errors and precision (random) errors, that caused measurement uncertainty will be provided.

4.5.1 Bias Errors

The bias errors are not changing during the experiment and could rise positive or negative effects on the measurements. The bias errors are unknown and attributed to the overall uncertainty of the measurements in most cases. However, if these errors can be determined by comparison to a more accurate instrument or a standard and estimated to be affecting the measurements, they should be removed from the

measured value.

In the experiments of this study, the hot-wire probe calibrated by reference to a Pitot tube. In the near-wall region, the hot-wire measurements can be effected by free convection, heat conduction to the walls, atmosphere temperature changes, the difficulty of finding the critical distances from the wall, and calibration drift [54]. Thus, these errors could lead to drift in the measurements. For example, the difficulty of find the initial probe position from the wall caused by two classifications of errors: human error that cased by eye averaging, and the errors raised from imperfection of the distance measuring microscope. Another example of the bias error in these experiments is the drift calibration that caused by referencing the hot-wire probe to the Pitot tube. These small errors can be shown in Figures (4.2 & 4.3).

4.5.2 Precision Errors

Precision errors are, presumably, changeable throughout the experiment in several undesirable inputs. Each of these inputs can be assumed to cause a relatively small influence on the output; therefore, the total effect is unpredictable. The occurrence of this leads the experiment to be under statistical control, where the central limit theorem indictates that repeat measurements should have a Gaussian (normal) distribution. Thus, a normality test may be performed to prove randomness. Then, identifying possible outliers and removing them from the sample are recommended [53]. A statistical measured of the possible value of the precision error is the standard deviation that shows the spread of the distribution of repeat values about the mean.

The magnitudes of both the bias and precision errors specify the accuracy of a measurement. If both these errors are small, the reading is consider to be accurate otherwise it is termed inaccurate. There are three types of inaccurate measurements: biased and precise, unbiased and imprecise, and biased and imprecise.

Repeatability of a measurement is the replicate of the readings of the same prop-

erty with the same instrument and during a relatively short period of time under the same conditions. It is not necessary that the good repeatability means negligible random errors even though good replication is a good indication of the closeness of the readings. In addition, good repeatability does not refer necessarily to overall accuracy as it may not subtracted the bias. Replication of a measurement is to develop statistics and ensure repeatability for this measurement as shown in the most Figures in Chapter (5).

To compare data in different laboratories and measured with different instruments, the closeness of the repeated readings is an indication of which is called Reproducibility. Good reproducibility of a measurement indicates that both the random and systematic errors are small.

4.6   Flow Conditions

The turbulent boundary layer at the measurement location has Reynolds number, $Re_\tau = \delta u_\tau/\nu \approx 1000$ ($Re_\theta = \theta U_\infty/\nu \approx 2000$). Here, the boundary layer thickness, δ, is calculated at the streamwise mean velocity, $\langle U_1 \rangle = 0.99 U_\infty$. The friction velocity, u_τ, was calculated using two approaches (the Clauser-plot [55] approach and the approach of fitting near-wall data to DNS data) that will be presented in details in the next chapter. The values of u_τ determined from both approaches were found to be in agreement. Thus, the approach of finding the value of u_τ, which best scaled the measured velocity profiles in the near wall region to the DNS data of Schlatter and Örlü [56], was considered for further calculations. The experimental conditions for each case are presented in Table (4.1).

Table 4.1: Experimental conditions and symbols used to represent each case in following figures.

Free Stream	Laminar	Turbulent
Re_τ	1000	1000
Re_θ	1800	2100
u_τ (m/s)	0.19	0.18
ν/u_τ (μm)	79	83
δ (mm)	82	85
Symbol	△	□
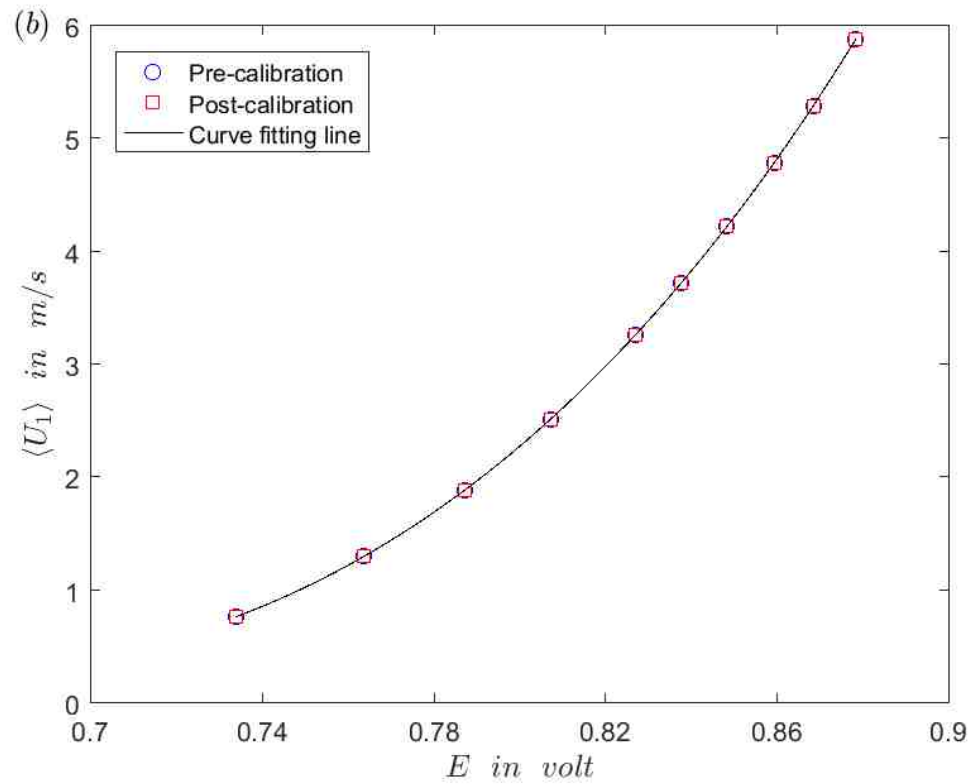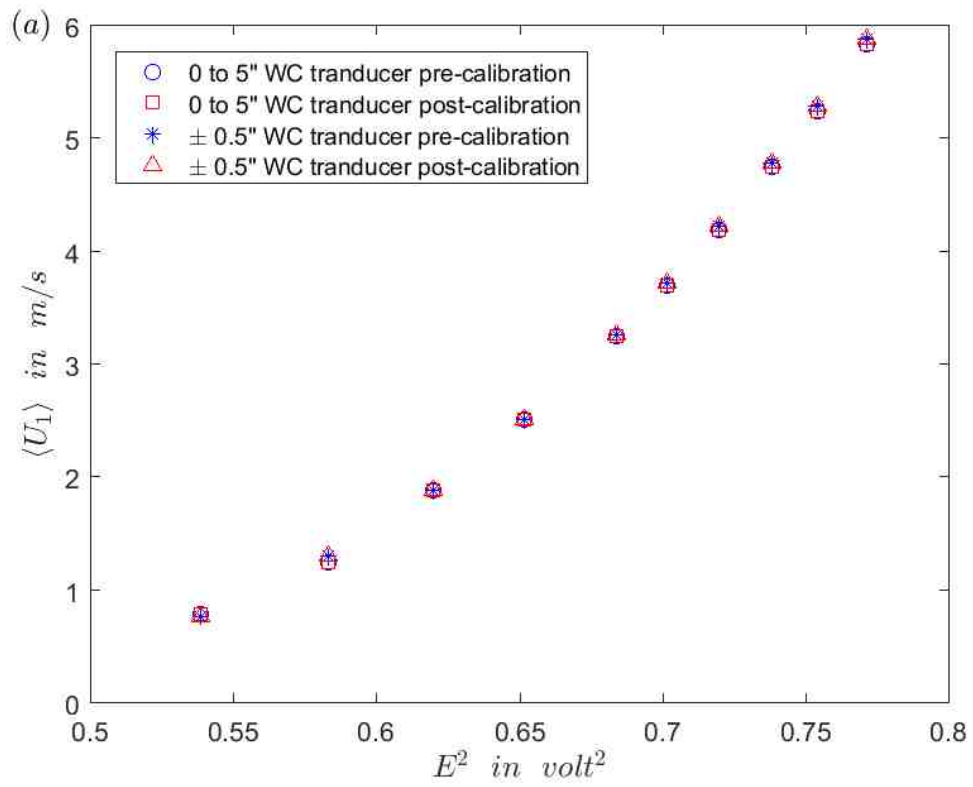
Figure 4.2: Calibration of the hot-wire reading for the case with a laminar free-stream condition using a Pitot tube (a) before; and (b) after curve fitting.
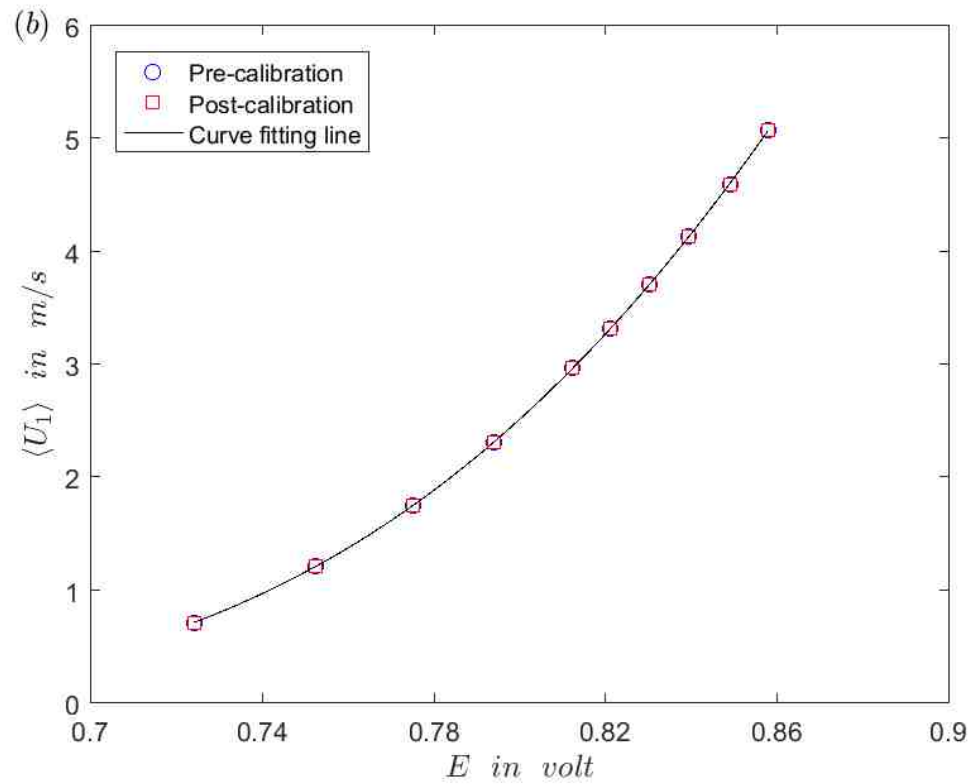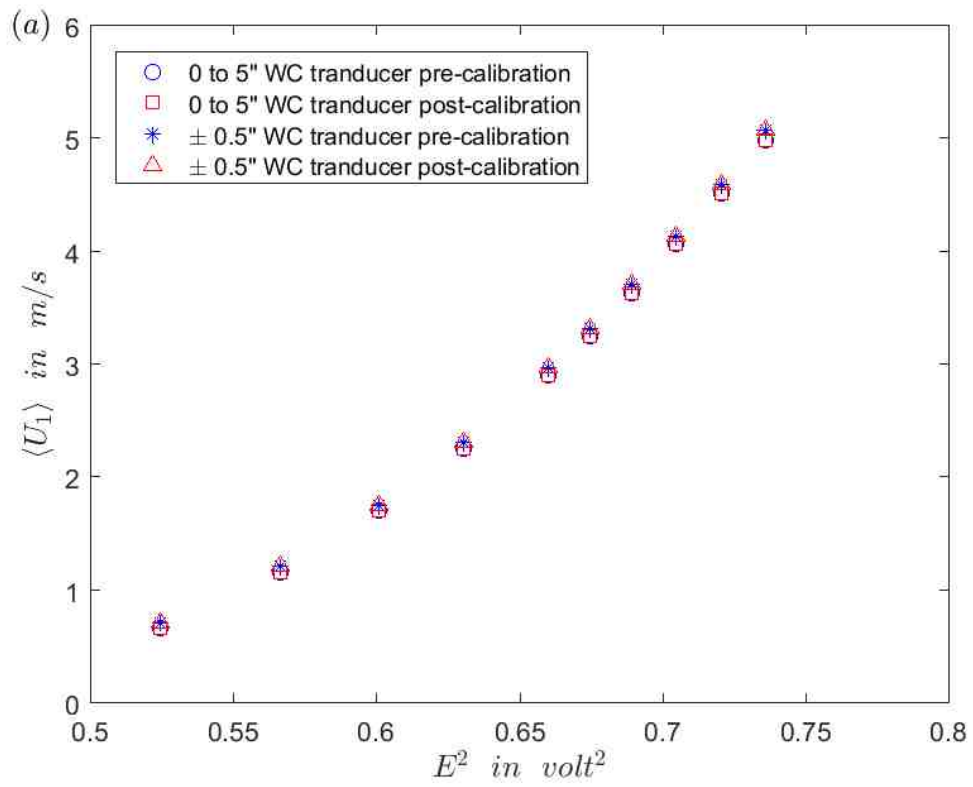
Figure 4.3: Calibration of the hot-wire reading for the case with a turbulent free-stream condition using a Pitot tube (a) before; and (b) after curve fitting.

Chapter 5 Mean Flow Analysis

This chapter will first describe the two approaches that were used to estimate the friction velocity, u_τ, in the two flow conditions and their replications. Then, the profiles of the mean steamwise velocity and variance profiles for both conditions will be presented. Finally, the distributions of the Reynolds stresses will be discussed.

5.1   Determination of Friction Velocity

Friction velocity, u_τ, is used to characterize shear-related motion in moving fluids and is used in turbulent flows as a characteristic scaling parameter for velocity. One way to define the friction velocity is through the non-dimensionalization of the turbulent equations of motion. For instance, in a fully developed turbulent boundary flow, the streamwise momentum equation in the very near wall layer reduces to $u_\tau = \sqrt{\frac{\tau_w}{\rho}}$, as introduced in Equation (2.30).

Despite the importance of u_τ for scaling the boundary layer, determination of τ_w is a non-trivial process. In this study we used two related indirect approaches to determine u_τ : the so-called Clauser-plot [55] approach and fitting near-wall data to DNS data. Both approaches require that the turbulent boundary layer scaling discussed in Section (2.3) is valid for this experiment.

In the Clauser-plot approach, the inner scaled velocity profile is assumed to match the log-law. This approach is based on the assumption that the velocity profile follows a universal logarithmic form in the overlap layer between the inner and outer regions of the turbulent boundary layer. In this method, the data was fitted to the log-law

The Clauser-plot approach is simply to adjust u_τ to find the best fit of the measured data to Equation (2.40). This approach is highly dependent on the choice of the

Figure 5.1: Profiles of mean streamwise velocity normalized by u_τ across the boundary layer for the laminar free-stream condition with three replicates.

von Kaŕmań constant, κ, and the constant B. Here we used $\kappa = 0.384$ and $B = 4.173$ [57]. In other words, the mean streamwise velocity profile of our data is fitted to the log-law in the region between the inner and outer layer in the boundary layer. Then, we find u_τ that best matches log-law to our data in the overlap region.

The mean streamwise velocity profiles, normalized by u_τ across the boundary layer, for the laminar free-stream condition with three replicates of the measurement, and compared to the log-law are shown in Figure (5.1). Ensuring repeatability of our data, the four mean streamwise velocity profiles show a qualitative agreement in the overlap layer between the inner and outer regions of the boundary layer.

This approach also is used to estimate u_τ for the normalized mean streamwise

Figure 5.2: Profiles of mean streamwise velocity normalized by u_τ across the boundary layer for the turbulent free-stream condition with two replicates.

velocity data for the turbulent free-stream condition, with the experiment replicated twice. Comparison to the log-law for these measurements is presented in Figure (5.2). As in the laminar free-stream condition, the velocity scaled with the estimated u_τ fits the log-law in the log layer of the boundary layer. Again, in this condition, the mean streamwise velocity profile and the log-law are in a agreement in the overlap layer.

Thus, using this approach, u_τ was found to be 0.19 m/s for the condition of laminar free-stream and 0.18 m/s for the condition of turbulent free-stream as presented in Table (4.1). This approach provides us a coarse estimate of the friction velocity. Therefore, we will match our data to DNS data to calculate u_τ that best matches our data with these DNS data in order to validate the first approach that we used to

determine u_τ.

In the second approach used to find friction velocity, we find u_τ by finding the value that best matches the measured profile of the normalized mean streamwise velocity profile to DNS data in the near-wall region. In this method, the mean streamwise velocity profile in the wall-normal distance will match the DNS data at approximately the same Reynolds number.

The mean-flow data are presented in the wall-normal distance form in Figures (5.3 & 5.4) for both laminar and turbulent free-stream conditions, respectively, with DNS results from simulations that were performed at the Royal Institute of Technology (KTH), Stockholm at $Re_\theta = $ 2000 [56]. The friction velocity, u_τ, was calculated in both conditions by finding the value of u_τ, which best scaled the measured mean streamwise velocity profile to this DNS data of Schlatter and Örlü [56]. A good agreement between our data and the DNS data is observed. u_τ estimated using this way matches the values of u_τ found from the Clauser-plot approach for both free-stream conditions.

Both methods, Clauser-plot and matching scaled profile to DNS data, were used to estimate u_τ, and both were determined to be in agreement. For the remainder of this work, the values calculated using matching scaled profile to DNS data are the ones considered.

5.2 Streamwise Velocity and Variance Profiles

Figures (5.3 & 5.4) show the wall-normal dependence of the inner-scaled profiles of the mean streamwise velocities for both laminar and turbulent free-stream conditions. In these figures, a comparison between our data and DNS of Schlatter and Örlü [56] displays small discrepancies between our data and the DNS data, particularly in the near-wall region and the free-stream region (potential layer). These discrepancies are consistent with the existent of non-zero pressure gradient free-stream conditions
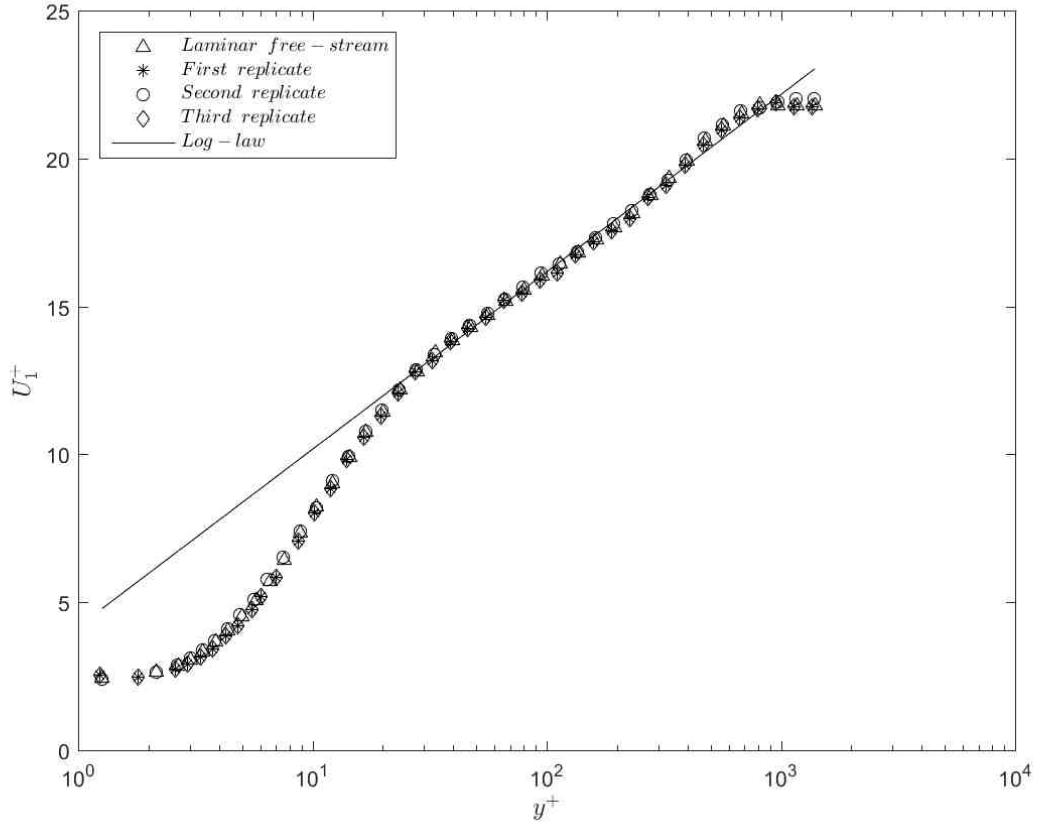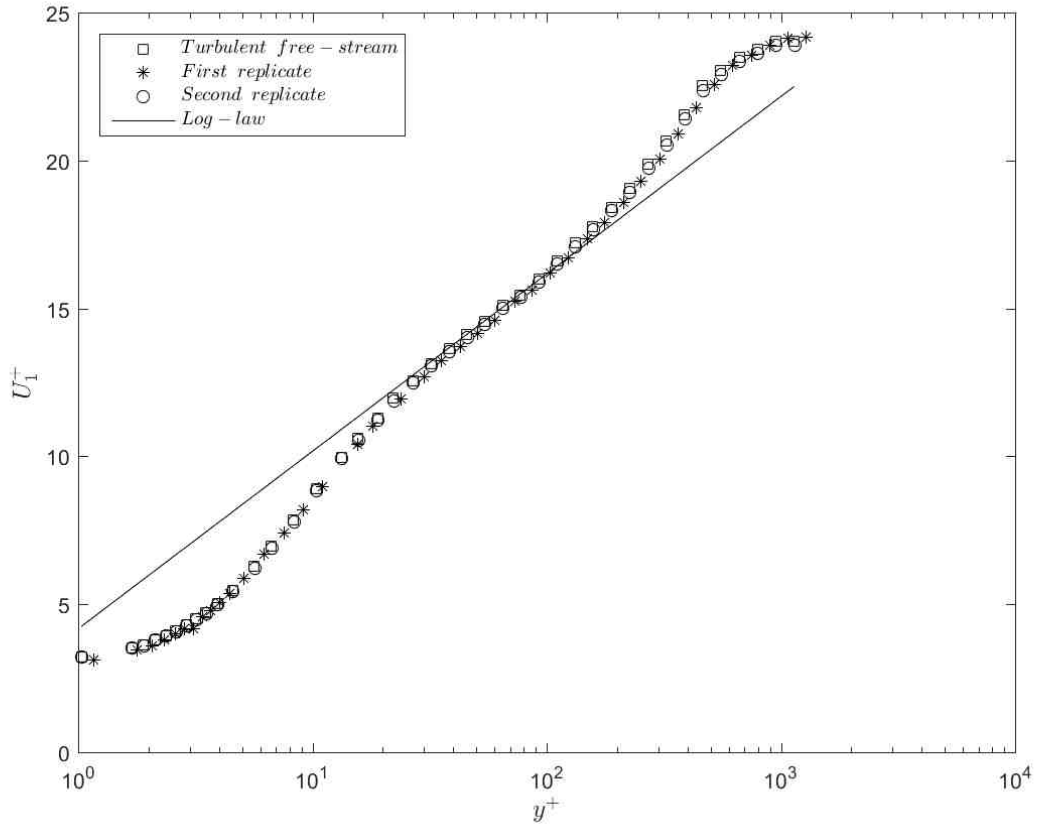
Figure 5.3: Profiles of mean streamwise velocity normalized by u_τ across the boundary layer for the laminar free-stream condition with three replicates.

in the experiment, possibly introduced by the flap at the back of the plate used to prevent flow separation at its leading edge. The enhancement of the wake layer for the case with free-stream turbulence is expected, and consistent with prior studies comparing laminar to free-stream conditions. Furthermore, in the near-wall region, the discrepancy between the experiments and DNS can be attributed to the bias in the measurements that can be created by heat conduction to the wall and the formation free convection as the hot-wire probe enters into the low velocity environment near the surface.

The mean-flow data is presented in the wall-normal distance form in Figure (5.5) for both flow conditions with the DNS data at $Re_\theta = 2000$ [56]. The inner-scaled profiles of the mean streamwise velocity and the streamwise turbulence intensity with

Figure 5.4: Profiles of mean streamwise velocity normalized by u_τ across the boundary layer for the turbulent free-stream condition with three replicates.

the inner-scaled distance from the wall are shown in Figures (5.5 (a & b)), respectively. These two figures show a good agreement between our data for the case without free-stream turbulence condition and the DNS data. As indicated earlier, this comparison demonstrates small differences in the free-stream due to the difference in the values of Reynolds numbers among these cases. For the case with free-stream turbulence, as expected, the inner-scaled turbulence intensity distribution is higher than that of the case without free-stream turbulence as shown in Figure (5.5 (b)). This is attributed to the higher level of turbulence in this case, where the turbulence intensity is 2.5% at the measurement location. Note that in Figures (5.5 (a & b)) data when $y^+ \leq 5$ [58] was removed due to the near-wall bias in the data that attributed to the known hot-wire issues when measuring near a solid surface.
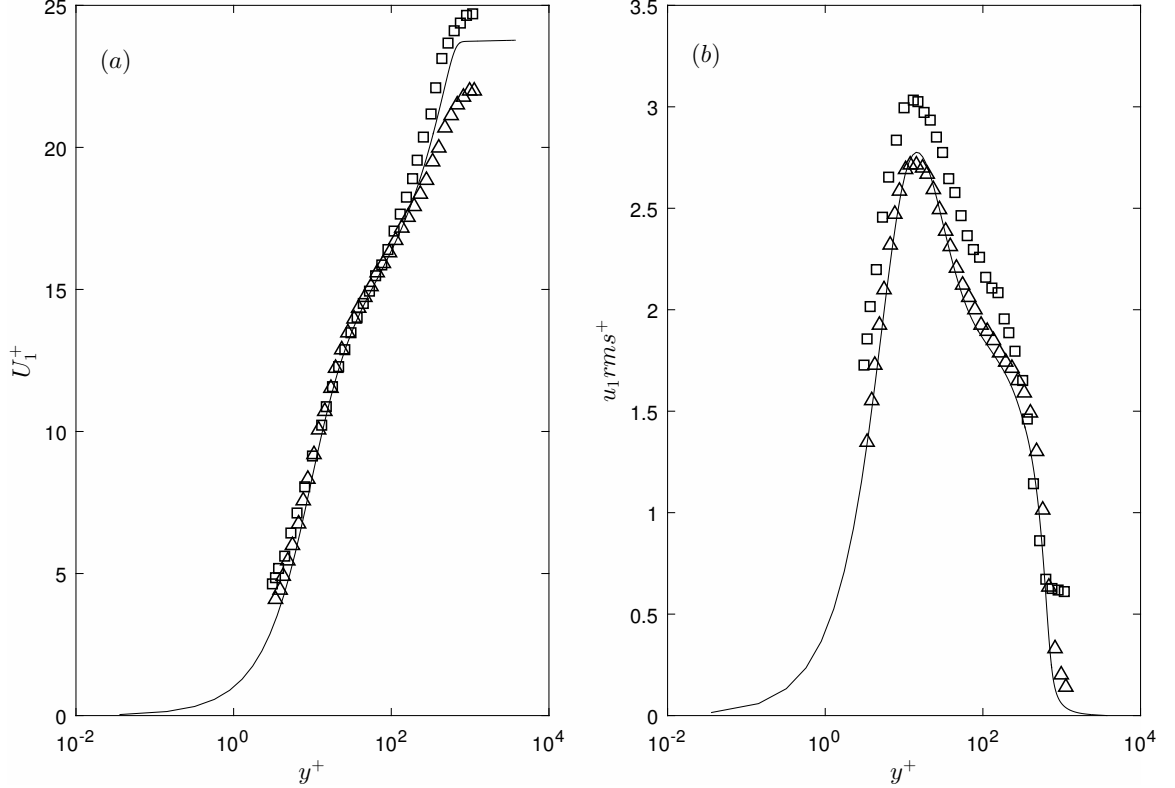
Figure 5.5: (a) Inner-scaled mean streamwise velocity profile. (b) Inner-scaled streamwise turbulence intensity profile. Symbols are as in Table (4.1), with line indicates DNS data of Schlatter and Örlü [56].

Turbulence intensity refers to the turbulence level. The inner-scaled streamwise turbulence intensity, $u_1 rms^+$, can be determined from

$$u_1 rms^+ = \frac{u'}{u_\tau}, \tag{5.1}$$

in which u' is the root-mean-square of the turbulence velocity fluctuation in the streamwise direction, which can be computed from $u' = \sqrt{\langle u_1^2 \rangle}$. The wall-normal dependence of the inner-scaled streamwise turbulence intensity profile for both conditions is presented in Figure (5.5 (b)). This figure demonstrates the higher level of the turbulence intensity for the turbulence free-stream condition compared to the laminar free-stream condition throughout the wall-normal locations. Furthermore, the peaks of the turbulence intensity for both conditions agrees with the previously reported experimental and numerical data [59, 56]. The difference in the turbulence
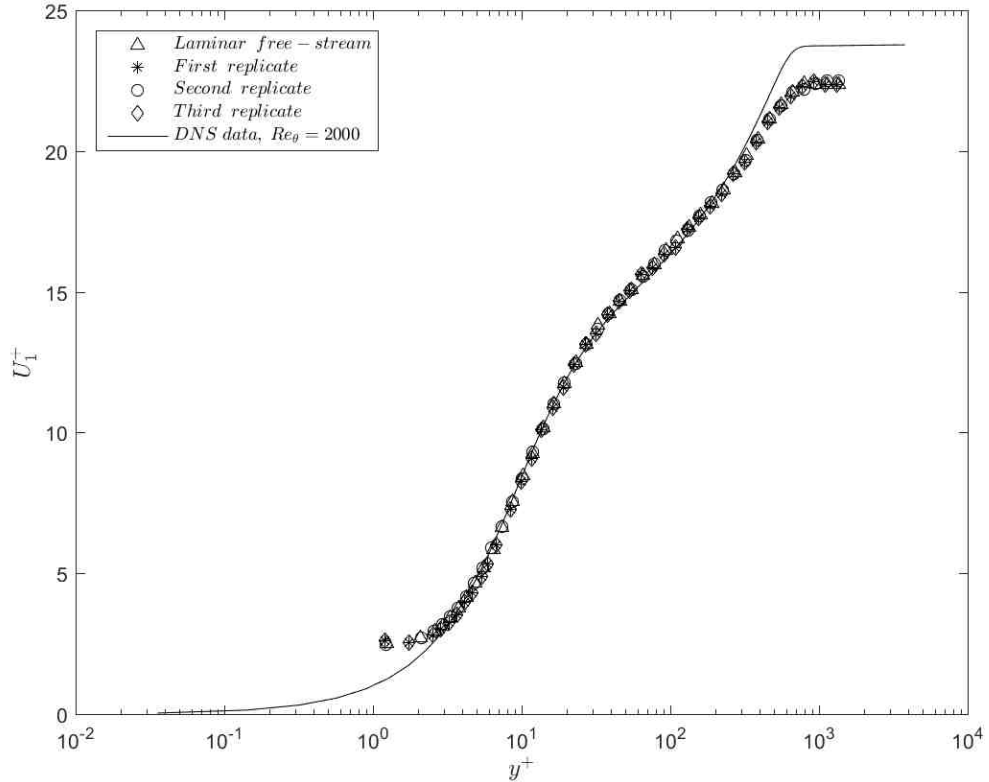
45
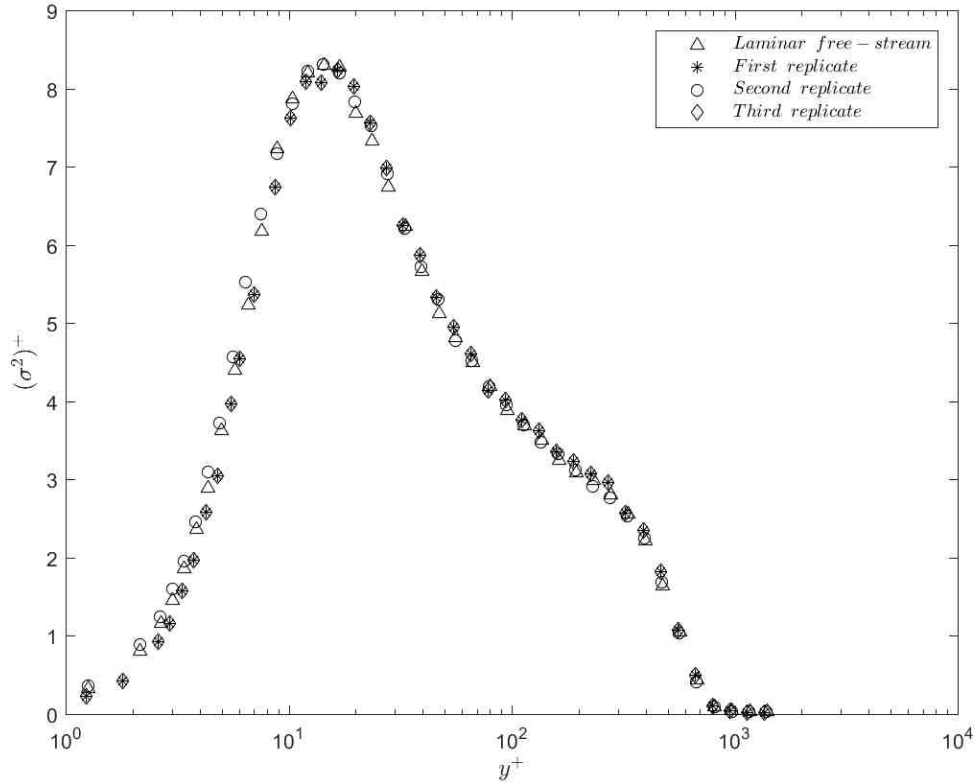
Figure 5.6: Profiles of variances of the streamwise velocity normalized by u_τ across the boundary layer for the laminar free-stream condition with three replicates.

intensity between the two free-stream conditions can be observed in the edge of the boundary layer, near $y^+ \approx 1000$.

To demonstrate the repeatability of the fluctuation measurements, the wall-normal dependence of the inner scaled distribution of variance, $(\sigma^2)^+$, is shown in Figures (5.6 & 5.7) for all repeated measurements made in the laminar and turbulent free-stream, respectively. In both conditions, these figures show clearly the repeatability of the data. In both free-stream conditions, the peaks of the variance is near to $y^+ = 15$.
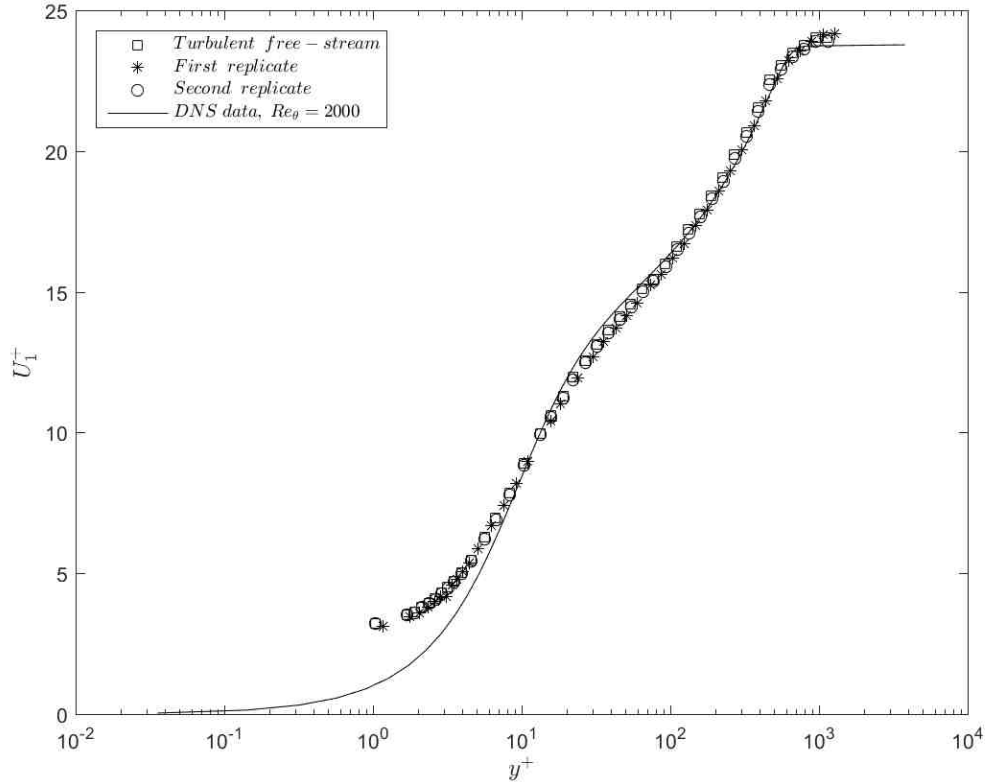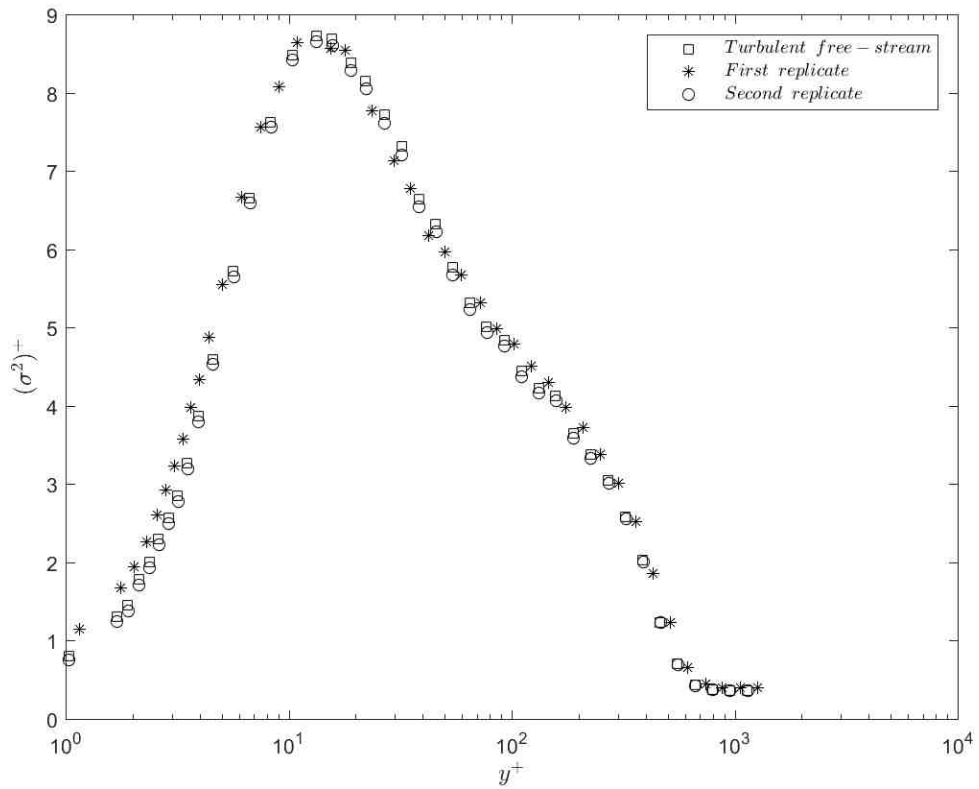
Figure 5.7: Profiles of variances of the streamwise velocity normalized by u_τ across the boundary layer for the turbulent free-stream condition with two replicates.

Chapter 6 Universality of Local Dissipation Scales

6.1 Longitudinal Energy and Dissipation Spectra

To describe the turbulence, examples of the estimated energy and dissipation spectra as well as the measured statistics are first presented. The wavenumber spectra of the streamwise velocity $E_{11}(k_1)$ was estimated through

$$E_{11}(k_1) = \frac{\langle U_1 \rangle}{2\pi} F_{11} \left(\frac{2\pi}{\langle U_1 \rangle} f \right), \tag{6.1}$$

in which $F_{11}(f)$ is the frequency, f, spectrum of the streamwise velocity calculated from the magnitude of the Fourier transformation of the streamwise velocity fluctuations $u_1 = U_1(t) - \langle U_1 \rangle$. In order to interpret temporal information into spatial information in the calculation, Taylor's frozen flow hypothesis [60] was used, where the streamwise wavenumber, k_1, was found from frequency through $2\pi f / \langle U_1 \rangle$. There is much literature on the validity of Taylor's hypothesis [61, 62, 63], which suggest possible additional corrections are required when translating the temporal domain into the spatial domain. Such corrections are not attempted here since the focus of the study is the smallest turbulent scales, where Taylor's hypothesis provides a reasonable approximation of the spatial separation. Note also that these corrections are not without problems, especially for the low Reynolds numbers of the present study, where they could lead to bias of the data prior to the analysis [64, 65, 66].

In order to estimate η_K, an estimate of $\langle \varepsilon \rangle$ must first be found. One approach to calculate $\langle \varepsilon \rangle$ is from the integration of the approximated one-dimensional dissipation spectrum $D(k_1)$ after assuming local isotropy [67] following

$$\langle \varepsilon \rangle \approx 15\nu \int_0^{k_c} D(k_1) dk_1 \approx 15\nu \int_0^{k_c} k_1^2 E_{11}(k_1) dk_1, \tag{6.2}$$

where $D(k_1)$ was approximated from the longitudinal energy spectrum through $D(k_1) = 15\nu k_1^2 E_{11}(k_1)$. To minimize the effect of the f^2 noise of the thermal anemometer and prevent contamination of the $\langle \varepsilon \rangle$ estimate by the oversampling of the velocity signals in the present measurements, an appropriate cutoff wavenumber, k_c was applied as an upper bound of the integration. This cutoff was set at the wavenumber when an inflection started to appear in the frequency spectrum, i.e. the frequency at which the noise started to overcome the useful signal.

In this work, the streamwise component of the velocity was resolved utilizing a single-sensor thermal anemometry probe, which was not capable of conducting measurements of the all components of the time-series of the local rate-of-deformation tensor. Hence, an alternate estimate of the dissipation rate could be obtained using the one-dimensional approximation [68]

$$\varepsilon(t) \approx 15\nu \left(\frac{\partial u_1}{\partial x_1} \right)^2, \tag{6.3}$$

which assumes local homogeneity. However, as reported in Pope [8], for example, such alternatives are only estimated to be qualitatively similar to the instantaneous dissipation. To evaluate Equation (6.3), Taylor's hypothesis and a first-order finite difference were used as follows

$$\varepsilon(t) \approx 15\nu \frac{1}{\langle U_1 \rangle^2} \left[\frac{u_1(t + \Delta t) - u_1(t)}{\Delta t} \right]^2, \tag{6.4}$$

here $\Delta t = 1/f_s$. In the present measurements, to minimize contamination from instrumentation noise, the data were filtered using an additional zero-phase, eight order digital Butter-worth filter. The cutoff frequency was chosen to be $k_c \langle U_1 \rangle / 2\pi$. Both Equation (6.2) and the mean of Equation (6.4) were used to estimate $\langle \varepsilon \rangle$, and both were determined to be in agreement. For the remainder of this work, the values calculated using Equation (6.4) are the ones presented. Note that the assumptions of local homogeneity and isotropy used to extract surrogates for the three-dimensional dissipation from one-dimensional measurements break down near the wall. Hence,
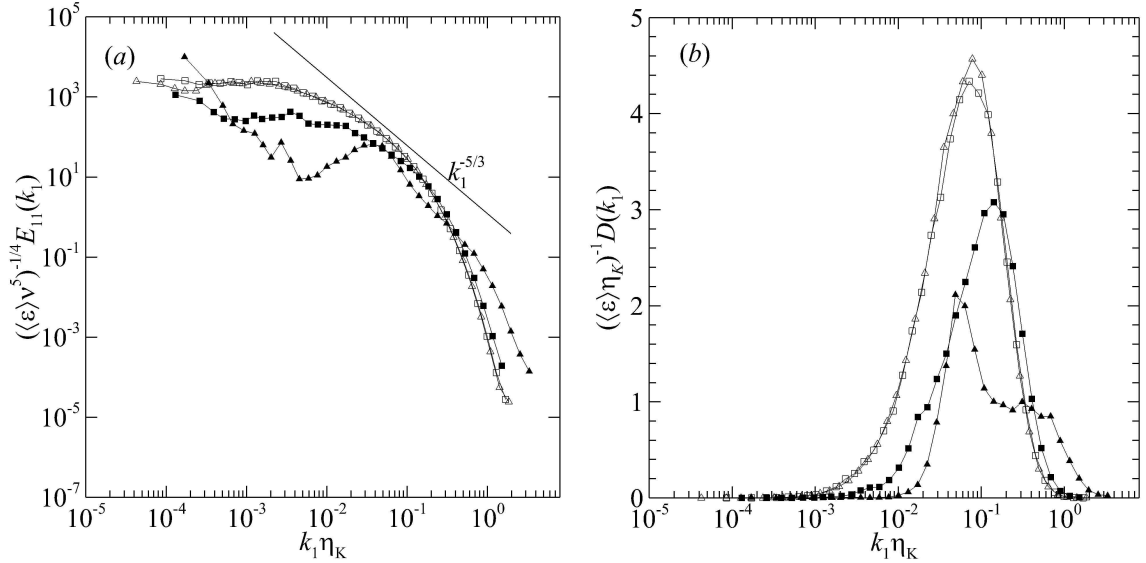
Figure 6.1: (a) Normalized longitudinal one-dimensional energy spectra measured at $y^+ \approx 30$ (hollow symbols) and 800 (filled symbols). (b) Corresponding estimate of the dissipation spectra. Symbols are as in Table (4.1).

only measurement points for which $y^+ = yu_\tau/\nu > 25$, where such scaling is observed, are included in the present study.

The measured longitudinal one-dimensional energy spectra and the corresponding approximated one-dimensional dissipation spectra for both cases with laminar and turbulent free-stream conditions are presented in Figures (6.1(a & b)), respectively. Two different y positions are presented, $y^+ \approx 30$ and 800, as they represent the points closest to the wall and at the edge of the outer part of the boundary layer where the flow is subjected to an interface between the boundary layer and free-stream conditions, and therefore intermittently displays the properties of each.

The energy and dissipation spectra have been normalized by $(\langle\varepsilon\rangle\nu^5)^{1/4}$ and $(\langle\varepsilon\rangle\eta_K^5)$, respectively, and thus scaled using Kolmogorov scaling. As expected, for the cases where the flow is fully turbulent (near the wall, and at the edge of the boundary layer for the case with a turbulent free stream and thus the external intermittency is between boundary layer and free-stream turbulence), the scaled energy spectra follow Kolmogorov scaling at high wavenumber. For the measurement in the outer

50
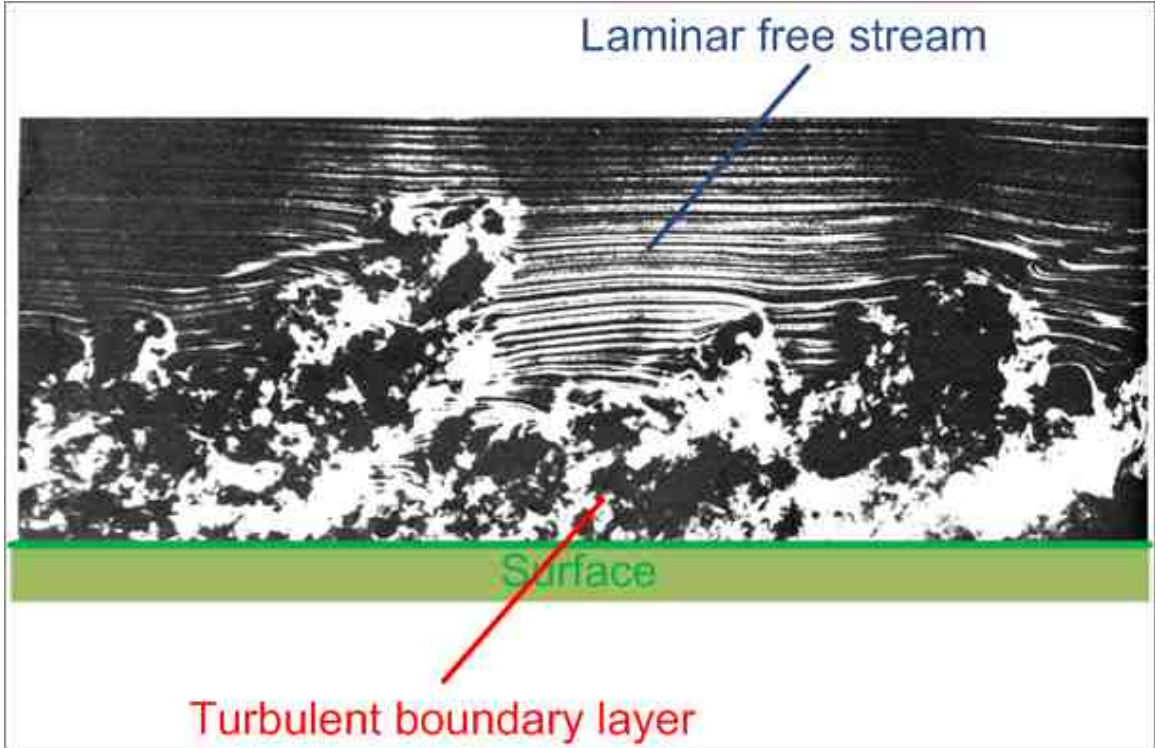
Figure 6.2: Smoke wire flow visualization of a turbulent boundary layer. Adapted from Dyke [69]

part of the boundary layer when the free stream is laminar and the external intermittency is between boundary layer turbulence and laminar flow this scaling does not hold and the corresponding spectra does not monotonically decay and deviates from Kolmogorov scaling at high wave-numbers.

This external intermittency is illustrated in Figure (6.2), which shows smoke-wire flow visualization of a turbulent boundary layer. It can be observed that there are instances where the free-stream flow extends very close to the wall. For a probe fixed at a y position, with the flow advecting past it, this will appear as intermittent laminar and turbulent behavior.

The corresponding estimated one-dimensional dissipation spectra, shown in Figure (6.1(b)), provide confidence that the entire dissipation range has been captured by the measurements. Whereas for the case where the flow is consistently turbulent the dissipation spectra appear log-normal, when laminar-turbulent external intermit-

tency is present the approximated one-dimensional dissipation spectra has a different appearance, being skewed towards larger scales and showing more content at wave-numbers above η_K.

6.2 Wall-Normal Dependence of the Turbulent Statistics

Comparison of the wall-normal dependence of the turbulent statistics measured for laminar and turbulent free-stream boundary layers is presented in Figure (6.3) with the inner-scaled dissipation, $\langle\varepsilon\rangle^+ = \langle\varepsilon\rangle 0.4/u_\tau^3$, and the Kolmogorov scale, $\eta_K^+ = \eta_K u_\tau/\nu$, presented in Figures (6.3(a & b)), respectively. In Figure (6.3(a)), the inner-scaled profiles of dissipation for both cases increase with wall-normal distance at the same rate up to $y^+ \approx 350$. At locations further from the wall, the mean dissipation rate of the case without free-stream turbulence decreases rapidly with increasing distance from the wall until reaching zero at the edge of the boundary layer to match the dissipation rate of the laminar free-stream. Conversely, for the boundary layer in the turbulent free-stream, there is always turbulence present, so the dissipation rate maximizes at $y^+ \approx 500$, above which the dissipation rate decreases down to the free-stream levels. Comparison of the mean dissipation rate indicates that the differences in the free-stream conditions largely influences the fine scale behavior only in the outer part. In this region we can consider there to be two different types of external intermittency depending on free-stream conditions. For the case with a laminar free-stream, the external intermittency is between the laminar free-stream flow and the turbulent boundary layer flow. For the case with a turbulent free-stream, the external intermittency is between the free-stream turbulence and the boundary layer turbulence.

The values of $\eta_K^+ = \eta_K u_\tau/\nu$ corresponding to the mean dissipation rate presented are provided in Figure (6.3(b)). As expected, η_K^+ increases with distance from the wall and, again, the difference between the two flow regimes occurs when $y^+ \gtrsim 350$.
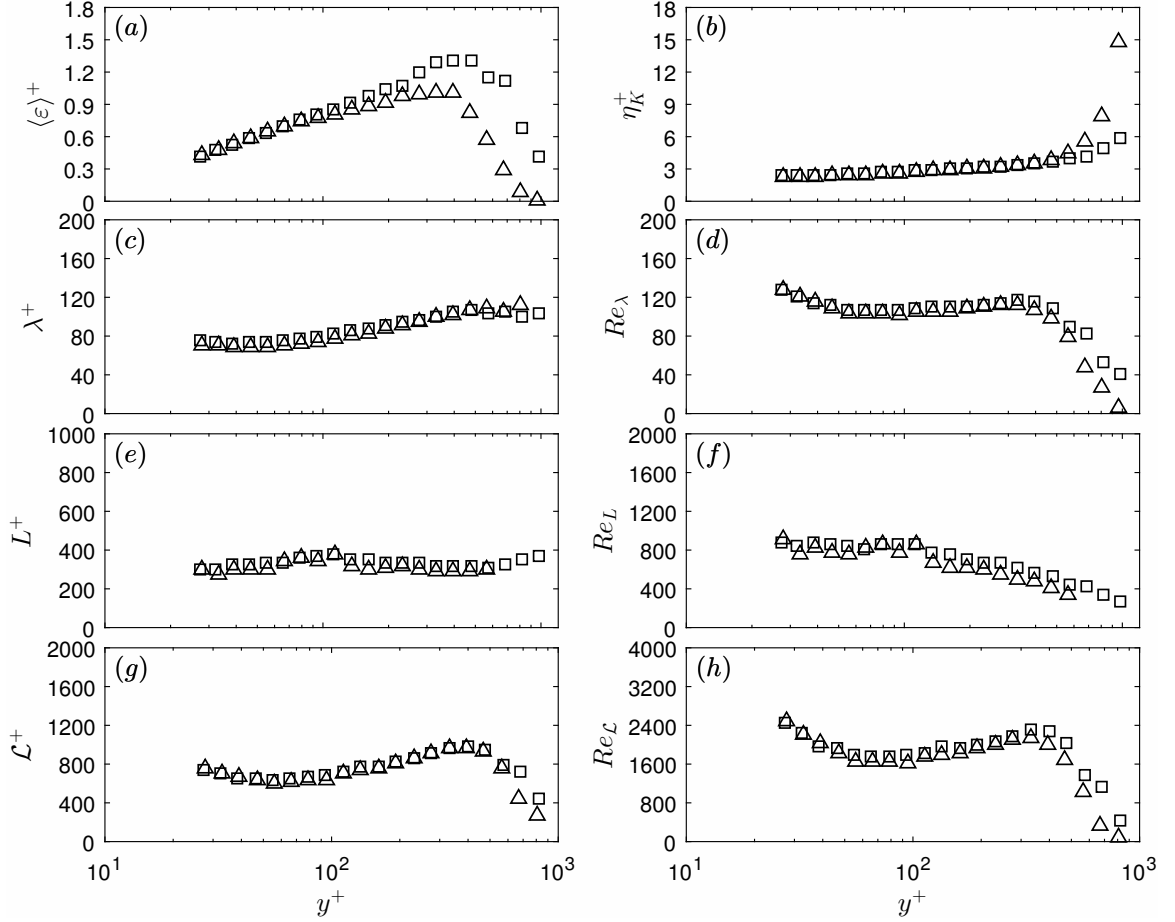
Figure 6.3: Wall-normal dependence of: (a) the inner scaled mean dissipation rate; (b) the inner scaled Kolmogorov scale; (c) the inner scaled Taylor micro-scale; (d) Taylor Reynolds number; (e) the inner scaled integral length-scale; (f) large-scale Reynolds number; (g) the inner scaled alternative large scale; and (h) alternative large-scale Reynolds number. Symbols are as in Table (4.1).

The Taylor micro-scale, providing intermediate length-scale between the large and small-scale statistics, was determined from

$$\lambda \approx \left(\frac{30\nu \langle u_1^2 \rangle}{\langle \varepsilon \rangle} \right)^{0.5}. \tag{6.5}$$

Figure (6.3(c)) shows the profiles of wall-normal dependence of the inner-scaled Taylor micro-scale, $\lambda^+ = \lambda u_\tau / \nu$, for the two free-stream conditions. Unlike the Kolmogorov scale, the Taylor microscale changes very little across the boundary layer, and no difference is observed between the laminar and turbulent free-stream conditions. The

corresponding Taylor-scale Reynolds number was estimated from

$$Re_\lambda = \frac{\lambda \langle u_1^2 \rangle^{0.5}}{\sqrt{2}\nu}. \tag{6.6}$$

There is little variation in Re_λ, remaining between 100 and 120, for $y^+ < 350$, with its maximum value occurring near the wall. Closer to the edge of the boundary layer, however, there is a rapid drop in Re_λ, slightly delayed for the turbulent free-stream for which $Re_\lambda \approx 40$.

A key scaling parameter for the large turbulent eddies is the scale L and it is common practice to use the integral length-scale to determine L. To find the integral length-scale we applied Taylor's hypothesis to the autocorrelation and integrated such that

$$L = \frac{\langle U_1 \rangle}{\langle u_1^2 \rangle} \int_0^{\mathcal{T}_c} \langle u_1(t + \mathcal{T}) u_1(t) \rangle d\mathcal{T}. \tag{6.7}$$

To minimize the impact of experimental bias and precision errors, which can result in a slow convergence in the integral, the integration was conducted up to $\mathcal{T}_c$, which was either the first zero-crossing of the autocorrelation, or the first inflection point, whichever value was lower. The inner-scaled profiles of integral length-scale $L^+ = Lu_\tau/\nu$ are shown in Figure (6.3(e)). In both laminar and turbulent free-streams, the integral length-scale remains largely constant at $L^+ \approx 0.4\delta^+$. Note that for the turbulent free-stream case, $L^+ \approx M^+$ and we should not expect to see much difference in the size of the large-scales between the turbulent boundary layer and free-stream turbulence. Note also that for the measurement points approaching and in the laminar free-stream, the value of L was beyond the scale of Figure (6.3(e)) and is not shown, as the integral scale calculated only reflects long wavelength oscillation in the free-stream conditions, as opposed to turbulent eddies.

To find the corresponding large-scale Reynolds number, $Re_L = \langle |\delta_L u| \rangle L/\nu$, the average velocity increment was estimated through time averaging $|\delta_L u| \approx |u_1(t + L/\langle U_1 \rangle) - u_1(t)|$ for all t. The resulting values of Re_L are presented in Figure (6.3(f))

and are found to be $\mathcal{O}(Re_\tau)$ near the wall, decreasing towards the edge of the bound-ary layer. Interestingly, for most of the boundary layer, the velocity and length-scales describing the large-scales of turbulence, $|\delta u_L|$ and L, appear to be less affected by the free-stream turbulence conditions than the Kolmogorov scales.

In summary, the boundary layers with and without free stream turbulence demon-strate identical wall-normal dependence of large- and small-scale statistics near the wall, diverging towards the edge of the boundary layer where external intermittency becomes increasingly important.

As noted by Bailey and Witte [37] the integral length-scale, L, is a poor indicator of the low-wavenumber boundary of the inertial cascade, as the calculation of L is biased by the presence of non-local, potentially 'inactive' [70], long-wavelength motions, for example the very-large-scale- and large-scale-motions e.g., [71, 72, 73]. As a result, the scaling parameter η_0 is biased as well, and becomes ineffective near the wall. Therefore we seek alternative descriptions for the large scales, which may be unbiased by the presence of these long-wavelength motions. In this respect, we note that it is possible to use dimensional arguments to define an alternative description of the large scales [8] using turbulent kinetic energy K and $\langle \varepsilon \rangle$ such that

$$\mathcal{L} = \frac{K^{3/2}}{\langle \varepsilon \rangle}. \tag{6.8}$$

Note that it is possible to modify this quantity to account for inhomogeneities through the introduction of an additional coefficient [74], however that is not done here as these coefficients typically bring $\mathcal{L}$ closer to L, whereas we require a quantity that will describe the more isotropic large scales. In the present experiments we use the isotropic approximation $K \approx 3/2\langle u_1^2 \rangle$ to calculate $\mathcal{L}$ in order to investigate the possibility of using it as a surrogate to L for describing the largest scales at the start of the energy cascade. A bias is likely to be introduced in our K estimate by the anisotropy in the large scales, which will bias high in the turbulent boundary layer due to the streamwise normal Reynolds stress being higher than the other two normal

components of the Reynolds stress. Hence $\mathcal{L}$ is likely to be slightly longer than would be found if the full three components of velocity were measured.

We also note that the estimate of $\mathcal{L}$ presented here assumes that the small scales are isotropic through the approach used for the calculation of $\langle \varepsilon \rangle$, necessitated by the measurements' inability to resolve the instantaneous velocity gradient tensor. However, the small scales may not be isotropic, as observed by Agostini and Leschziner [75] and also it is not expected that the small degree of anisotropy observed at small scales will have an appreciable impact on the calculation of $\mathcal{L}$.

Due to its dependence on K, which is a Reynolds number dependent quantity, there is some Reynolds number dependence in $\mathcal{L}$, which could impact the scaling of the dissipation scales. However, as can be observed in the study of Nedić et al. [74] most of this Reynolds number dependence is confined to $Re_\theta \leq 200$; above this value of Re_θ, there is very little Reynolds number dependence due to $\langle \varepsilon \rangle$ increasing proportionately with $K^{3/2}$.

In an analogy to Re_L we also introduce

$$Re_{\mathcal{L}} = \frac{\langle |\delta_{\mathcal{L}} u| \rangle \mathcal{L}}{\nu}, \tag{6.9}$$

where $\delta_{\mathcal{L}} u$ is the longitudinal velocity increment, defined in Equation (3.6), with $|r| = \mathcal{L}$. The wall-normal distribution of the inner-scaled $\mathcal{L}$ and $Re_{\mathcal{L}}$ for the two flow regimes are presented in Figures (6.3(g & h)), respectively. This scale is slightly larger than the integral length-scales, being closer to δ^+ and displays more wall-normal dependence. Due to its dependence on $\langle u_1^2 \rangle$ it drops significantly in the outer part of the boundary layer. In addition, there is effectively no dependence on free-stream conditions.

6.3 Dependence of Large Eddies length-scales and Taylor Reynolds Numbers on Large Scale Reynolds Numbers

The classical scaling prediction of $L/\eta_K \sim Re_L^{0.75}$ and $R_\lambda \sim Re_L^{0.5}$ (e.g., see Frisch [22]) is not well supported in a channel flow [37], most notably through the existence of different L/η_K values at the same Re_L, but different wall-normal positions. In the present case, the Re_τ is much lower and this effect is less readily apparent, as shown in Figures (6.4(a & b)). For example, in the near-wall region L and Re_L remains relatively constant, whereas η_K increases monotonically in the same region as can be observed in comparison of Figures (6.3(b,e & f)). The result is that L/η varies at constant Re_L as shown in Figure (6.4(a)). A similar comparison reveals that the variation in Re_λ does not have a commensurate variation in Re_L, resulting in the expected scaling not being observed in Figure (6.4(b)).

As noted previously, in the theory of turbulence, L is intended to represent scales at the start of the energy cascade region and have approximately Gaussian statistics. However, in turbulent boundary layer flows, the integral scale is much longer than δ and describes large-scale, anisotropic eddies, which are elongated in the streamwise direction. This leads to the integral scale being a poor metric to describe the start of the energy cascade, which is at the boundary of the universal equilibrium range; and therefore, should be approximately isotropic. Thus, defining Re_L using L in turbulent boundary layer flows is ineffective at capturing the same Reynolds number scaling observed in simpler flows.

Instead, Bailey and Witte [37] introduced a length-scale L^* to characterize the largest nearly isotropic energy-producing eddies in a channel flow. They assumed a validity of Townsend's attached eddy hypothesis, which states that in wall-bounded flows the scale of Reynolds-stress-contributing eddies depends on the distance from the wall, y, and cannot be larger than y since these eddies are confined by the wall. They therefore suggested that $L^* = 0.8y$ as an appropriate length-scale to describe
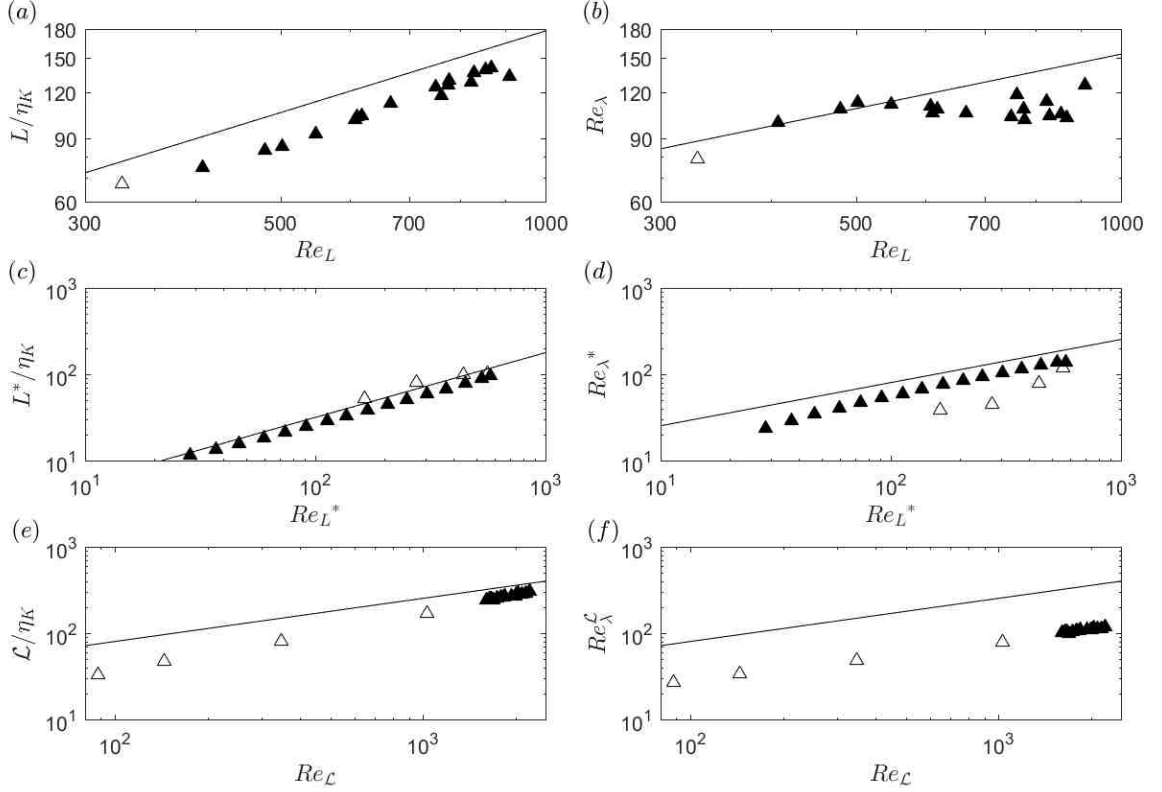
Figure 6.4: Dependence of (a) L/η_K and (b) R_λ on Re_L, dependence of (c) L^*/η_K and (d) Re_λ^* on Re_L^*, and dependence of (e) $\mathcal{L}/\eta_K$ and (f) $Re_\lambda^{\mathcal{L}}$ on $Re_{\mathcal{L}}$. Symbols are as in Table (4.1). Solid symbols indicate measurement locations where $y \leq 0.5\delta$.

the local, active contributions to the Reynolds stress, and upper bound of the inertial subrange. There is no theoretical foundation for choosing the constant of proportionality 0.8; however, it was determined to be the most effective value when normalizing the dissipative motions for $y \lesssim 0.5\delta$, the region where Townsend's attached eddy hypothesis has validity [37]. Correspondingly, they defined

$$Re_L^* = \frac{\langle |\delta_L u^*| \rangle L^*}{\nu}, \tag{6.10}$$

$$\lambda^* = \left(\frac{30\nu \langle |\delta_L u^*|^2 \rangle}{\langle \varepsilon \rangle} \right)^{0.5}, \tag{6.11}$$

and

$$Re_\lambda^* = \frac{\lambda^* \langle |\delta_L u^*| \rangle}{\sqrt{2}\nu}, \tag{6.12}$$

58

Figure 6.5: Sketch showing non-local influences of statistics by eddies centered at locations further away from wall than y position.

where λ^* is the revised Taylor micro-scale and Re_λ^* is its corresponding Reynolds number. It is therefore anticipated that L^* is a better descriptor for the energetic eddies at the upper limits of the universal equilibrium range, and thus leads to a value of the local-large-scale Reynolds number representing local contributions to Reynolds stress, particularly in the near-wall region of the boundary layer. An illustration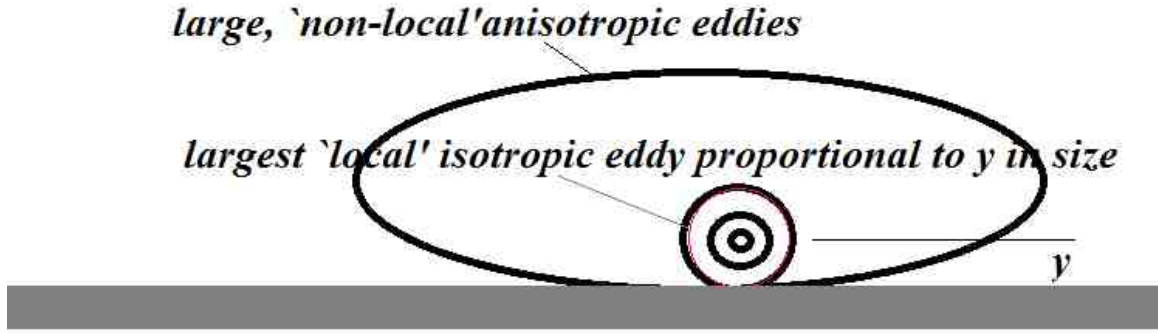 of how anisotropic, 'non local' large scales centered at locations further away from the wall than a specific y location can influence the statistics at y is presented in Figure (6.5). This sketch also illustrates how the largest isotropic eddies at y, would have a scale proportional to y.

Figures (6.4 (c & d)) show the dependence of L^*/η_K and Re_λ^* on Re_L^* for the two conditions of the free-stream, respectively. These two figures demonstrate the same improvement of scaling behavior observed in Bailey and Witte [37] through the agreement with the classical theory when $y/\delta \leq 0.5$. Thus, it is hypothesized that the scaling parameter L^* is a much better descriptor of the large-scale eddies at the start of the inertial subrange, at least for $y/\delta \leq 0.5$.

However, due to this limited range of applicability, we seek a better descriptor for the local large scales. Being based on the isotropic theory, $\mathcal{L}$ should be a better estimate for the top of the inertial subrange cascade, compared to L, and should work everywhere in the boundary layer. Therefore, we proposed the Reynolds number

scaling through the use of $\mathcal{L}$. Correspondingly we can introduce

$$\lambda^{\mathcal{L}} = \left(\frac{30\nu \langle |\delta_{\mathcal{L}} u|^2 \rangle}{\langle \varepsilon \rangle} \right)^{0.5},$$ (6.13)

and

$$Re_{\lambda}^{\mathcal{L}} = \frac{\lambda^{\mathcal{L}} \langle |\delta_{\mathcal{L}} u| \rangle}{\sqrt{2}\nu}.$$ (6.14)

The dependence of $\mathcal{L}/\eta_K$ and $Re_{\lambda}^{\mathcal{L}}$ on $Re_{\mathcal{L}}$ in the boundary layer for the two cases of the free-stream conditions is provided in Figures (6.4(e & f)), respectively. In both cases, there is monotonic behavior, with no indication of the non-uniqueness, which plagues the other two estimates for the scaling of the large eddies. Note that this is as expected, given that the scaling of Equation (6.8) is intrinsic to the scaling analysis used to produce the $L/\eta_K \sim Re_L^{0.75}$ and $R_{\lambda} \sim Re_L^{0.5}$ scaling relationships.

6.4   Probability Density Function (PDF) of the Local Dissipation Scales

The probability density function (PDF), also termed "probability distribution function", describes the frequency of occurrence of the values of the local-dissipative scale over a range of this scale.

To find the distribution of η, we use Equation (3.8) to define η and find the PDF of these scales $Q(\eta)$. This PDF is found by evaluating the local Reynolds number $|\delta_r u| r_1 / \nu$ throughout the measured time series and identifying instances where it is near unity. These instances are counted as an occurrence of a dissipation scale with $\eta = r_1$. Specifically, the $Q(\eta)$ distribution was calculated from each velocity time series using the following procedure, which was introduced in Bailey et al. [34]. To do so, the values of $|u_1(t + \Delta t) - u_1(t)| U_1 \Delta t / \nu$ was calculated for all t, resulting in a different value for each point in the time series. Then, the instances where this quantity was between 0.5 and 2, were counted as occurrences of dissipation at a scale $\eta = U_1 \Delta t$. Δt was then incremented by $1/f_s$ and the process was repeated. These counts were obtained up to $U_1 \Delta t = 4L$ resulting in a count, $q(\eta)$, of the total number

Figure 6.6: Forms of the PDFs of local dissipation scales from all measured positions within the boundary layer for the condition of a laminar free-stream.

of occurrences of η in the range $0 < \eta < 4L$. Finally, the PDF of η, $Q(\eta)$, was determined by normalizing such that

$$Q(\eta) = \int_0^{4L} q(\eta)d\eta = 1. \tag{6.15}$$

This process was repeated for all y positions within the boundary layer until profiles of the PDFs from all measured positions were generated.

Figures (6.6 & 6.7) show the PDFs of the local dissipation scales from all measured positions for a laminar and turbulent free-stream conditions, respectively. These distributions are skewed and biased toward the small scales, with a broad tail stretching into the large scales. The peaks of these distributions decrease and shift to the right with the wall-normal location. In both conditions, close inspection of these figures characterizes that these distributions do not collapse. To show a more detailed view

Figure 6.7: Forms of the PDFs of local dissipation scales from all measured positions within the boundary layer for the condition of a turbulent free-stream.

of the degree of collapse for all all measured positions in both conditions, the PDFs of the local dissipation scales are provided in Figures (6.8 & 6.9), respectively. These figures clearly characterized the difference between the PDFs of the two conditions
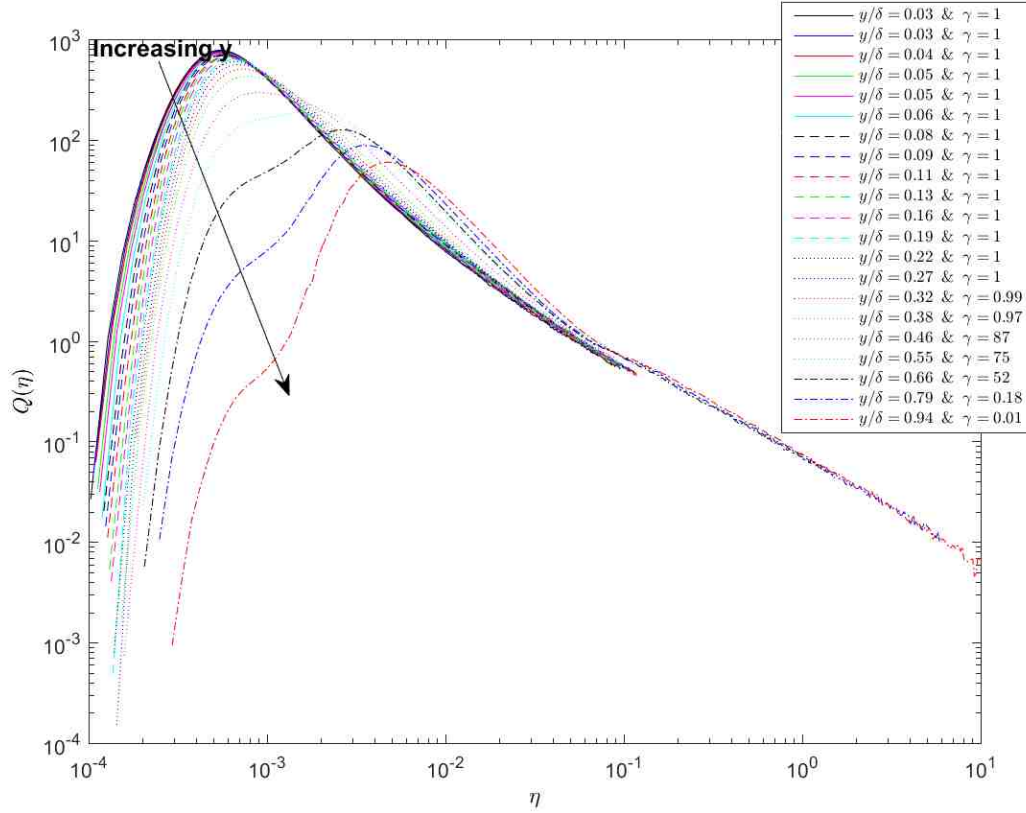

Figure 6.8: PDFs of local dissipation scales from all measured positions within the boundary layer for the condition of a laminar free-stream using linear axes.
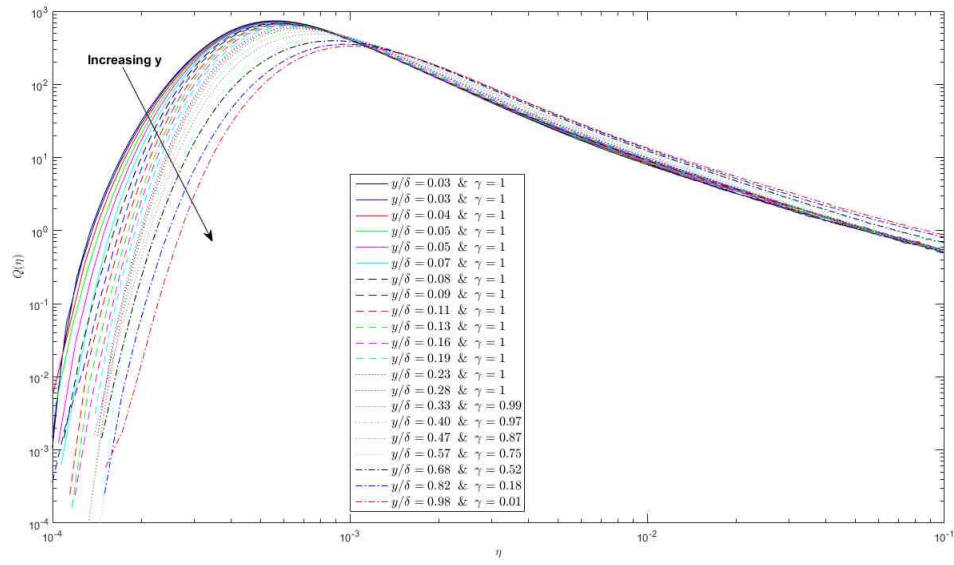
Figure 6.9: PDFs of local dissipation scales from all measured positions within the boundary layer for the condition of a turbulent free-stream using linear axes.

within the boundary layer. As expected, the PDFs of the laminar free-stream condition are highly skewed, comparing to the turbulent free-stream condition. The peak values of the PDFs are higher for the condition of the turbulent free-stream due to the higher turbulent intensity, especially in the outer part of the boundary layer.

6.5 Scaling of Local Dissipative Scales

We now seek to examine the scaling of the dissipative eddies within a turbulent boundary layer. As noted earlier, the scaling parameter, η_0, introduced by Yakhot and Sreenivasan [1] scales with the local large scale Reynolds number through $\eta_0 \approx LRe_L^{-0.73}$, and is analogous to $\eta_K \sim LRe_L^{-0.75}$. Hence, how the local large scales, L, are determined can strongly influence the value of the scaling parameter η_0.

As anticipated, L^* was a better descriptor for the energetic eddies at the upper limits of the universal equilibrium range, and thus leads to a value of the local-large-scale Reynolds number representing local contributions to Reynolds stress, particularly in the near-wall region of the boundary layer. Thus, $\eta^* = L^* Re_L^{*-0.73}$ would be a more

appropriate scaling parameter for the small scales, which was found to be the case for $y/\delta < 0.5$ in channel flow. However, due to this limited region of applicability, we seek a better descriptor for the local large scales. Being based on isotropic approximations $\mathcal{L}$ is potentially a better estimate for the top of the inertial subrange cascade than L and should work everywhere in the boundary layer. Therefore, in this section we investigate the scaling of the distribution of the dissipative scale, η, when using scaling parameters found by assuming that either L, L^*, or $\mathcal{L}$ are the appropriate descriptors for the large scales.

To investigate the suitability of the different descriptors of the large scales, three scaling parameters were used to normalize the PDFs of η:

(1) $\eta_0 = LRe_L^{-0.73}$ as introduced by Yakhot and Sreenivasan [1] and used by Schumacher [32] and Hamlington et al. [33];

(2) $\eta^* = L^*Re_L^{*-0.73}$ as suggested by Bailey and Witte [37]; and

(3) $\eta_{\mathcal{L}} = \mathcal{L}Re_{\mathcal{L}}^{-0.73}$ as proposed by Alhamdi and Bailey [76].

The PDFs of η determined from all y measurement positions normalized by η_0, η^*, and $\eta_{\mathcal{L}}$ are presented in Figures (6.10 (a)–(c)), respectively, for the case with a laminar free-stream.

As expected, the general shape of the distributions of the PDFs are in a good agreement with the previously reported distributions calculated both experimentally and numerically. Most notably, this is in the form of a skewed PDF biased towards the small scales, with a long tail towards the larger scales. For the most part, the maximum values of the PDFs are near $2.5\eta_0$, $3\eta^*$, and $2.2\eta_{\mathcal{L}}$, respectively. However, it can be observed that each of the scalings display regions of poor collapse, with the greatest deviations observed when the PDFs are scaled by η_0.

To provide a more detailed view of the degree of collapse near the wall under the different scalings, the PDFs for $y/\delta < 0.4$ are presented on linear axes in Fig-
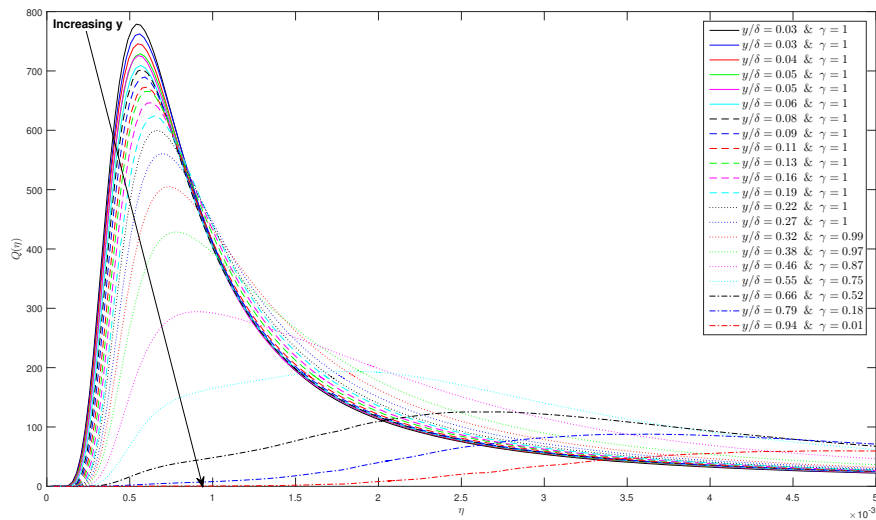
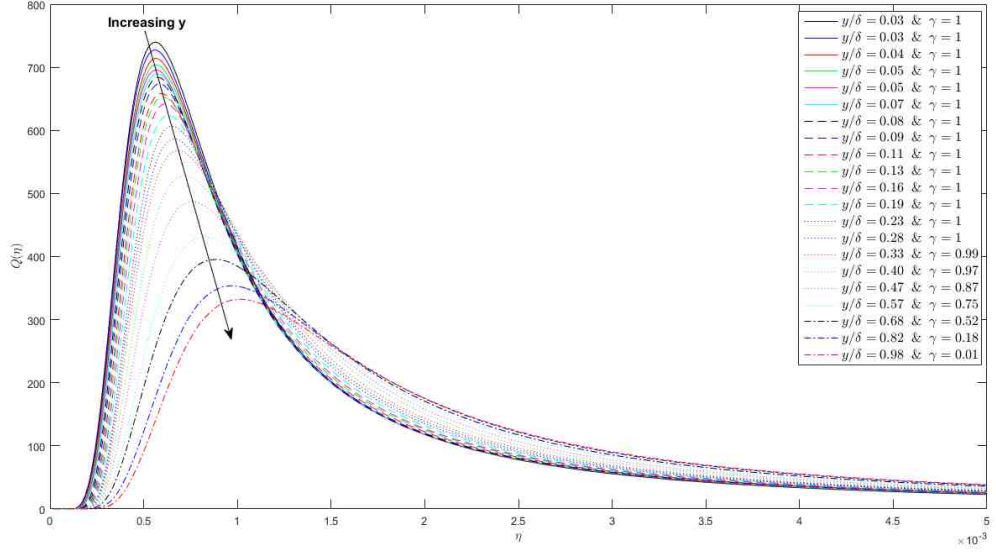Figure 6.10: PDFs of local dissipation scales from all measured positions within the boundary layer for the case with a laminar free-stream, normalized by: (a) η_0 ; (b) η^* ; and (c) $\eta_{\mathcal{L}}$.

ures (6.11(a)–(c)). Consistent with the observations of Bailey and Witte, scaling by η^* improves the collapse of the PDFs near the wall relative to that provided by η_0, indicating that the non-universality of the small scales and dependence on the large-scale shear observed by Morshed et al. [36] and Hamlington et al. [33] is due to the imperfect description of the large scales by L. When normalized by $\eta_{\mathcal{L}}$, there is a noticeable improvement relative to the η_0 scaled PDFs; however, it does not provide the same degree of collapse provided by η^*. This is most noticeable in the shift of the peak of $\eta/\eta_{\mathcal{L}}$.

To examine the dependency of the collapse of the PDFs on the distance from the wall, the PDFs measured throughout the entire boundary layer are presented in the

Figure 6.11: Measured PDFs of local dissipation scales for the case with a laminar free-stream using linear axes, normalized by: (a) η_0 ; (b) η^* ; and (c) $\eta_{\mathcal{L}}$ for $y/\delta < 0.4$. The wall-normal dependence of the PDFs are shown normalized by: (d) η_0 ; (e) η^* ; and (f) $\eta_{\mathcal{L}}$.

form of isocontours of probability in Figures (6.11(d)–(f)) for the PDFs scaled by η_0, η^* and $\eta_{\mathcal{L}}$. It can be observed from these isocontours that the greatest deviations from universal scaling don't appear near the wall, as occurs in channel flow, but actually occur for $y^+ > 350$ (or, alternatively, $y/\delta > 0.35$). In this range, the PDFs normalized by all three scaling parameters vary non-monotonically, with the highest probabilities shifting to larger values than those observed near the wall as y increases before shifting to smaller values near the edge of the boundary layer. We can attribute this non-universality to the effect of the external intermittency that exists in the wake region of the boundary layer. In this region, the flow will be intermittently laminar and turbulent, with the relative fraction of laminar to turbulent flow increasing towards the edge of the boundary layer. Hence, the PDFs of η will be increasingly impacted as the instances of laminar flow in the time series increase in frequency and length towards the edge of the boundary layer and increasingly biases the calculation of $Q(\eta)$, which does not discriminate between laminar and turbulent flow.

To support such an intermittency argument, we can look at equivalent scaling of the PDFs for the case with free-stream turbulence. Although intermittent behavior is still present this case, even when boundary layer turbulence is not present, there is still turbulence present in the free-stream fluid entrained into the boundary layer. Hence, the impact of the external intermittency on the PDFs of η should be reduced. The PDFs measured for all y positions when free-stream turbulence is present are shown in Figures (6.12(a)–(c)) scaled by η_0, η^*, and $\eta_{\mathcal{L}}$, respectively. In all cases there is improved agreement between the PDFs relative to that observed in Figure (6.10), with the best agreement throughout the boundary layer and into the free-stream is offered by the $\eta_{\mathcal{L}}$ scaling.

There is still some variation among the PDFs evident in Figure (6.12), and thus we present the wall-normal dependence of this variation in Figure (6.13), which shows the PDFs measured for $y/\delta < 0.4$ in Figures (6.13(a)–(c)) on linear axes and the wall-
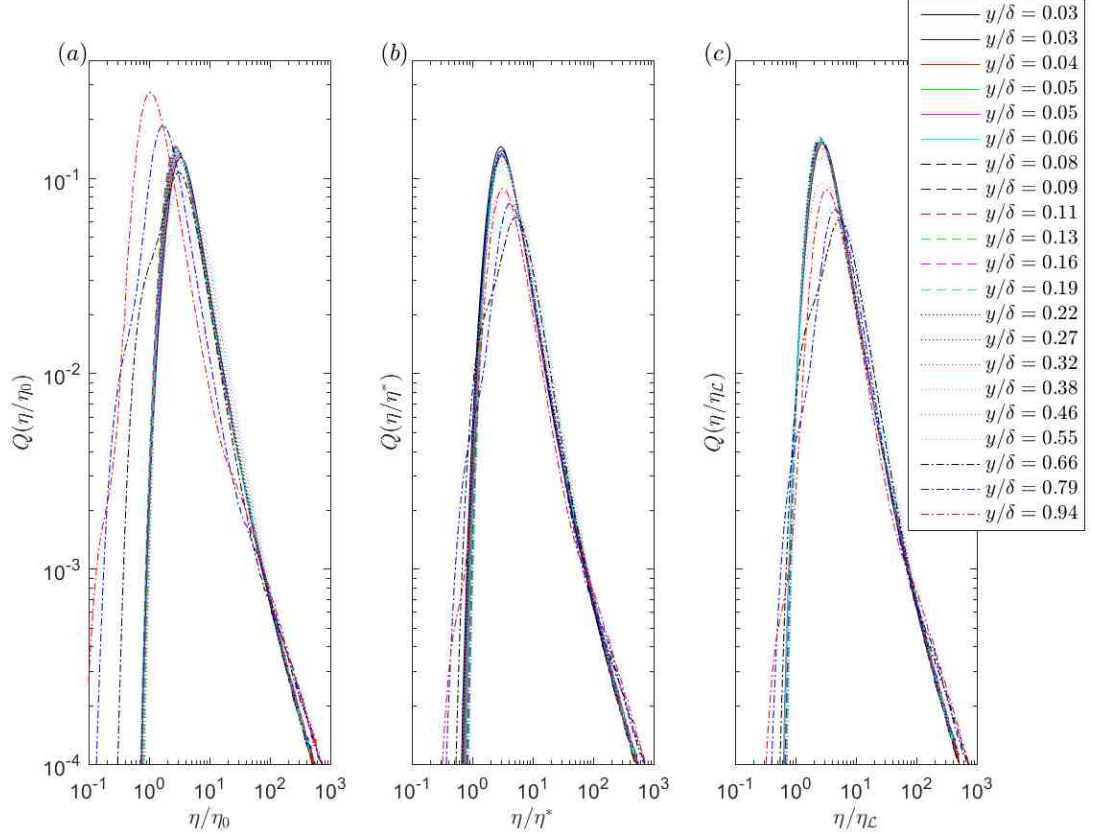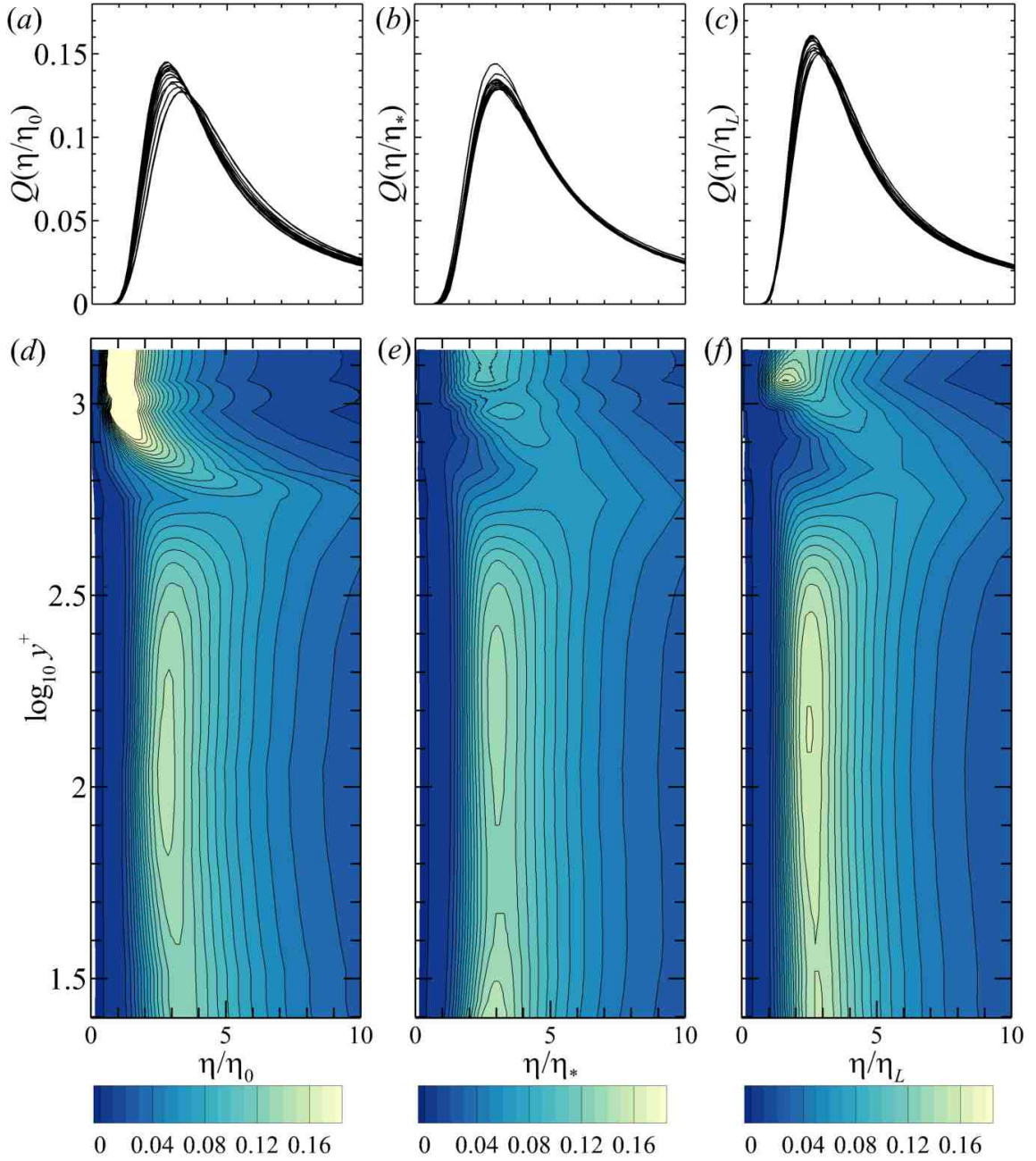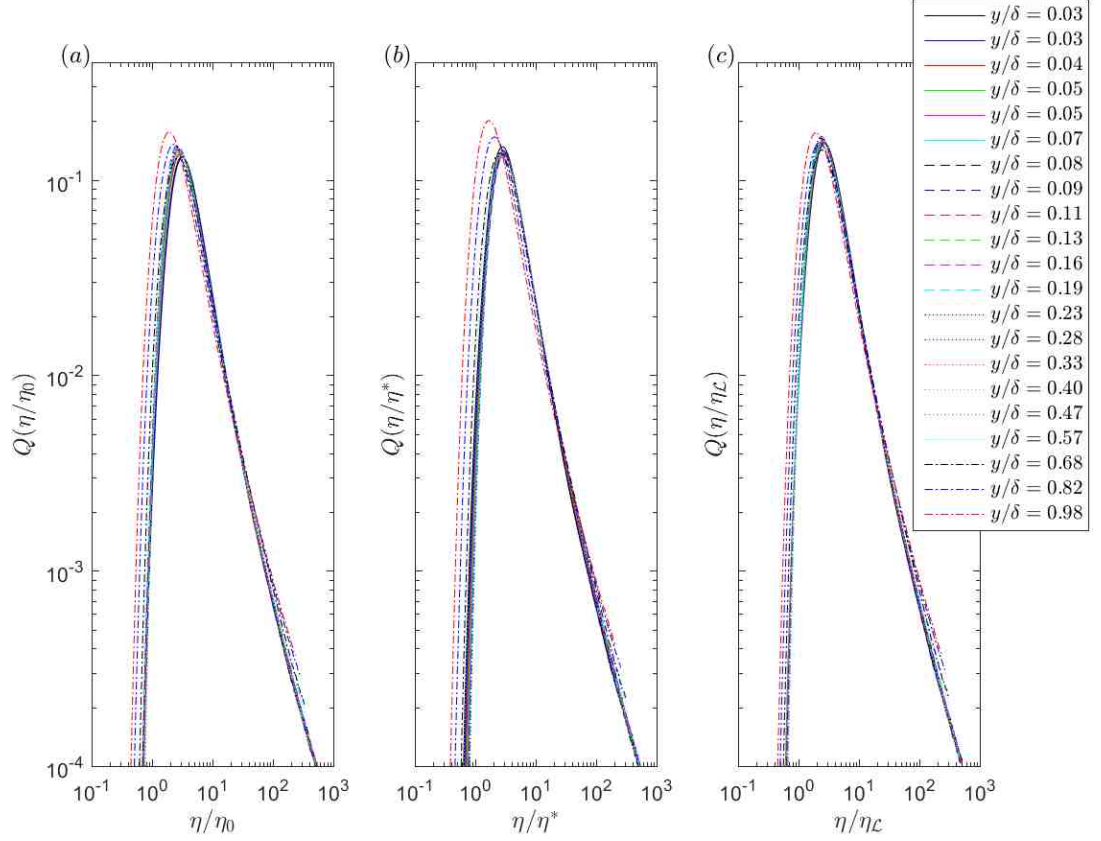
Figure 6.12: PDFs of local dissipation scales from all measured positions within the boundary layer for the case with a turbulent free-stream, normalized by: (a) η_0 ; (b) η^* ; and (c) $\eta_{\mathcal{L}}$.

normal dependence throughout the boundary layer via the corresponding isocontours of the PDF value in Figures (6.13(d)–(f)). As for the case with a laminar free-stream, the best scaling near the wall is produced by normalization by η^*.

The results shown in Figures (6.13(b & e)) scaled by η^* demonstrate the same improved collapse as in Figures (6.11(b & e)) when compared to the same PDFs scaled using η_0, consistent with the results of Bailey and Witte [37] that indicate η^* is a suitable parameter when $y/\delta \leq 0.5$. However, also consistent with the results of Bailey and Witte [37], η^* is increasingly unsuitable as a normalization parameter in the far-wall region $(y/\delta \gtrsim 0.5)$.

Conversely, although the $\eta_{\mathcal{L}}$ scaling does not work as quite as well in the near-
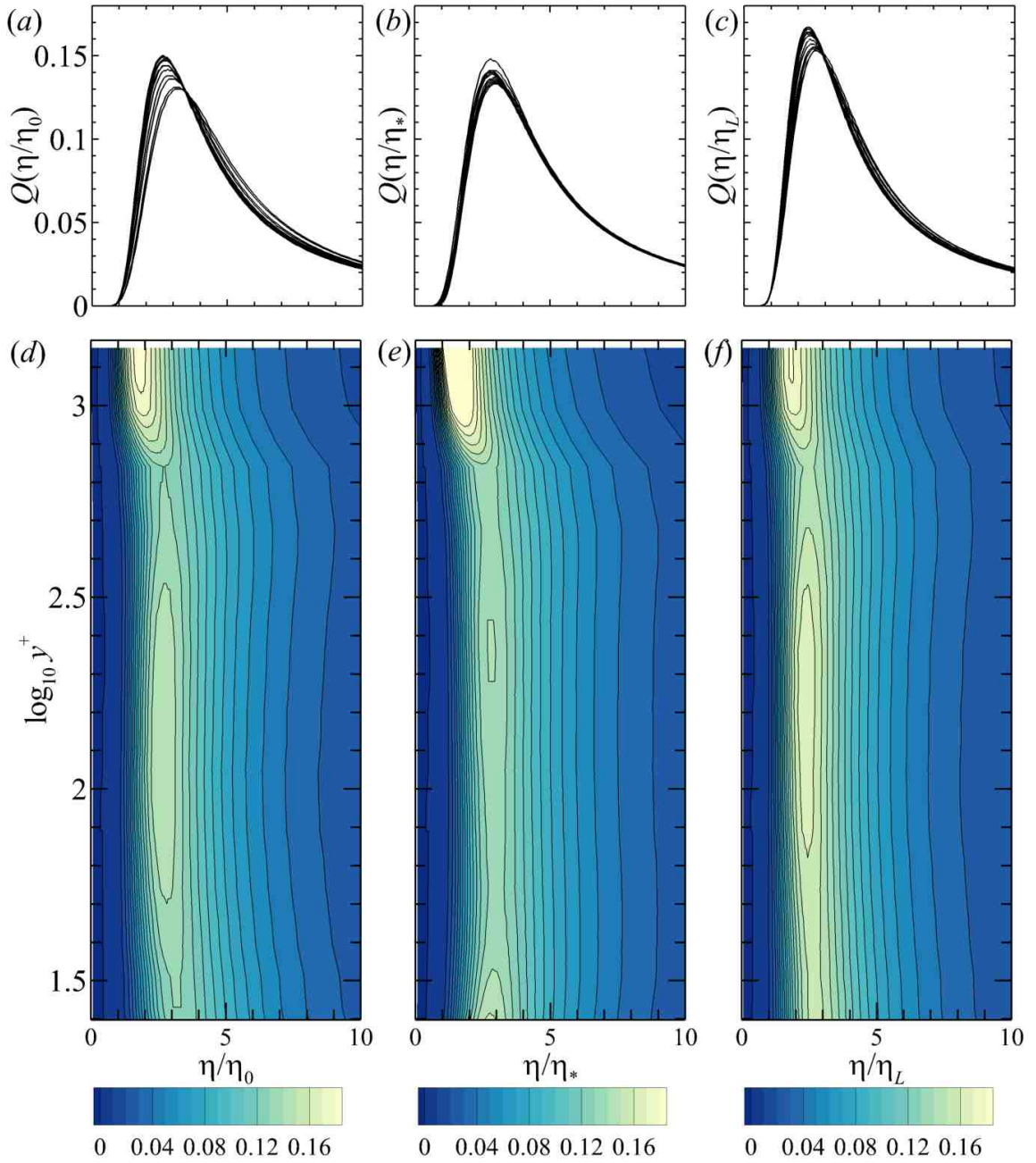
Figure 6.13: Measured PDFs of local dissipation scales for the case with a turbulent free-stream using linear axes, normalized by: (a) η_0 ; (b) η^* ; and (c) $\eta_{\mathcal{L}}$ for $y/\delta < 0.4$. The wall-normal dependence of the PDFs are shown normalized by: (d) η_0 ; (e) η^* ; and (f) $\eta_{\mathcal{L}}$.

wall region as η^*, it does display improved collapse throughout the boundary layer, as shown in Figure (6.12(c) & 6.13(f)), with the near-wall scaling comparable to that provided by η_0. Near the wall, there is improvement relative to η_0 when the PDFs are scaled by $\eta_{\mathcal{L}}$, with the near-wall scaling comparable to η^*.

Chapter 7 The Influence of External Intermittency on Local Dissipation Scales

7.1 Analysis of the External Intermittency

The scaling of the PDFs using $Re_{\mathcal{L}}$ that was proposed by Alhamdi and Bailey [76] and introduced in Section (6.5) in turbulent boundary layer flows with and without free-stream turbulence at $Re_{\tau} \approx 1000$ provided the best agreement so far throughout the entire depth of this boundary layer. However, in the outer part of the boundary layer, Alhamdi and Bailey [76] reported a significantly reduced collapse in the scaled PDFs. They attributed this lack of collapse to bias in the calculation of η introduced by the intermittent presence of laminar flow in the time series. To support this attribution, they found a significant improvement in the scaling of the probability density functions when the free-stream conditions were turbulent. Thus, it is expected that accounting for the external intermittency influence will improve the scaling of the PDFs, particularly for the condition of a laminar free-stream turbulence.

To account for the external intermittency in the calculation of the distribution of η requires first that we identify instances where the transition from one state to another occurs. In other words, a turbulence detection function must be employed.

The approach is illustrated in Figure (7.1). An example of the instantaneous streamwise velocity signal $U_1(t)$ is shown in Figure (7.1(a)), which is turbulent for some time interval and non-turbulent for the rest of the intervals. In the outer region of the turbulent boundary layer, the convection velocity of the non-turbulent flow, as it comes from the free-stream, is approximately U_{∞} (i.e. Corrsin and Kistler [38]; Fiedler and Head [44]; Kovasznay et al. [47]; Jiménez et al. [77]; Chauhan et al. [40]),
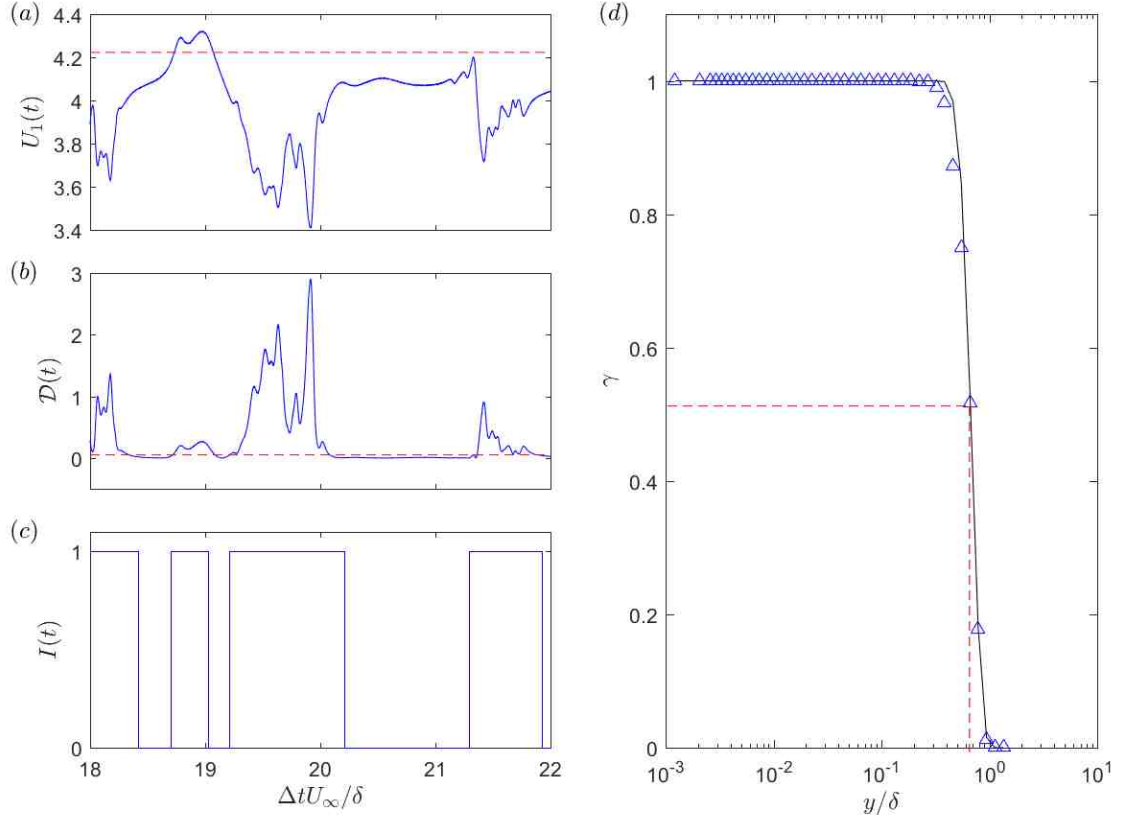
Figure 7.1: (a) Portion of instantaneous streamwise velocity measured at $y/\delta = 0.66$ by the hot-wire probe, with the dashed line indicating the free-stream velocity. (b) Corresponding detector function $\mathcal{D}(t)$ with the dashed line indicating the threshold used to identify turbulent/not-turbulence zones. (c) Corresponding binary intermittency signal with $I(t) = 1$ indicating the presence of turbulence and $I(t) = 0$ indicating a non-turbulent state. (d) Profile of average intermittency function, γ. Solid line indicates Equation (7.2) and dashed line indicates the wall-normal location where $\gamma = 0.5$, which occurs at $y/\delta \approx 2/3$.

which is denoted by the dashed line in Figure (7.1(a)). The detector function assumes that over the non-turbulent intervals of the signal, the fluctuations $U_1 - U_\infty$ are of the order of the free-stream intensity or less. Thus, we utilized a criterion to identify these turbulent/non-turbulent interfaces by applying a threshold value on a detector function $\mathcal{D}(t) = 100 \times [1 - U_1(t)/U_\infty]^2$ [40]. When $\mathcal{D}(t)$ is less than the threshold value, it is assumed to be non-turbulent flow, while it is higher than, or is equal to, this threshold value in the turbulent flow as shown in Figure (7.1(b)). In the present

72

case, to isolate the turbulent bulges the velocity time series was low pass filtered at 25 Hz using an eight order digital Butterworth filter (applied both in forward and backward time, to eliminate any phase lag introduced into the filtered signal) before calculating $\mathcal{D}(t)$. In addition, a threshold value of $\mathcal{D}_t = 0.05$, was used (indicated by the dashed line in Figure (7.1(b)), which corresponds to the 95% confidence level of a 1% standard deviation in the free-stream velocity.

Using this threshold value, the binary indicator $I(t)$ is determined where $I(t) = 0$ when $\mathcal{D}(t) < \mathcal{D}_t$ and the flow is considered to be non-turbulent, and $I(t) = 1$, when $\mathcal{D}(t) \geq \mathcal{D}_t$ and the flow is considered to be turbulent. The values of $I(t)$ for the example time series shown in Figure (7.1(a)) is presented in Figure (7.1(c)).

This calculation was conducted for all wall-normal locations to identify turbulent and non-turbulent regions at all wall-normal positions in the boundary layer. We denote the length of the turbulent intervals as ℓ_t and non-turbulent ℓ_{nt}, where ℓ_t and ℓ_{nt} are found from the duration in time of each segment multiplied by the average velocity within it.

At a specific wall-normal location where the streamwise velocity is measured, the average intermittency function, γ is calculated from

$$\gamma = \frac{1}{T_s} \int_0^{T_s} I(t)dt, \tag{7.1}$$

in which T_s is the sampling time.

In a turbulent boundary layer, the profile of $\gamma(y)$, has been found to be independent of Reynolds number [44] and can be represented with considerable accuracy by the error function as follows (see, for example Corrsin and Kistler [38]; Fiedler and Head [44], Hedley and Keffer [78], Chen and Blackwelder [79]):

$$\gamma(y) = \frac{1}{\sigma_Y \sqrt{2\pi}} \int_y^{\infty} exp\left[-\frac{(y-Y)^2}{2\sigma_Y^2}\right] dy. \tag{7.2}$$

Here Y is the mean interface position, which is the wall-normal location where $\gamma = 0.5$, and σ_Y is the standard deviation of the instantaneous interface position, y, relative
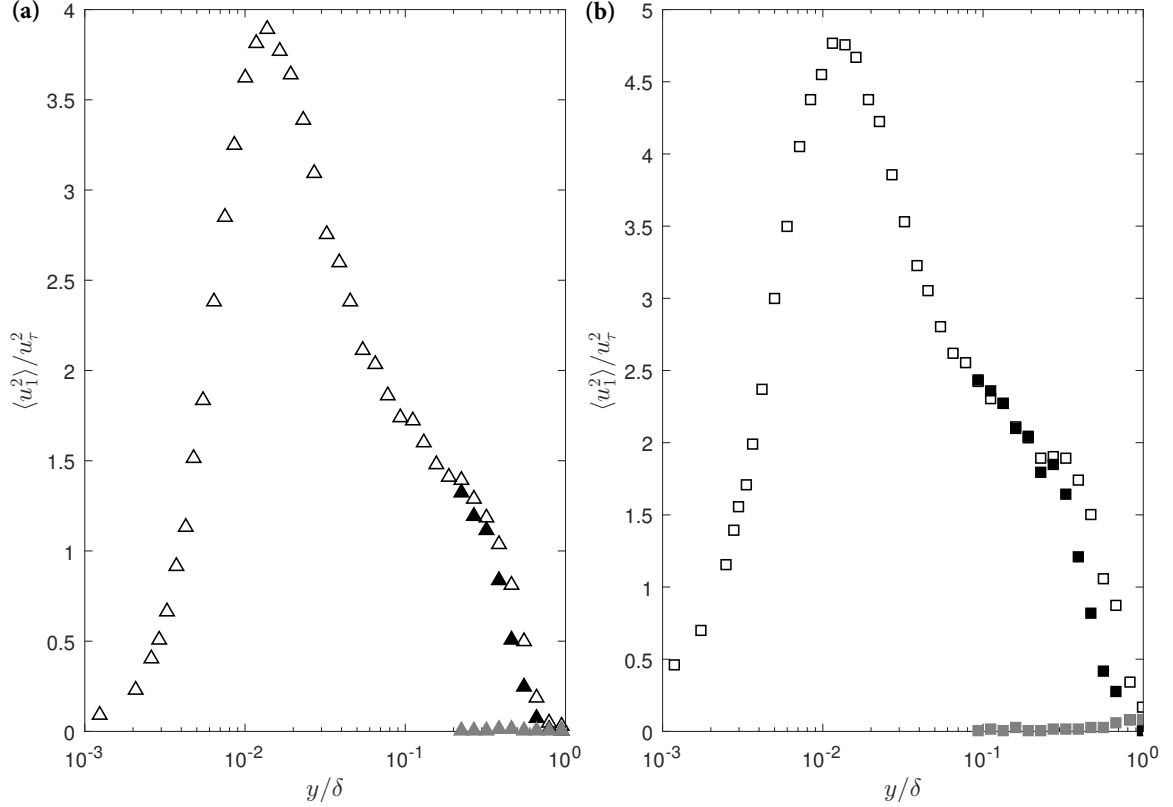
Figure 7.2: Profiles of Reynolds stress normalized by u_τ across the boundary layer for the case with a: (a) laminar; and (b) turbulent free-stream. Symbols are as in Table (4.1), with black symbols referring to the calculation using only instances where boundary layer turbulence is present and and grey symbols indicating instances where free-stream conditions are present.

to the mean location Y. Previous studies have found that $Y \approx 2/3\delta$ and $\sigma_Y \approx \delta/9$ for the turbulent boundary layer [40]. Figure (7.1(d)) shows the γ profile measured for the turbulent boundary layer in the present study and $Y/\delta = 0.66$ was found to correspond $\gamma = 0.52$. For comparison, the profile of γ produced by Equation (7.2) is also shown using $Y = 2/3\delta$ and $\sigma_Y = \delta/9$. A good agreement between these two profiles of γ was found, supporting the implementation of the $\mathcal{D}$ criterion, and the selected threshold value, to identify turbulent and laminar regions within this flow.

To affirm our argument of applying the $\mathcal{D}$ criterion and the selected threshold values to detect the external intermittency, we also used this detector function approach to distinguish between the turbulence and free-stream turbulence interfaces

in the case with free-stream turbulence. However, a threshold value of 0.12 is applied to detect the interfaces at wall-normal locations of the external intermittency since the free-stream intensity is higher in this case. The streamwise Reynolds stress normalized by u_τ across the boundary layer is provided in Figure (7.2) for the two free-stream conditions. As expected, the distribution of the Reynolds stress agrees with the previously reported experimentally and numerically (i.e. Lee and Sung [80]) for turbulent boundary layer at around the same Re_θ. The budgets of Reynolds stresses for the two free-stream conditions in the outer part of the boundary layer are compared. It is found that when the streamwise Reynolds stress has been calculated only using instances where boundary layer turbulence is present, the profiles measured in the two different free-stream conditions match. These findings also support the implementation of the $\mathcal{D}$ criterion, and the selected threshold value.

7.2 The External Intermittency Effect on the Scaling of the Local-Dissipative Scales

Experimental determination of η and its PDF from hot-wire data has been conducted in boundary layer flow with a laminar and turbulent free-stream conditions in Section (6.5). The present study essentially follows the same procedure, but had to be modified to account for the external intermittency.

Using the indicator function $I(t)$, the time series was segmented into discrete intervals and intervals where $I(t) = 0$ were discarded. To ensure that the length of time available was suitable for determining converged PDFs, intervals where $\ell_t < 2.5\delta$ were also discarded. The remaining intervals were then analyzed as independent time series. Where intermittency was not detected, the calculation proceeded as described in Sections (6.4). The calculation of the distribution of η requires identification of instances where $Re_\eta = |\delta_r u| r_1/\nu \sim 1$. To do this, $|\delta_r u|$ at each time t was estimated by assuming $r_1 \approx \langle U_1 \rangle \Delta t$, where $\langle U_1 \rangle$ was the average velocity within the segment of

the time series being analyzed, and $\delta_r u \approx [u_1(t + \langle U_1 \rangle \Delta t) - u_1(t)]$. For a particular discrete measurement time, t, Re_η was calculated over the range of Δt values up to the length of the time series. Each instance where Re_η was between 0.5 and 2 was counted as a single occurrence of dissipation at a scale $\eta = r_1$. This process was performed for all t to generate $q(\eta)$, the count of occurrences when $0.5 < Re_\eta < 2$ for each value of η.

A PDF of η could then be found by normalizing such that $\int q(\eta)d\eta = 1$ over the range 0 to $100\eta_{\mathcal{L}}$ where $\eta_{\mathcal{L}} = \mathcal{L}Re_{\mathcal{L}}^{*-0.73}$ is also used to scale the PDFs. Note, however, that the choice in scaling parameter is not expected to impact the efficacy of the intermittency compensation, as its influence is confined to the outer part. Scaling by $\eta_{\mathcal{L}}$ was conducted for simplicity, as it was found to be minimally impacted by the wall-normal location and is not bounded by ranges of validity, unlike η_0 and η^* and thus simplifies comparison across the boundary layer [76]. To calculate $\mathcal{L} = K^{3/2}/\langle \varepsilon \rangle$, K was necessarily approximated using an isotropic assumption as $1.5\langle u_1^2 \rangle$ and $\langle \varepsilon \rangle$ similarly approximated as $15\nu\langle U_1 \rangle^{-2}\langle (\partial u_1/\partial t)^2 \rangle$. For simplicity, these quantities were calculated from the full time series, as preliminary analysis indicated that the scaling remained unchanged when $\eta_{\mathcal{L}}$ was calculated from only the turbulent portion of the intermittent signal.

The use of these isotropic assumption to calculate dissipation rate was necessitated by the one-dimensional nature of hot-wire data. However, in Bailey and Witte [37] and Alhamdi and Bailey[76] the approach described above was compared to other methods for finding dissipation rate from hot-wire data and the results were found to be in agreement for $y^+ > 25$, with Kolmogorov scaling of the also one-dimensional spectra supported for this range. A greater bias is likely to be introduced by the $K = 1.5\langle u_1^2 \rangle$ approximation, which will bias $\mathcal{L}$ high due to anisotropy at the large scales. However, we have found the value of $\mathcal{L}Re_{\mathcal{L}}^{-0.73}$ to change only gradually with $\mathcal{L}$ and therefore we do not expect a significant deviation in the scaling behavior to

occur if mean dissipation rate and turbulent kinetic energy are calculated from the full three-component velocity vector and velocity gradient tensor.

Figure (7.3(a)) shows the distribution of the $Q(\eta/\eta_\mathcal{L})$ at different values of y/δ without accounting for the external intermittency (assuming the entire time series turbulent). For cases where γ is close to unity, the PDFs of η collapse on one another and are consistent with previously reported distributions determined experimentally and numerically in internal wall-bounded flows [34, 33, 81], as well as other turbulent flows [32, 82]. Specifically, these distributions are highly skewed and characterized by a broad tail stretching into the large scales, a peak near $\eta/\eta_\mathcal{L} \approx 2.2$ and a much narrower tail at small scales. However, for the cases where $\gamma < 0.9$ the PDFs become dependent on wall-normal position, both broadening and having the maximum shift to higher values of $\eta/\eta_\mathcal{L}$.

However, when only the instances where $I(t) = 1$ and $\ell_t > 2.5\delta$ are examined, as done in Figure (7.3(b)), the PDFs for $\gamma < 0.9$ recover the shape of those where $\gamma > 0.9$. The PDF for each segment is shown in this figure. For wall-normal locations where γ is high, there are very few instances where the flow was identified as being laminar, and there are fewer, longer segments, which improves statistical convergence of the PDFs. As γ decreases, there is an increasing number of shorter segments, which were analyzed, and there is greater scatter observed. At very low γ, the number of segments, which were longer than 2.5δ, were fewer. This limited the number of PDFs, which could be calculated at a particular wall-normal location.

To provide a more rigorous comparison of the PDFs across the different wall-normal locations, Figures (7.4(a & b)) show the PDF at each location in linear axes for the range 0 to $10\eta_\mathcal{L}$. The case where the entire time series is treated as turbulent is presented in Figure (7.4(a)), whereas the case where only the turbulent segments of the time series are examined is presented in Figure (7.4(b)). For Figure (7.4(b)), the PDFs of each segment at a particular wall-normal distance were averaged to
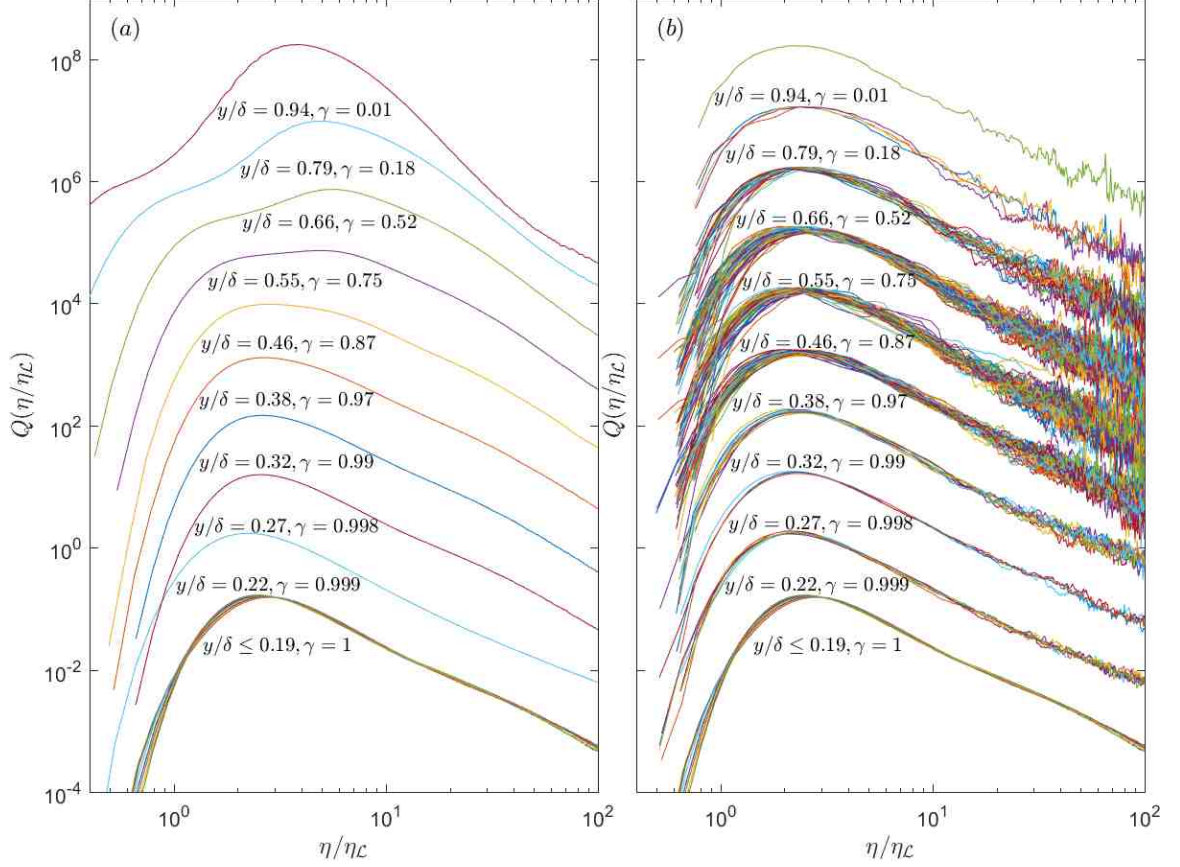
Figure 7.3: Comparison between the measured PDFs of local dissipation scales when (a) treating the entire time series as turbulent and (b) accounting for the external intermittency. For cases where $\gamma < 1$ (i.e. $y/\delta > 0.19$), each wall-normal position has been shifted up by a decade for clarity.

produce $\langle Q(\eta/\eta_{\mathcal{L}}) \rangle$. Comparison between these figures demonstrates the improvement in scaling across the boundary layer when only the turbulent portions of the time series are considered.

The corresponding wall-distance dependence of these PDFs is demonstrated in the isocontours of $Q(\eta/\eta_{\mathcal{L}})$ shown in Figures (7.4(c & d)) as functions of y/δ and $\eta/\eta_{\mathcal{L}}$, again using linear scaling. Figure (7.4(c)) shows that the greatest deviations from universal scaling occur for $y/\delta > 0.35$. In this range, the PDFs vary non-monotonically, with the highest probabilities shifting to values larger than those observed near the wall as y increases until the most deviating occurs at $y/\delta \approx 0.6$ and $\gamma \approx 0.5$, before shifting to smaller values near the edge of the boundary layer. Conversely, when
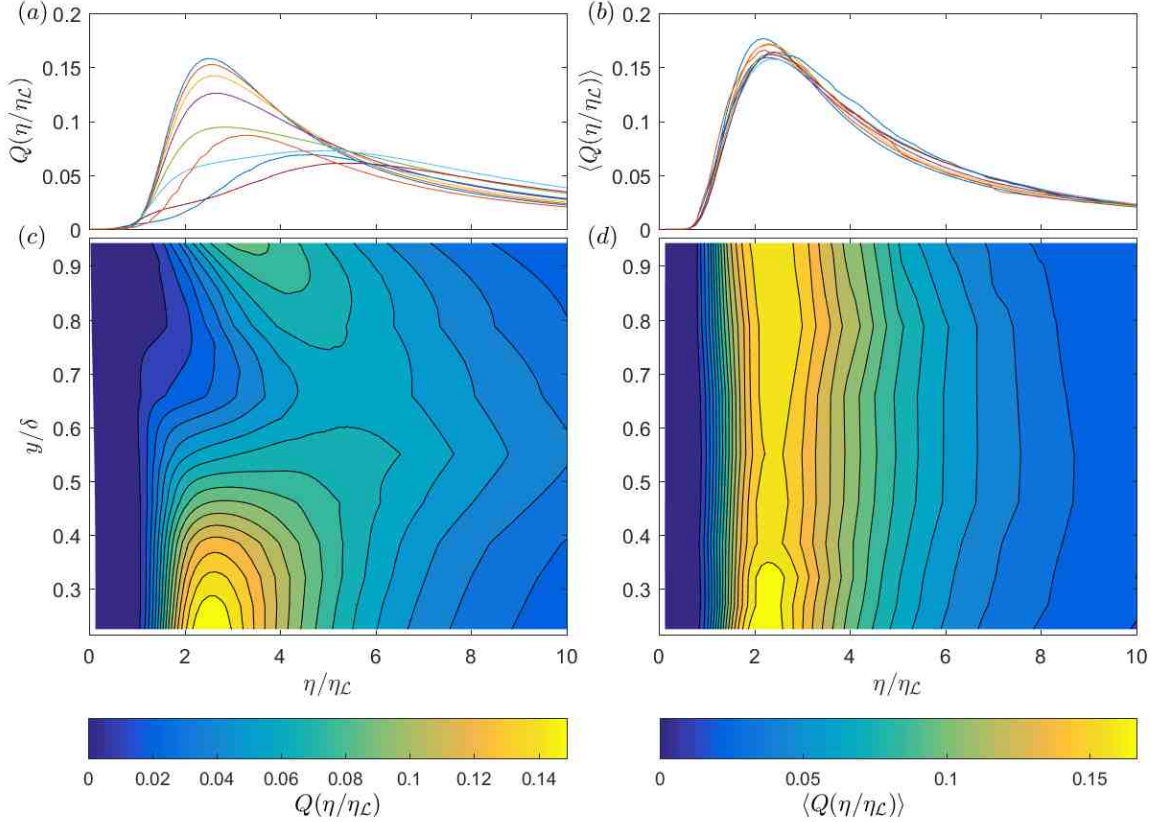
Figure 7.4: PDFs of η for cases with $\gamma < 1$ when (a) treating the entire time series as turbulent and (b) accounting for the external intermittency. For (b), the average values of the PDFs at a specific wall normal position when the flow is intermittent are presented. Corresponding isocontours of $Q(\eta/\eta_{\mathcal{L}})$ as a function of $\eta/\eta_{\mathcal{L}}$ and y/δ are shown in (c) treating the entire time series as turbulent and (d) accounting for the external intermittency.

only the turbulent segments of the time series are considered, this wall-dependence is effectively removed, as shown in Figure (7.4(b)). Here the maximum stays constant at $\eta/\eta_{\mathcal{L}} \approx 2.2$ and only a slight broadening of the PDFs is evident at larger $\eta/\eta_{\mathcal{L}}$ for intermediate wall distances.

These results confirm the hypothesis of Alhamdi and Bailey [76] that the wall-normal dependence of the PDFs in the outer part of the boundary layer can be attributed to bias introduced by the inclusion of periods of laminar flow in the calculation of η. More importantly, the results suggest that the boundary layer produces a universal distribution of the dissipative scales of turbulence, when turbulence is

79

present. Given the agreement of the results from the PDFs with those of other flows, there is consistent support for the existence of a universal distribution of these scales, which can be determined from a single scaling parameter.

Chapter 8 Conclusions and Future Work

8.1 Conclusions

Measurements of turbulent boundary layer with and without free-stream turbulence were conducted at $Re_\tau \approx 1000$ using a thermal anemometry probe. The data were utilized to investigate the scaling behavior of the distribution of dissipative scales within the boundary layer turbulence. Specifically, the collapse of the probability density functions of the dissipative scales was examined using normalizing parameters built from three selected measures of the large scale turbulence. These were the measured integral length-scale, an approximation based on Townsend's attached eddy hypothesis introduced by Bailey and Witte [37], and the length-scale built from the dimensional analysis of turbulent kinetic energy and dissipation rate.

The measured PDFs of η were consistent with those observed in other flows. Although, unlike turbulent channel flow, in the outer part of the boundary layer there was significantly reduced collapse in the scaled PDFs, irregardless of the scaling used. This lack of collapse was attributed to the bias in the calculation of η introduced by the intermittent presence of laminar flow in the time series. This attribution was supported by the significant improvement in the scaling of the probability density functions when the free-stream conditions were turbulent.

Within the near-wall region, the local large-scale defined based on distance from the wall was found to collapse the probability density functions for the lower half of the boundary layer. This observation is consistent with the prior observations of scaling within turbulent channel flow and supports the universality of the small-scale description of the turbulence for external wall-bounded flow. However, this scaling does not extend to the outer part of the boundary layer, even for the case of a

turbulent free stream. Instead, it was found that scaling the PDFs using a parameter built from the turbulent kinetic energy and mean dissipation rate provided the best agreement throughout the boundary layer.

Furthermore, contrasting to channel flow, in the outer part of the turbulent boundary layer, the normalized distributions of the local dissipation scales were found to be dependent on wall-normal position. This was observed to be attributable to the presence of external intermittency in this outer part.

Then, the effects of the external intermittency on the scaling of the dissipation scale distribution were investigated. The analysis employed a detection function to identify the turbulent and non-turbulent regions in the outer part where external intermittency exists. When only the turbulent portions of the time series are considered, the probability density functions of the dissipation scales from each portion of the time series collapse on each other, and result in a significant improvement in the scaling of the probability density functions across the depth of the turbulent boundary layer when normalized by $\eta_{\mathcal{L}}$.

This observation supports the universality of the small-scale description of the turbulence for external wall-bounded flow, using the alternative definition of the local large scale Reynolds number, $Re_{\mathcal{L}}$.

8.2   Future Work

The scaling of the PDFs using the alternative definition of the local large scale Reynolds number, $Re_{\mathcal{L}}$, after accounting for the external intermittency supports the universality of the small-scale description of the turbulence for external wall-bounded flow. This observation does not provide the same degree of collapse in the PDFs as the wall-dependent scaling, as this quantity converges on the integral length-scale for homogeneous isotropic turbulence. Thus, it should prove to be a more practical parameter to use in complex flows where the boundary layer thickness is not known

a priori.

It should be noted that the alternative definition of the local large scale Reynolds number, $Re_{\mathcal{L}}$, presented here has only been examined in the turbulent boundary layer flow at a low Reynolds number. It is not yet clear whether the scaling parameter, $\eta_{\mathcal{L}}$, will hold for other types of shear flows, or at higher Reynolds numbers. It is also not clear whether accounting for the external intermittency will generalize for other turbulent flows, or at higher Reynolds numbers.

Appendix A: Hot-wire Calibration for the Replicated Cases

Calibration of replicated cases of pre- and post-curve fitting for the laminar and turbulent free-stream conditions is provided below. These figure show a good agreement between pre- and post-measurement calibrations.
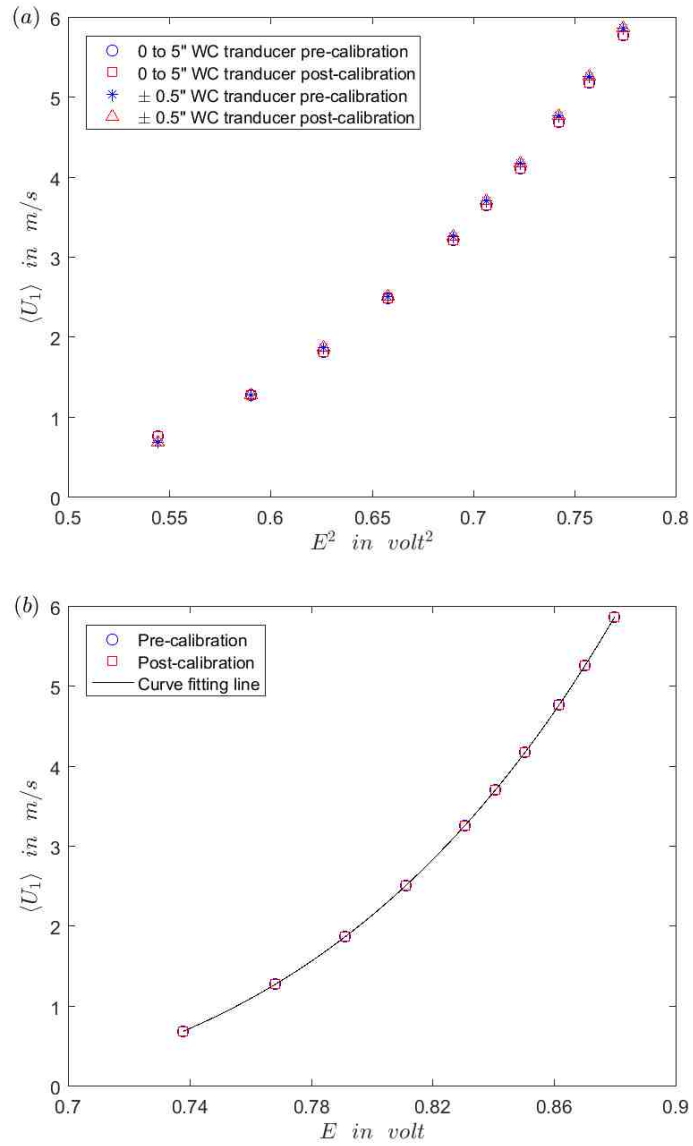

Figure B1: Calibration of the hot-wire reading for the first replication of the case with a laminar free-stream condition using pitot tube (a) before; and (b) after curve fitting.
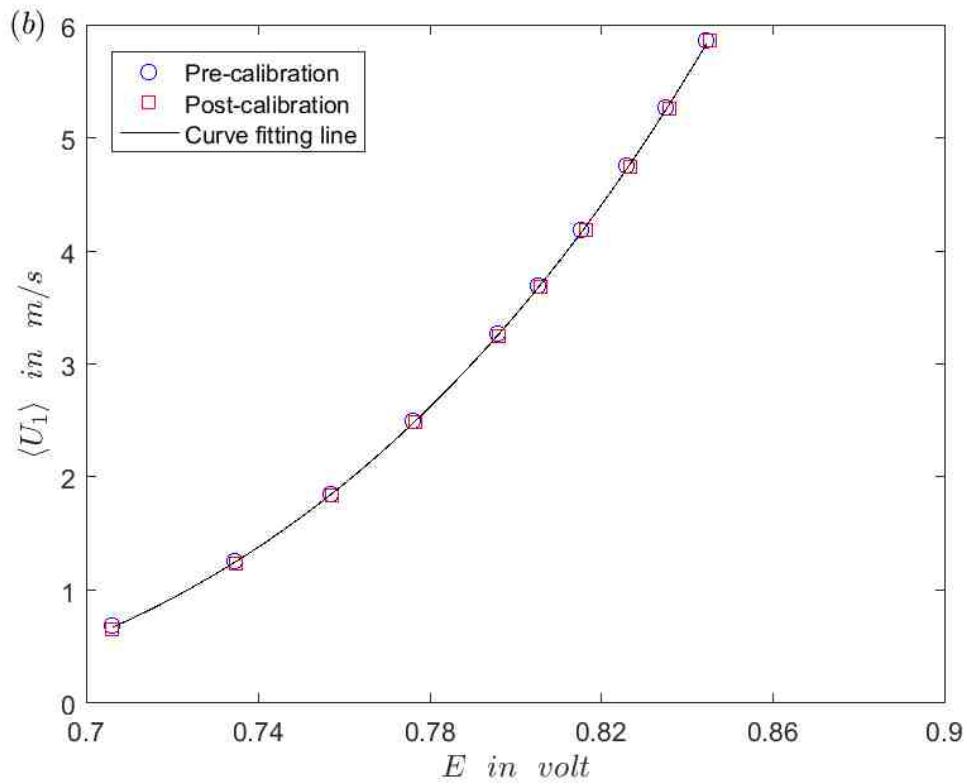
Figure B2: Calibration of the hot-wire reading for the second replication of the case with a laminar free-stream condition using pitot tube (a) before; and (b) after curve fitting.

Figure B3: Calibration of the hot-wire reading for the third replication of the case with a laminar free-stream condition using pitot tube (a) before; and (b) after curve fitting.
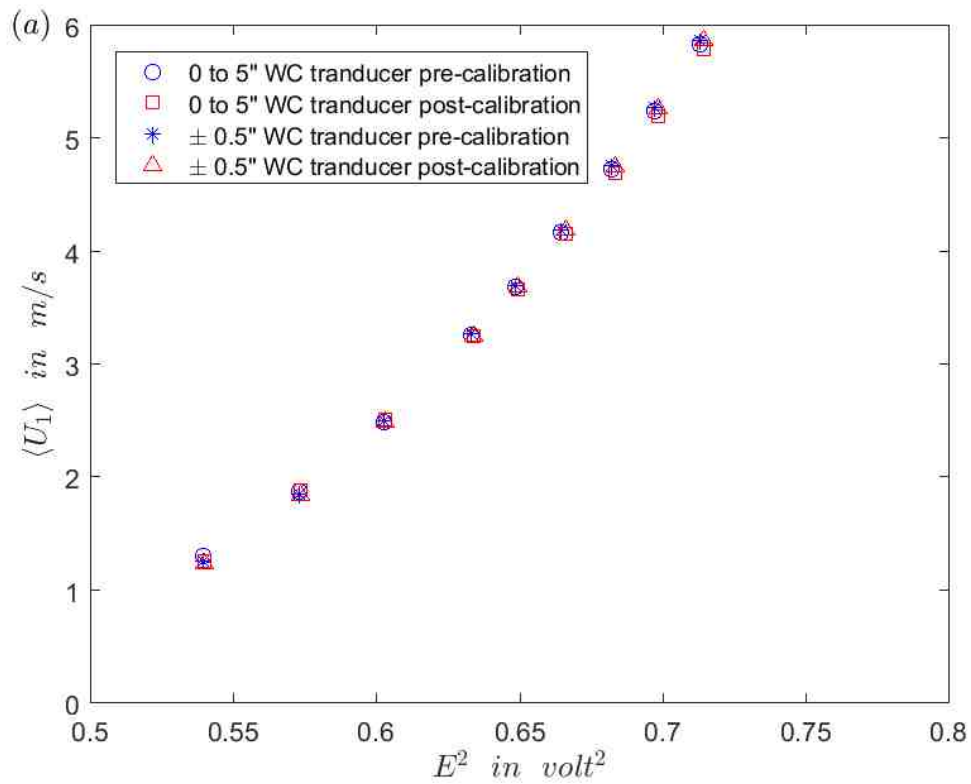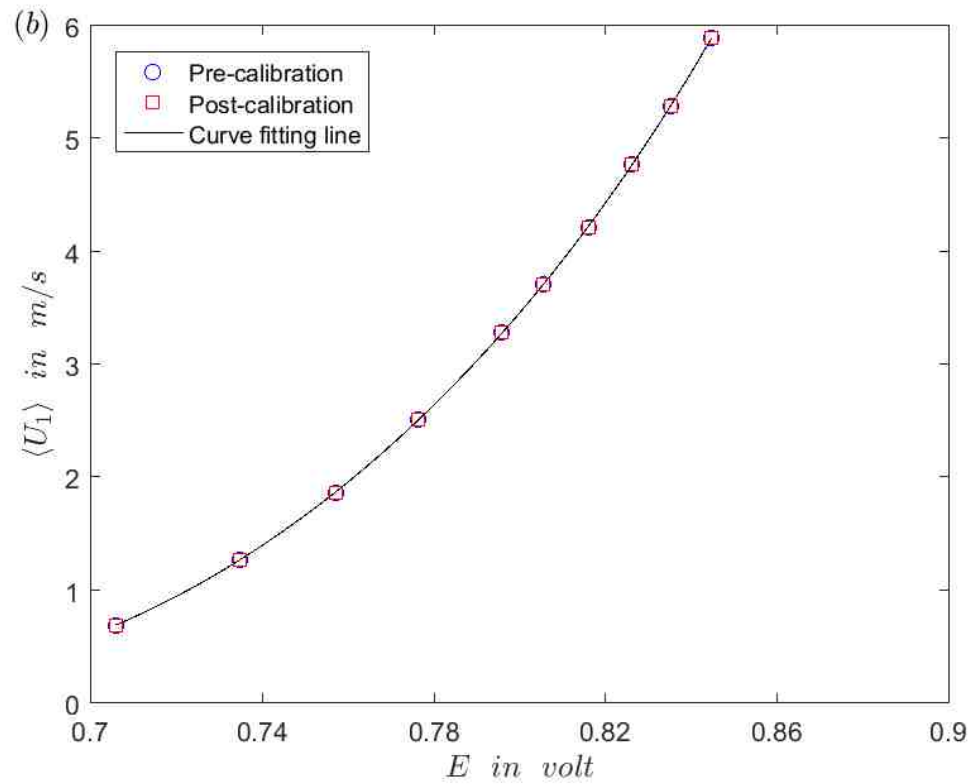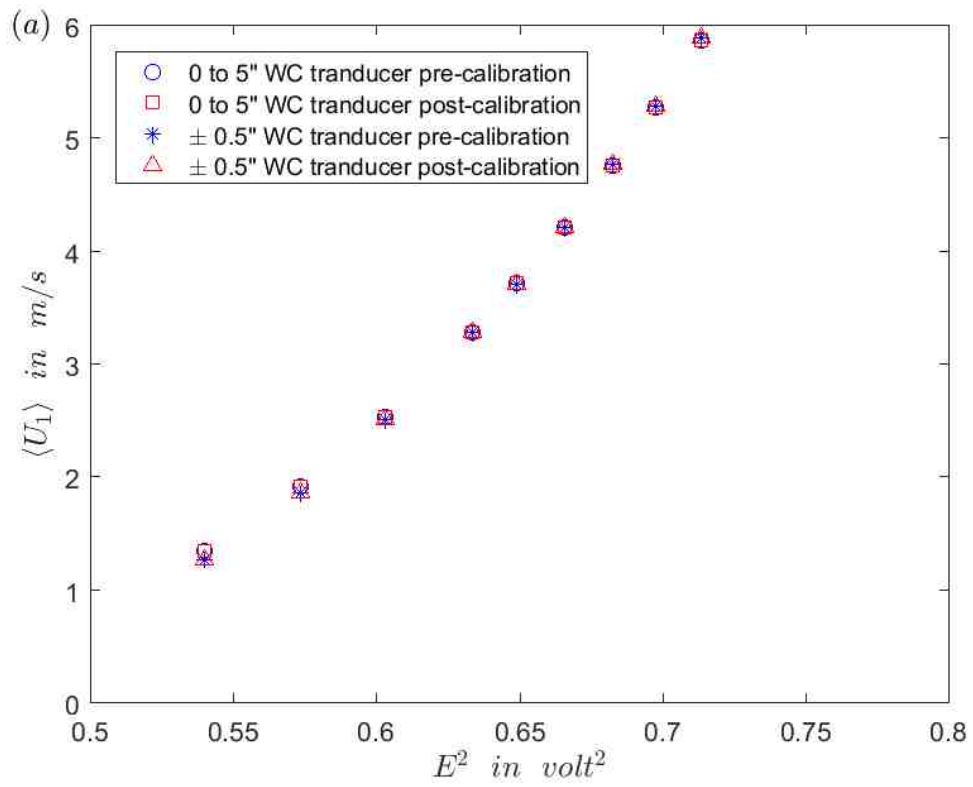
Figure B4: Calibration of the hot-wire reading for the first replication of the case with a turbulent free-stream condition using pitot tube (a) before; and (b) after curve fitting.
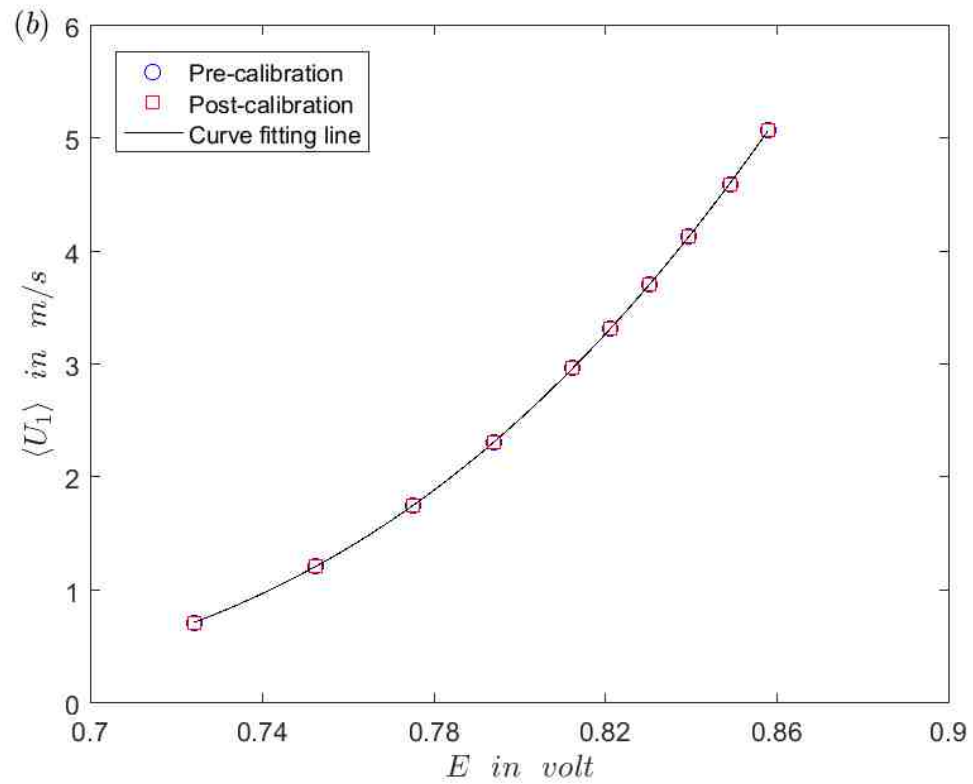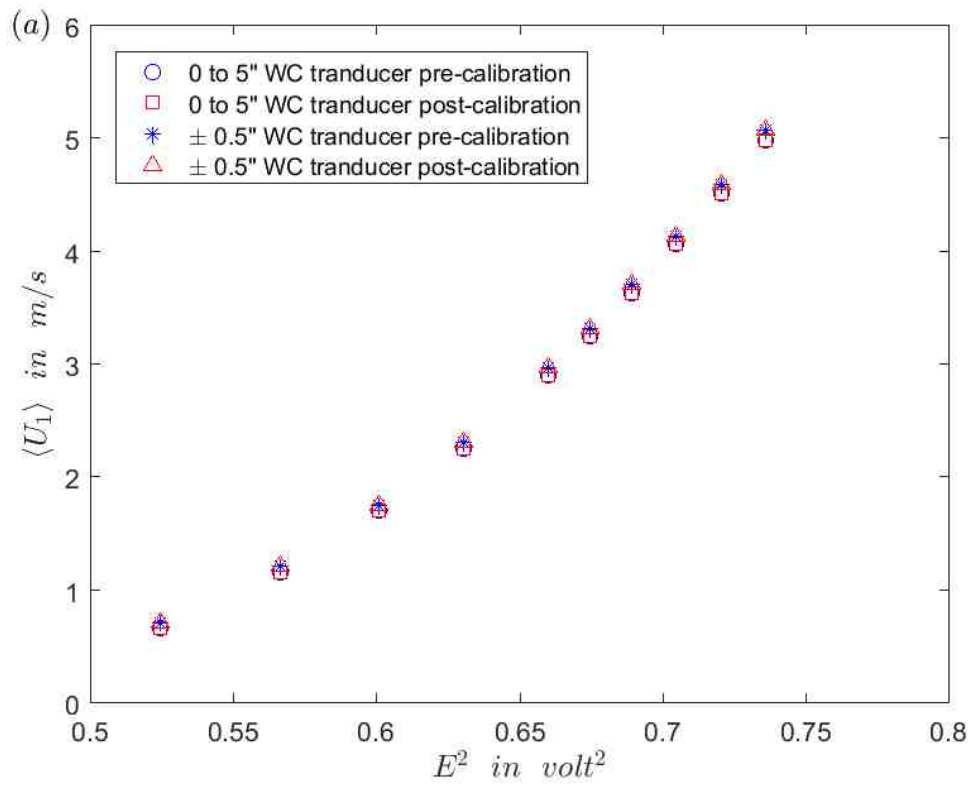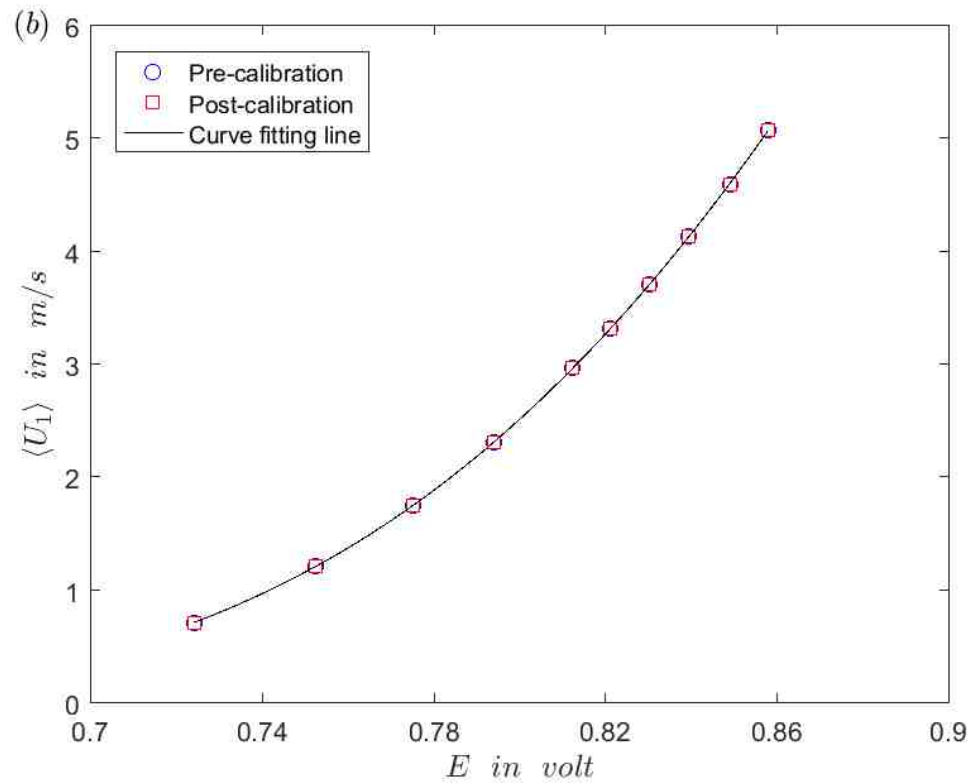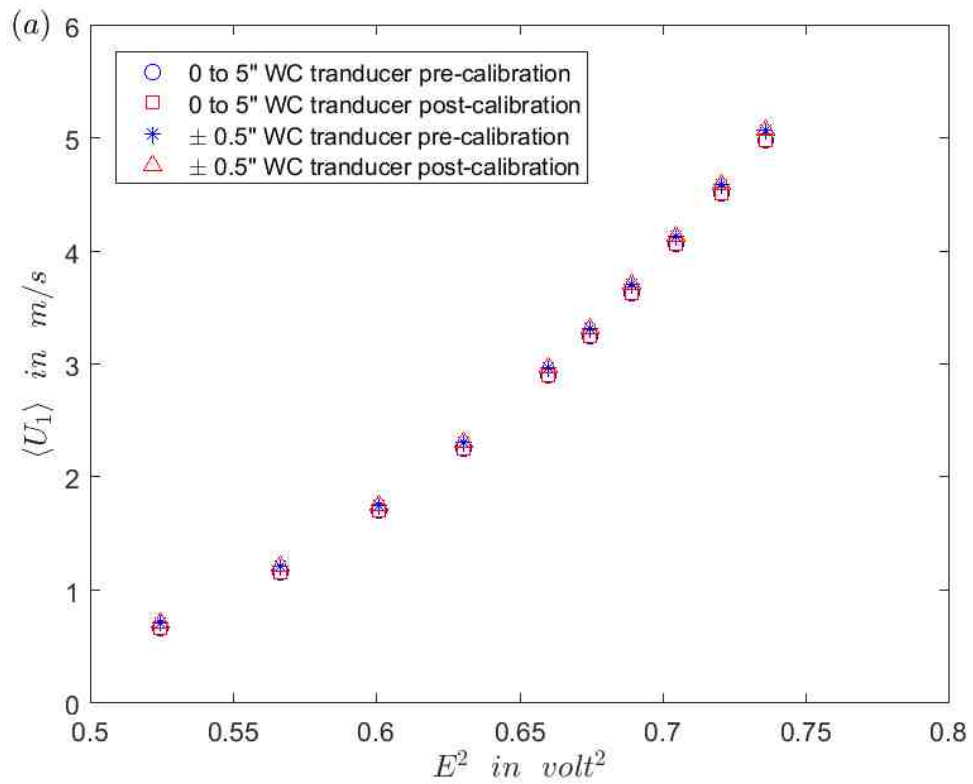
87

Figure B5: Calibration of the hot-wire reading for the second replication of the case with a turbulent free-stream condition using pitot tube (a) before; and (b) after curve fitting.

Appendix B: Universality

Measured PDFs from all Measures Locations:

The measured PDFs of local dissipation scales for both laminar and turbulent free-stream conditions using linear axes, normalized using η_0, η^*, and $\eta_{\mathcal{L}}$, are presented in the following two figures. In these two figures the PDFs are from all measured positions of $y^+ > 25$ within the boundary layer when the flow is intermittent. Comparison between the two free-stream conditions shows that the normalized PDFs profiles collapsed better with the local-dissipative scales when the free-stream turbulence presents.

Figure B1: Measured PDFs of local dissipation scales for the case with a laminar free-stream condition using linear axes, normalized by: (a) η_0; (b) η^*; and (c) $\eta_{\mathcal{L}}$ from all measured positions within the boundary layer when the flow is intermittent.

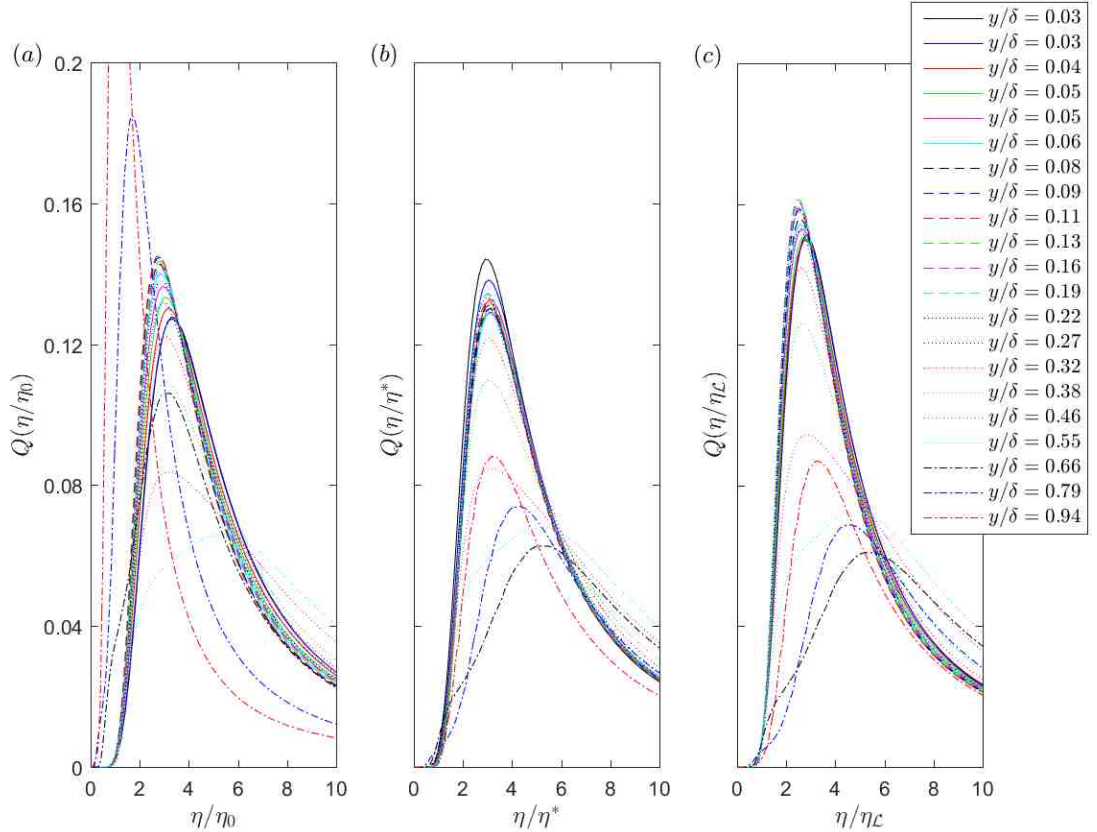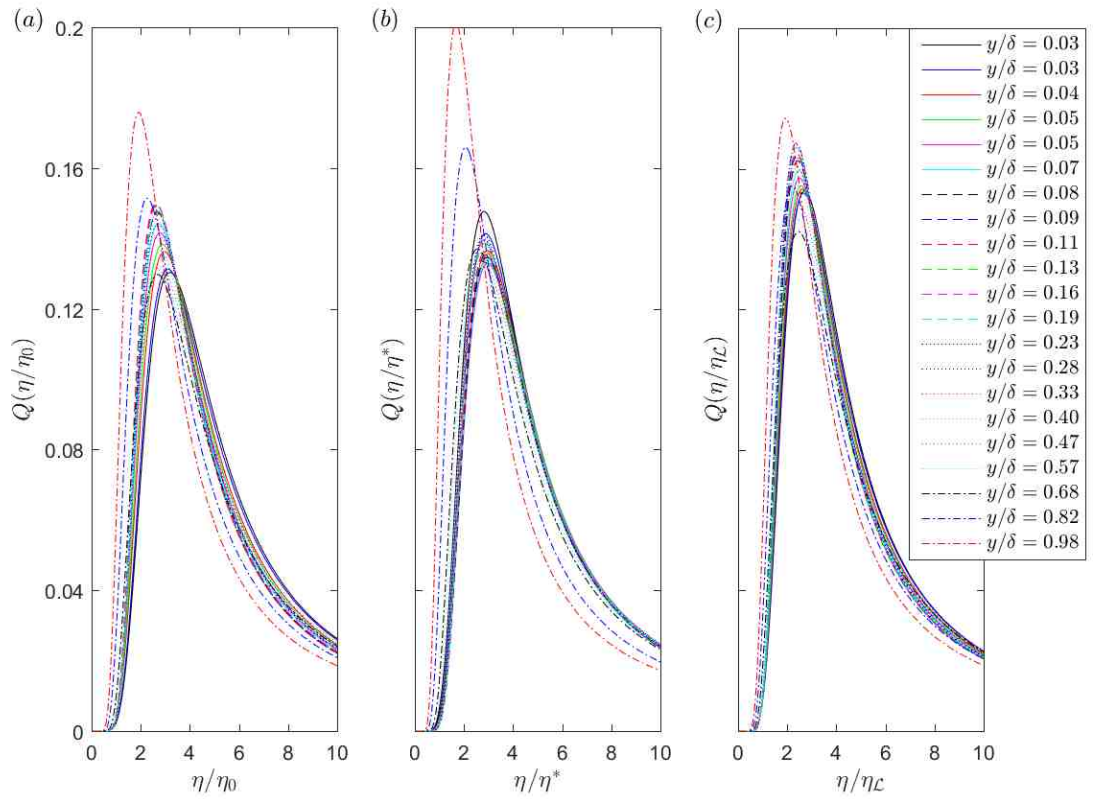Figure B2: Measured PDFs of local dissipation scales for the case with a turbulent free-stream condition using linear axes, normalized by: (a) η_0; (b) η^*; and (c) $\eta_\mathcal{L}$ from all measured positions within the boundary layer when the flow is intermittent.

Wall-Normal Dependence of Maximum PDFs:

The wall-normal dependence of all maximum values of PDFs are shown as isocontours normalized by η_0, η^* and $\eta_\mathcal{L}$ are presented below. This Figure shows the wall normal dependence of the maximum PDFs for the case with a laminar free-stream condition. Comparison between the different scaling parameter shows that η^* and $\eta_\mathcal{L}$ describe the PDFs better than η_0.

Figure B3: Isocontours of maximum values of the PDFs, showing wall normal dependence for the case with a laminar free-stream condition, normalized by: (a) η_0; (b) η^* ; and (c) $\eta_\mathcal{L}$. Symbols are as in Table (4.1) showing location of maximum probability.

Bibliography

[1] V. Yakhot, K. Sreenivasan, Towards a dynamical theory of multifractals in turbulence, Physica A: Statistical Mechanics and its Applications 343 (2004) 147–155.

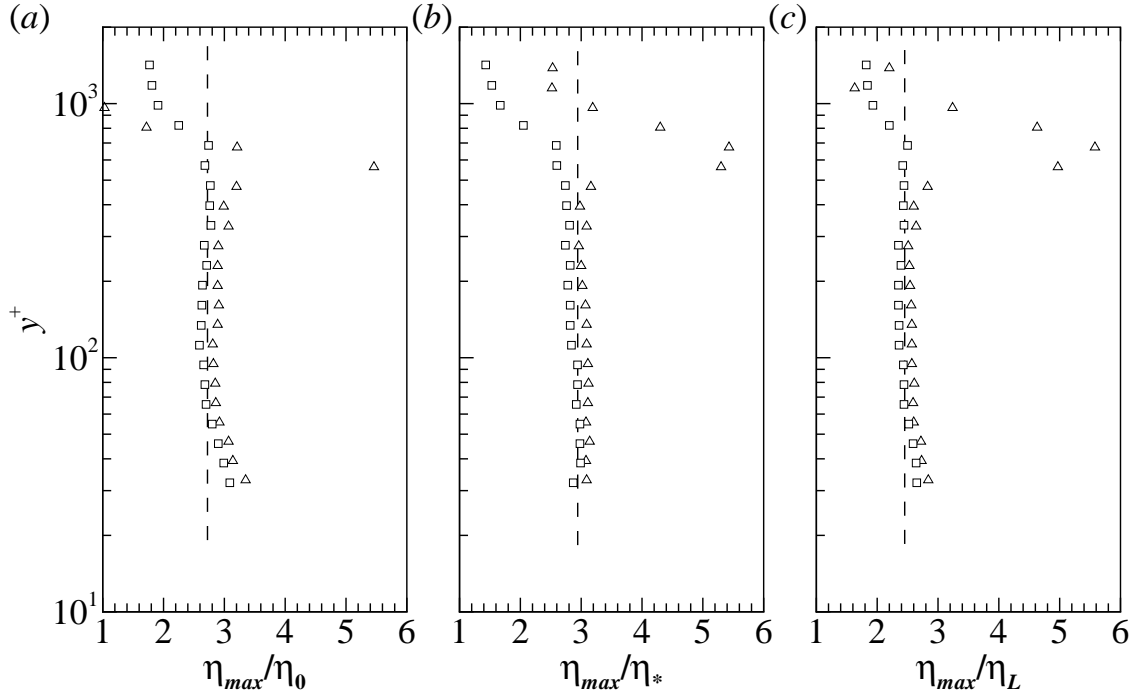[2] V. Yakhot, K. R. Sreenivasan, Anomalous scaling of structure functions and dynamic constraints on turbulence simulations, J. Stat. Phys. 121 (2005) 823–841.

[3] S. Wiggins, Introduction to applied nonlinear dynamical systems and chaos, Vol. 2, Springer Science & Business Media, 2003.

[4] R. E. Mayle, The 1991 igti scholar lecture: The role of laminar-turbulent transition in gas turbine engines, Journal of Turbomachinery 113 (4) (1991) 509–536.

[5] S. F. H. Alhamdi, A. K. H. Al-Taie, Flow separation of axial compressor cascade blades, Journal of Engineering 16 (2) (2010) 4877–4896.

[6] S. F. H. Alhamdi, Study of flow seperation between two axial compressor blades, Master's thesis, University of Technology, Baghdad, Iraq (2008).

[7] F. M. White, Viscous Fluid Flow, 2nd Edition, McGraw Hill, New York, NY, 1991.

[8] S. B. Pope, Turbulent Flows, Cambridge University Press, 2000.

[9] H. Tennekes, J. L. Lumley, A first course in turbulence, MIT press, 1972.

[10] J. Hinze, Turbulence 2nd ed., 790 (1975).

[11] A. Monin, A. Yaglom, Statistical fluid dynamics, Vol. I and II MIT Press, Cambridge.

[12] A. Monin, A. Yaglom, Statistical fluid mechanics: Mechanics of turbulence, vol. 2, 874 pp (1975).

[13] P. Davidson, Turbulence: an introduction for scientists and engineers, Oxford University Press, USA, 2015.

[14] P. Schlatter, R. Örlü, Q. Li, G. Brethouwer, J. H. Fransson, A. V. Johansson, P. H. Alfredsson, D. S. Henningson, Turbulent boundary layers up to $Re_\theta = 2500$ studied through simulation and experiment, Physics of fluids 21 (5) (2009) 051702.

[15] K. A. Chauhan, P. A. Monkewitz, H. M. Nagib, Criteria for assessing experiments in zero pressure gradient boundary layers, Fluid Dynamics Research 41 (2) (2009) 021404.

[16] D. Coles, The law of the wake in the turbulent boundary layer, Journal of Fluid Mechanics 1 (2) (1956) 191–226.

[17] R. Orlü, On the determination of the wall position in wall-bounded turbulent flows, Experimental studies in jet flows and zero pressure-gradient turbulent boundary layers (2009) 229.

[18] A. N. Kolmogorov, The local structure of turbulence in incompressible viscous fluid for very large Reynolds numbers, Dokl. Akad. Nauk SSSR 30 (1941) 301–305.

[19] H. L. Grant, R. W. Stewart, A. Moilliet, Turbulence spectra from a tidal channel, J. Fluid Mech. 12 (1962) 241–268.

[20] S. G. Saddoughi, S. V. Veeravalli, Local isotropy in turbulent boundary layers at high Reynolds number, J. Fluid Mech. 268 (1994) 333–372.

[21] F. Anselmet, Y. Gagne, E. Hopfinger, R. Antonia, High-order velocity structure functions in turbulent shear flow, J. Fluid Mech. 140 (1984) 63–89.

[22] U. Frisch, Turbulence: The Legacy of A. N. Kolmogorov, Cambridge University Press, 1995.

[23] A. Oboukhov, Some specific features of atmospheric tubulence, Journal of Fluid Mechanics 13 (1) (1962) 77–81.

[24] A. N. Kolmogorov, A refinement of previous hypotheses concerning the local structure of turbulence in a viscous incompressible fluid at high Reynolds number, Journal of Fluid Mechanics 13 (1) (1962) 82–85.

[25] K. Sreenivasan, P. Kailasnath, An update on the intermittency exponent in turbulence, Physics of Fluids A: Fluid Dynamics 5 (2) (1993) 512–514.

[26] G. Batchelor, A. A. Townsend, The nature of turbulent motion at large wavenumbers, Proc. R. Soc. Lond. A 199 (1949) 238–255.

[27] V. Yakhot, Probability densities in strong turbulence, Physica D: Nonlinear Phenomena 215 (2) (2006) 166–174.

[28] G. Paladin, A. Vulpiani, Degrees of freedom of turbulence, Phys. Rev. A. 35 (1987) 1971–1973.

[29] M. Nelkin, Multifractal scaling of velocity derivatives in turbulence, Phys. Rev. A 42 (12) (1990) 7226–7229. `doi:10.1103/PhysRevA.42.7226`.

[30] U. Frisch, M. Vergassola, A prediction of the multifractal model: the intermediate dissipation range, Europhys. Lett. 14 (1991) 439–444.

[31] L. Biferale, A note on the fluctuation of dissipative scale in turbulence, Phys. Fluids 20 (2008) 031703.

[32] J. Schumacher, Sub-Kolmogorov-scale fluctuations in fluid turbulence, Europhys. Lett. 80 (2007) 54001–1 – 54001–6.

[33] P. Hamlington, D. Krasnov, T. Boeck, J. Schumacher, Local dissipation scales and energy dissipation-rate moments in channel flow, J. Fluid Mech. 701 (2012) 419–429.

[34] S. C. C. Bailey, M. Hultmark, J. Schumacher, V. Yakhot, A. J. Smits, Measurements of the dissipation scales in turbulent pipe flow, Phys. Rev. Let. 103 (2009) 103.014502.

[35] Q. Zhou, K.-Q. Xia, Universality of local dissipation scales in buoyancy-driven turbulence, Physical Review Letters 104 (12) (2010) 124301.

[36] N. Morshed, S. Venayagamoorthy, L. Dasi, Intermittency and local dissipation scales under strong mean shear, Phys. Fluids 25 (2013) 011701.

[37] S. Bailey, B. Witte, On the universality of local dissipation scales in turbulent channel flow, J. Fluid Mech. 786 (2015) 234–252.

[38] S. Corrsin, A. L. Kistler, Free-stream boundaries of turbulent flows, NACA-TR-1244.

[39] Y. Tsuji, K. Honda, I. Nakamura, S. Sato, Is intermittent motion of outer flow in the turbulent boundary layer deterministic chaos?, Physics of Fluids A: Fluid Dynamics 3 (8) (1991) 1941–1946.

[40] K. Chauhan, J. Philip, C. M. de Silva, N. Hutchins, I. Marusic, The turbulent/non-turbulent interface and entrainment in a boundary layer, Journal of Fluid Mechanics 742 (2014) 119–151.

[41] A. Townsend, The fully developed wake of a circular cylinder, Australian Journal of Chemistry 2 (4) (1949) 451–468.

[42] G. Heskestad, Hot-wire measurements in a plane turbulent jet, Journal of Applied Mechanics 32 (4) (1965) 721–734.

[43] I. S. Gartshore, An experimental examination of the large-eddy equilibrium hypothesis, Journal of Fluid Mechanics 24 (1) (1966) 89–98.

[44] H. Fiedler, M. Head, Intermittency measurements in the turbulent boundary layer, Journal of Fluid Mechanics 25 (4) (1966) 719–735.

[45] R. E. Kaplan, J. Laufer, The intermittently turbulent region of the boundary layer, in: Applied Mechanics, Springer, 1969, pp. 236–245.

[46] I. Wygnanski, H. E. Fiedler, The two-dimensional mixing region, Journal of Fluid Mechanics 41 (2) (1970) 327–361.

[47] L. S. Kovasznay, V. Kibens, R. F. Blackwelder, Large-scale motion in the intermittent region of a turbulent boundary layer, Journal of Fluid Mechanics 41 (2) (1970) 283–325.

[48] R. Antonia, P. Bradshaw, Conditional sampling of turbulent shear flows, Imperial College of Science and Technology, Department of Aeronautics, 1971.

[49] M. Sunyach, Contribution a l'etude des frontieres d'ecoulements turbulents libres, Ph.D. thesis, Laboratoire de Mécanique des Fluides, École Centrale de Lyon (1971).

[50] R. Antonia, Conditionally sampled measurements near the outer edge of a turbulent boundary layer, Journal of Fluid Mechanics 56 (1) (1972) 1–18.

[51] R. Thomas, Conditional sampling and other measurements in a plane turbulent wake, Journal of Fluid Mechanics 57 (3) (1973) 549–582.

[52] S. F. H. Alhamdi, S. C. C. Bailey, External intermittency compensation of dissipation scale distributions in a turbulent boundary layer, Physical Review of Fluids (In Press).

[53] S. Tavoularis, Measurement in fluid mechanics, Cambridge University Press, 2005.

[54] S. Bailey, M. Hultmark, J. Monty, P. H. Alfredsson, M. Chong, R. Duncan, J. Fransson, N. Hutchins, I. Marusic, B. McKeon, et al., Obtaining accurate mean velocity measurements in high Reynolds number turbulent boundary layers using pitot tubes, Journal of Fluid Mechanics 715 (2013) 642–670.

[55] F. H. Clauser, The turbulent boundary layer, in: Advances in applied mechanics, Vol. 4, Elsevier, 1956, pp. 1–51.

[56] P. Schlatter, R. Örlü, Assessment of direct numerical simulation data of turbulent boundary layers, Journal of Fluid Mechanics 659 (2010) 116–126.

[57] K. Chauhan, H. Nagib, P. Monkewitz, On the composite logarithmic profile in zero pressure gradient turbulent boundary layers, in: 45th AIAA Aerospace Sciences Meeting and Exhibit, 2007, p. 532.

[58] Y. Chew, B. Khoo, G. Li, An investigation of wall effects on hot-wire measurements using a bent sublayer probe, Measurement Science and Technology 9 (1) (1998) 67.

[59] I. Marusic, G. J. Kunkel, Streamwise turbulence intensity formulation for flat-plate boundary layers, Physics of Fluids 15 (8) (2003) 2461–2464.

[60] G. I. Taylor, The spectrum of turbulence, Proc. R. Soc. Lond. 164 (919) (1938) 476–490.

[61] J. Lumley, Interpretation of time spectra measured in high-intensity shear flows, Phys. Fluids 8 (6) (1965) 1056–1062.

[62] F. H. Champagne, Fine-scale structure of turbulent velocity-field, J. Fluid Mech. 86 (1978) 67–108.

[63] R. Antonia, A. Chambers, N. Phan-Thien, Taylor's hypothesis and spectra of velocity and temperature derivatives in a turbulent shear flow, Boundary-Layer Meteorology 19 (1) (1980) 19–29.

[64] E. Siggia, Invariants for the one-point vorticity and strain rate correlation functions, Phys. Fluids 24 (11) (1981) 1934–1936.

[65] R. Prasad, C. Meneveau, K. Sreenivasan, Multifractal nature of the dissipation field of passive scalars in fully turbulent flows, Phys. Rev. Lett. 61 (1) (1988) 74.

[66] R. Prasad, K. Sreenivasan, Quantitative three-dimensional imaging and the structure of passive scalar fields in fully turbulent flows, J. Fluid Mech. 216 (1990) 1–34.

[67] A. A. Townsend, The Structure of Turbulent Shear Flow, Cambridge university press, 1980.

[68] K. R. Sreenivasan, R. A. Antonia, The phenomenology of smal-scale turbulence, Annu. Rev. Fluid Mech. 29 (1997) 435–472.

[69] M. Van Dyke, An Album of Fluid Motion, The Parabolic Press, Stanford, California, USA, 1982.

[70] A. A. Townsend, The Structure of Turbulent Shear Flow, Cambridge University Press, Cambridge, UK, 1976.

[71] K. C. Kim, R. J. Adrian, Very large-scale motion in the outer layer, Phys. Fluids 11 (2) (1999) 417–422.

[72] M. Guala, S. E. Hommema, R. J. Adrian, Large-scale and very-large-scale motions in turbulent pipe flow, J. Fluid Mech. 554 (2006) 521–542.

[73] B. J. Balakumar, R. J. Adrian, Large- and very-large-scale motions in channel and boundary-layer flows, Phil. Trans. R. Soc. A 365 (2007) 665–681.

[74] J. Nedić, S. Tavoularis, I. Marusic, Dissipation scaling in constant-pressure turbulent boundary layers, Physical Review Fluids 2 (3) (2017) 032601.

[75] L. Agostini, M. Leschziner, Spectral analysis of near-wall turbulence in channel flow at $Re_\tau = 4200$ with emphasis on the attached-eddy hypothesis, Physical Review Fluids 2 (1) (2017) 014603.

[76] S. F. H. Alhamdi, S. C. C. Bailey, Universality of local dissipation scales in turbulent boundary layer flows with and without free-stream turbulence, Physics of Fluids 29 (11) (2017) 115103.

[77] J. Jiménez, S. Hoyas, M. P. Simens, Y. Mizuno, Turbulent boundary layers and channels at moderate Reynolds numbers, Journal of Fluid Mechanics 657 (2010) 335.

[78] T. B. Hedley, J. F. Keffer, Some turbulent/non-turbulent properties of the outer intermittent region of a boundary layer, Journal of Fluid Mechanics 64 (4) (1974) 645–678.

[79] C.-H. P. Chen, R. F. Blackwelder, Large-scale motion in a turbulent boundary layer: a study using temperature contamination, Journal of Fluid Mechanics 89 (1) (1978) 1–31.

[80] J. H. Lee, H. J. Sung, Very-large-scale motions in a turbulent boundary layer, Journal of Fluid Mechanics 673 (2011) 80–120.

[81] S. C. C. Bailey, B. M. Witte, On the universality of local dissipation scales in turbulent channel flow, Journal of Fluid Mechanics 786 (2016) 234–252.

[82] J. Schumacher, J. Scheel, D. Krasnov, D. Donzis, V. Yakhot, K. R. Sreenivasan, Small-scale universality in fluid turbulence, PNAS 111 (2014) 10961–10965.

Vita

Sabah F. H. Alhamdi

Researchgate.net/profile/Sabah Alhamdi

Linkedin.com/in/sabah-alhamdi-21861276

ACADEMIC QUALIFICATIONS

M.Sc. in Mechanical Engineering   Apr 2008

 University of Technology, Baghdad, Iraq

GPA 82.305/100, Advisor: Arkan Kh. Al-Taie

Thesis Topic: Study of Flow Separation between Two Axial Compressor Blades.

B.Sc. in Mechanical Engineering   Aug 2004

University of Technology, Baghdad, Iraq

GPA 78.139/100

RESEARCH EXPERIENCE

Ph.D Program Research   Aug 2012–May 2018

University of Kentucky, Lexington, KY, USA

Graduate Research   Sep 2004–Apr 2008

University of Technology, Baghdad, Iraq

Undergraduate Research   Aug 2003–Aug 2004

University of Technology, Baghdad, Iraq

TEACHING EXPERIENCE

Teaching Assistant   Aug 2015–May 2018

University of Kentucky, Lexington, KY, USA

Faculty   Jan 2009–Aug 2011

University of Misan, Misan, Iraq

FIELD EXPERIENCE

Engineer and Head of Mechanical Department   Dec 2005–Jan 2009

Directorate of Misan Sewage, Misan, Iraq

Engineer at the Scientific and Engineering Consulting Bureau   Sep 2004–Apr 2008

University of Technology, Baghdad, Iraq

RECOGNITIONS, HONORS AND AWARD

• Two Certificates of Appreciation from the Dean of the College of Education at the University of Misan for tremendous efforts as a member of the examination committees for the academic years 2008-2009 and 2009-2010

• Certificate of Appreciation from the Dean of the College of Education at the University of Misan for great efforts as a member of the Organizing Committee of the First Scientific Conference at the university in 2011

• Certificate of Appreciation from the President of the University of Technology in Baghdad for ranking first among the department master graduates in 2008

• Receipt of Competitive Scholarship from the Office of the Prime Minister of Iraq through the Higher Committee for Education Development (HCED) in Iraq

• Professional Membership: American Institute of Aeronautics and Astronautics (AIAA)

• Membership: Omicron Delta Kappa National Leadership and Honor Society (OΔK)

JOURNALS PUBLICATIONS, AND CONFERENCE AND POSTER PRESENTATIONS

• Sabah F. H. Alhamdi and Sean C. C. Bailey (In Press), "External intermittency compensation of dissipation scale distributions in a turbulent boundary layer", Physical Review of Fluids.

• Sabah F. H. Alhamdi and Sean C. C. Bailey (November 2017), "Universality of local dissipation scales in turbulent boundary layer flows with and without free-stream

turbulence", Physics of Fluids, vol. 29, no. 11.

• Sabah F. H. Alhamdi and Sean C. C. Bailey (March 2017), "Local dissipation scales in external wall-bounded flows with and without free-stream turbulence", AIAA, The 42snd Dayton-Cincinnati Aerospace Sciences Symposium, Dayton, OH.

• Sabah F. H. Alhamdi and Sean C. C. Bailey (March 2016), "The effect of a locally oscillating wall on a turbulent boundary layer", AIAA, The 41st Dayton-Cincinnati Aerospace Sciences Symposium, Dayton, OH.

• Sabah F. H. Alhamdi and Sean C. C. Bailey (April 2016), "The effect of a locally oscillating wall on a turbulent boundary layer", the 1st ME Graduate Student Poster Competition, Department of MechanicalEngineering, University of Kentucky, College of Engineering, Lexington, KY.

• Muther S. Hameed, Buraq T. Shealash, and Sabah Faleh Habeeb (2011), "Computing pressure effect on projectile at an altitude 4Km above the sea level", College of Education Journal, University of Misan, Misan, Iraq, No. 22 V 96.

• Sabah F. H. Alhamdi and Arkan K. H. Al-Taie (June 2010), "Flow separation of axial compressor cascade blades", The Journal of Engineering, University of Baghdad, Baghdad Iraq, No. 3 V 16.

REFEREEING MANUSCRIPTS FOR SCHOLARLY JOURNALS

 • Physics of Fluids

- A peer-reviewed monthly scientific journal on fluid dynamics, founded by the American Institute of Physics in 1958, and is published by the AIP Publishing

- Reviewed five manuscripts in my field of research